Phase Stability of Precipitates After Ion Irradiation and Creep Deformation in Cu Alloys

A Dissertation Presented for the

Doctor of Philosophy

Degree

The University of Tennessee, Knoxville

Ling Wang

May 2020

Copyright © 2020 by Ling Wang
All Rights Reserved

ACKNOWLEDGMENTS

I would like to thank my advisor, Prof. Steven J. Zinkle, for his advice, support and guidance. During my graduate study, I benefited from his vision in science, and the opportunity and freedom he has given me to explore and pursue my scientific interests.

This research involves the characterization on two groups of materials. Efforts from many people have been made in order to make it possible and successful. Firstly, I would like to thank my research team in Theme I, Dr. Arunodaya Bhattacharya and Dr. Chad Parish both from Oak Ridge National Laboratory (ORNL). Their rich experience in TEM characterization has been very beneficial for this research. The research team from Argonne National Laboratory cannot be overlooked. Dr. Meimei Li supervised my research when I was a summer intern in the IVEM group during 2019. She has provided insightful advice since my first experiment in IVEM, and encouraged me to submit RTE proposals for later on in situ ion irradiation experiments. In addition, Dr. Li has extensive knowledge in mechanical properties of materials, and she worked with me to quantify the minimum strain rate on newly developed Cu alloys creep behavior. Dr. Wei-Ying Chen oversaw specimen preparations and TEM characterizations. His skillful technique promoted my understanding in radiation defects characterization; patience and carefulness are so important during the TEM characterization. Dr. Peter M. Baldo has more than 20 years of experience in ion irradiation accelerators, and his responsible manipulation guaranteed the precise damage dose and flux and his widespread experience in different materials response to irradiations leaves a positive impression. I feel so lucky to have been working with these excellent researchers for the 2019 summer. Mr. David Martin and Prof. Brian D Wirth from Nuclear Engineering Department, UTK, have been working on the MD simulations for expanding my understanding in interstitial defects interaction with coherent precipitates for more than one year. Their continuous efforts and dynamic results make it possible to combine both experimental and MD simulation results in this theme and present a thorough story on the coherency loss of the precipitates after irradiation.

I would also like to thank my research team in Theme II. Dr. Ying Yang (ORNL) is the principal investigator in this theme and developed new Cu alloys for this study. Dr. Lizhen Tan (ORNL) helped with mechanical tests design and analysis. Dr. Ce Zheng, from North Carolina State University, has helped with STEM-EDS mappings on the precipitates. Dr. Boopathy

Kombaiah from ORNL and now a research staff in Idaho National Laboratory helped with additional EDS mappings when he was in ORNL, and also provided critical comments on creep test results based on his experience. Prof. Lance L. Snead and Prof. David J. Sprouster from Stonybrook University helped with small angle x-ray diffraction characterization for investigating the precipitate size, volume fraction and lattice parameter.

This work won't be possible without many other scientists and staffs, Prof. Miguel L. Crespillo, Dr. Haizhou Xue, Dr. Yufan Zhou, Ms. Cheng Xu, Ms. Lauren Nuckols for their excellent work in IBML. Dr. Yutai Katoh from ORNL, for his timely and coordinated management to keep the project moving forward. Prof. John Dunlap, Prof. Gerd Duscher and Ms. Chenze Liu from UTK Microscopy Center for their timely help and rich experience.

Thanks also give to all members from Prof. Zinkle's group, students from MSE Class of 2015 for their academic knowledge and friendship.

I would like to thank my committee members, Prof. Yanwen Zhang, Prof. William J. Weber, and Prof. Maik K. Lang for their time, support and reviewing my thesis.

Finally, I deeply appreciate my family's support and encouragement during my graduate career. Thank you to my mom and my dad for their love and endless support during this period.

ABSTRACT

In this work two main research themes are studied in order to improve our understanding of how structural materials perform in extreme operating environment such as fission and fusion energy systems by utilizing advanced microstructural characterization to investigate the structure, precipitate-matrix orientation, and general stability of precipitates in model Cu-base structural alloys.

Theme I focuses on fundamental understanding of phase stability of nanoscale precipitates within and beyond the ion displacement damage region in irradiated dilute Cu-base model alloys (Cu-1%Co, Cu-1%Fe and Cu-0.8%Cr). First, the in situ irradiation experiments with 1 MeV Kr^{++} ions provide some indication of the critical dose to induce loss of precipitate coherency. The observed effect of suppressed loss of coherency at high sink strengths might be due to nearly equal numbers of interstitial and vacancy defects arriving at the precipitate interface. At low sink strengths, there might be a preferential medium-range strain-induced bias for absorption of interstitial defects at the precipitates that accelerates coherency loss. Second, we use these coherent precipitates with different sink strengths as a 'diagnostic monitor' to provide an indicator of the radiation defect migration behavior via ex situ 1 MeV Ni^{+} irradiation. Evidence for pronounced defect migration well beyond the maximum range of the ion irradiation region suggests significant 1D migration of defect clusters.

Theme II aims to analyze and understand the mechanical deformation mechanisms, especially regarding creep resistance, of newly designed CuCrNbZr alloys compared to commercial CuCrZr alloys for fusion energy applications. This new developed Cu alloy has been confirmed to have a multi-modal distribution of precipitates with fine Cr precipitates and Cu_5Zr intermetallic compounds in the matrix and coarse Laves_Cr_2Nb phase at the grain boundaries. The matrix precipitates contribute to high tensile strength and resistance to dislocation power law creep whereas the grain boundary precipitates suppress grain boundary crack propagation and increase creep strength and life at test temperatures of 500 ^{o}C.

TABLE OF CONTENTS

CHAPTER 1 INTRODUCTION 1

1.1 Precipitate stability under irradiation 1
1.1.1 Precipitate shrinkage and coarsening 1
1.1.2 Coherency loss of precipitates after irradiation 7
1.1.3 MD Simulations and experiments on defects migration behavior in fcc and bcc matrix 10
1.1.4 Motivation and objectives 15
1.2 Development of high strength high conductivity materials 15
1.2.1 Cu-Cr binary alloys 16
1.2.2 Commercial CuCrZr and ODS GlidCop Al25 alloys 17
1.2.3 NASA CuCrNb alloys 19
1.2.4 Grain boundary embrittlement and sliding limit high temperature applicability 20
1.2.5 Motivation and objectives 21

CHAPTER 2 METHODS AND TECHNIQUES 25

2.1 Sample description 25
2.1.1 Dilute Cu alloys 25
2.1.2 CuCrNbZr alloys 28
2.2 Ion irradiation 31
2.2.1 In situ ion irradiation 31
2.2.2 Ex situ ion irradiation 36
2.3 TEM 38
2.3.1 TEM specimen preparation 38
2.3.2 Basics of TEM and imaging conditions 39
2.3.3 Quantitative measurements of precipitates and defect clusters 40
2.3.4 In situ TEM 45
2.3.5 Chemical composition analysis 46
2.4 Electrical resistivity measurement 47
2.5 Mechanical tests 48

2.6 Other Microstructure characterization 49
2.6.1 SEM 49
2.6.2 XRD 49

CHAPTER 3 EXPERIMENTAL RESULTS 51

3.1 As fabricated characterization 51
3.2 In situ observation during thin foil ion irradiation 54
3.2.1 In situ observation of precipitate coherency loss during RT irradiation 54
3.2.2 In situ observation of precipitate evolution during high temperature irradiation 59
3.2.3 In situ observation of precipitates evolution during cryogenic temperature irradiation 66
3.2.4 In situ irradiation summary of coherent precipitate stability 66
3.3 Post-irradiation cross-section characterization after bulk ion irradiation 70
3.3.1 Damage region 70
3.3.2 Post-irradiation microstructure after room temperature irradiation 71
3.3.3 Post-irradiation microstructure after high temperature irradiation 74
3.3.4 Post-irradiation microstructure after cryo-temperature irradiation 74
3.3.5 Post-irradiation summary of precipitate stability within and beyond damage region .. 82
3.4 Precipitate characterization in as-fabricated and creep-tested CuCrNbZr alloys 84
3.4.1 Electrical resistivity and Vickers hardness 88
3.4.2 XRD results 89
3.4.3 Optical microscopy and SEM results 89
3.4.4 Nano-scale precipitates 90
3.4.5 Tensile test results 92
3.4.6 Creep test results 92
3.4.7 Summary of CuCrNbZr precipitate characterization 103

CHAPTER 4 DISCUSSION 104

4.1 Dilute Cu alloys 104
4.1.1 Sink strength effect on coherency loss of precipitates in irradiated regions 104
4.1.2 Comparison of observed 1D migration of SIAs clusters with MD simulations 106
4.1.3 The effect of Cu SIA clusters on the coherency of a Co precipitate 108
4.1.4 Quantification of vacancy defects during ion irradiations 113
4.2 CuCrNbZr alloys 115

4.2.1 Threshold stress analysis and creep mechanism in CuCrZr and CuCrNbZr_HP alloys 115
4.2.2 Roles of Laves phase on the creep property of the CuCrNbZr_HP alloy 118
4.2.3 Precipitate stability after creep 120

CHAPTER 5 CONCLUSION 126

5.1 Dilute Cu alloys 126
5.2 CuCrNbZr alloys 127

REFERENCES 129

VITA 137

LIST OF TABLES

Table 2-1: Chemical composition of four dilute Cu alloys (wt.%). 26
Table 2-2: Pre-ion irradiation heat treatment. 27
Table 2-3: Chemical composition and room temperature properties of CuCrZr compared with designed CuCrNbZr alloy. 33
Table 2-4: Summary of irradiation conditions of CC1, CC2, CC3, CC4, CFZ and CCZ alloys with concerns of irradiation temperature, damage dose and post-irradiation annealing. 35
Table 2-5: Summary of ex situ ion irradiation conditions of CC1, CC2, CFZ-0 alloys with concerns of irradiation temperature, damage dose, fluence and flux. 37
Table 2-6: Parameters for calculating the thickness using thickness contour method [58]. 44
Table 3-1: Summary of initial precipitate mean size, density and sink strength corresponding to different thermal aging conditions in Cu-1%Co, Cu-1%Fe (minor Zr) and Cu-0.8%Cr (minor Zr) alloys. 54
Table 3-2: Summary of room temperature properties of the 1st heat of CuCrNbZr alloys [48]. . 85
Table 3-3: Room temperature electrical resistivity and conductivity calculations for CuCrZr and CuCrNbZr_HP alloys. 89
Table 3-4: 0.2% Yield strength on CuCrZr, and CuCrNbZr_HP alloys at 24, 300 and 500 ^{o}C. . 97
Table 3-5: Minimum creep strain rates for CuCrZr and CuCrNbZr_HP alloys at 500 °C and 90, 100, 110, 125 and 140 MPa. 101
Table 4-1: Calculation results by 1D vs. 3D migration of SIA clusters on microstructural evolution and comparison to observed precipitate loss of coherency BEOR. 107
Table 4-2: MD simulation systems setup. 109
Table 4-3: Threshold stress analysis for CuCrZr and CuCrNbZr_HP alloys. 102
Table 4-4: Calculated miminum grain boundary strain rate for CuCrZr and CuCrNbZr_HP alloys at 500 ^{o}C and applied stresses of 90, 100, 110, 125 and 140 MPa. 117

LIST OF FIGURES

Figure 1-1: Computer simulation. (a) and (b) are for high and medium irradiation temperatures, while (c) is for low irradiation temperatures [6]. 2
Figure 1-2: Cluster size versus irradiation dose with 1.8 MeV Kr ions at elevated temperatures in dilute (a) Cu-Ag, (b) Cu-Co and (c) Cu-Mo binary alloys [7]. 2
Figure 1-3: Plot of nanoparticle diameter cubed versus the displacement damage dose after ion irradiation at 500 °C and neutron irradiation at 430 °C [8]. 3
Figure 1-4: Evolution of the nanoparticle distribution during irradiation [9]..... 4
Figure 1-5: Comparison of dispersoid diameter distribution of ferrite and tempered martensite grains [10]. 5
Figure 1-6: Schematic stability/evolution of the TaC, TaN and VN nanoprecipitates under ion irradiation from low to high doses. The tiny spots denote ejected atoms [11]. 5
Figure 1-7: Thermal aging induced coherency loss of Al_3Sc [14]. 8
Figure 1-8: Coherency loss before and after (a) electron irradiation [15]; (b) fast neutron irradiation [16] and (c) heavy ion irradiation [18]. 8
Figure 1-9: Schematic image of 'vacancy' type coherent precipitate and incoherent precipitate with the matrix [17]. 11
Figure 1-10: Energies of coherency loss versus radius of dislocation loop [16]. 11
Figure 1-11: Schematic illustration of the nature of 1D migration interrupted both by direction change (1D/3D-DC) and by transverse climb excursions (1D/3D-TC) [22]. 14
Figure 1-12: Room temperature strength and conductivity of selected high-performance Cu alloys [26]. 22
Figure 1-13: TEM images of the Cu alloy aged for 10 h at 440 ^{o}C [31]. 23
Figure 1-14: Yield strength (corrected for temperature-dependent elastic modulus, *E'=E(T)/E(20 ^{o}C))* versus reciprocal temperature for several copper alloys [26]. 24
Figure 2-1: TEM bright-field images with inset diffraction patterns and individual elemental mappings of Cu, Co and Fe in (a) CC1; (b) CC2 and (c) CFZ-0 alloy. 27
Figure 2-2: Solidification path simulation of the designed CuCrNbZr alloys [48]. 29

Figure 2-3: Calculated mole fraction of phases in the designed alloy as a function of temperature. The optical microscopy image shows coarse precipitates (Cr_2(Nb,Zr) Laves phase) at grain boundary and TEM image shows fine precipitates (Cr precipitates) in the matrix [48]..... 29
Figure 2-4: Typical optical images of newly fabricated CuCrNbZr alloys in low and high magnifications..... 33
Figure 2-5: IVEM-Tandem facility at Argonne National Laboratory. The accelerator is coupled to a Hitachi-9000 NAR TEM operated at 300 keV, impinging at a glancing 30^o into the electron-transparent specimen areas [52]..... 34
Figure 2-6: SRIM prediction profile of depth distribution of displacement damage and implanted ions for 1 MeV Kr^{++} ions irradiated to 1.0×10^{14} ions/cm^2..... 34
Figure 2-7: Depth profiles of displacement per damage (dpa) and induced Ni ion concentration predicted by SRIM code for dilute Cu alloys irradiated with 1 MeV Ni^+ ions to fluences of 7×10^{15} ions/cm^2..... 37
Figure 2-8: (a) Ion irradiation accelerator; (b) ion irradiation sample stage; (c) beam area judgement..... 38
Figure 2-9: Zeiss Crossbeam Augria FIB/SEM instrument at JIAM (left); and Fischione Nanomill 1040 system at LAMDA (right)..... 39
Figure 2-10: Coherent Fe-precipitates in a Cu-1%Fe alloy thermal aged at 600 ^{o}C for 15 h..... 41
Figure 2-11: JEOL 2100F S/TEM instrument at LAMDA..... 42
Figure 2-12: TEM images of CC2 alloy before RT irradiation. The imaging condition is g=220 dynamical for BF and DF. 44
Figure 2-13: Unfiltered thickness map (left); relative thickness map (right) of a FIB-prepared TEM thin foil from an un irradiated CC1 alloy. 45
Figure 2-14: Kinematic TEM images of RT irradiated CC1 alloy post-irradiation annealed at 500 ^{o}C for 40 min..... 46
Figure 2-15: FEI Talos F200X S/TEM, along with a SuperX four-detector EDS system at LAMDA..... 47
Figure 2-16: Four-wire electrical resistivity measurement for SS-3 tensile bar (left); linear fitting for resistance (right)..... 48
Figure 3-1: Typical microstructures of thermal-aging-produced coherent Co precipitates (CC1, CC2, CC3, CC4 alloys), Fe precipitates (CFZ alloy) and Cr precipitates (CCZ alloy). TEM images

were taken in dynamical two-beam conditions as indicated in the inset electron diffraction patterns. 53
Figure 3-2: (a) CC3 thin foil irradiated with 1 MeV Kr^{++} ions at RT to 0.00125, 0.00625, 0.125 dpa; (b) irradiated CC3 thin foil post-irradiation annealed from RT to 300 ^{o}C and stayed for 10 min then annealed to 400 ^{o}C for 10 min, 500 ^{o}C for 40 min. The imaging condition is **g**=220 dynamical BF. 56
Figure 3-3: CFZ thin foil irradiated with 1 MeV Kr^{++} ions at RT to 0.0025, 0.0125 and 0.625 dpa, then annealed to 300 ^{o}C and held for 10 min then annealed at 400 ^{o}C for 10 min, and 500 ^{o}C for 40 min. Imaging condition is g=200 (g, 3g) kinematic for BF and WBDF..... 57
Figure 3-4: Microstructures of initial coherent precipitates after RT irradiation to 1.25 dpa, 0.25 dpa, 0.0125 dpa, 0.25 dpa and 0.25 dpa and post-irradiation annealing at 500 ^{o}C (400 ^{o}C for CCZ alloy) in CC1, CC2, CC3, CC4, CFZ and CCZ alloys. Images were taken in strong two-beam conditions. 59
Figure 3-5: Diffraction patterns of CC1 alloy annealed to 200 ^{o}C before irradiation. The imaging conditions are **g**=200 for dynamic BF and CDF, **g**=200 (g, 3g) for kinematic BF and WBDF. .. 60
Figure 3-6: Low magnification TEM images of un-irradiated CC1 alloy at 200 ^{o}C. The imaging condition is g=002 for bright field and (g, 3g) for weak beam dark field with beam direction close to [110]. 61
Figure 3-7: High magnification TEM images from the center area of Figure 3-6. The imaging condition is g=002 for bright field and (g, 3g) for weak beam dark field with beam direction close to [110]. 62
Figure 3-8: TEM images of CC1 alloy irradiated at 200 ^{o}C to 0.0025, 0.0125, 0.0625 and 0.125 dpa. The imaging condition is g=002 for bright field and (g, 3g) for weak beam dark field with beam direction close to [110]..... 63
Figure 3-9: High magnification TEM images of CC1 alloy irradiated at 200 ^{o}C to 0.0025 and 0.125 dpa. The imaging condition is g=002 (g, 3g) for weak beam dark field with beam direction close to [110]..... 65
Figure 3-10: TEM images of CC3 alloy irradiated at -223 ^{o}C with 1 MeV Kr^{++} ions, the dose rate was controlled at 10^{-4} dpa/s, the first 9 s recorded the precipitate strain field change. The imaging condition is g=022 for bright field with beam direction close to [100]. 67

Figure 3-11: TEM images of CC3 alloy initially irradiated at -223 ºC to 0.0625 dpa with 1 MeV Kr^{++} ions then sequentially post-irradiation annealed to RT, 300 and 400 ºC. The imaging condition is g=022 for bright field with beam direction close to [100]. 68
Figure 3-12: TEM images of CC3 alloy initially irradiated at -223 ºC to 0.0625 dpa with 1 MeV Kr^{++} ions then post-irradiation annealed to 500 ºC. The imaging condition is g=022 for bright field and center dark field with beam direction close to [100]..... 68
Figure 3-13: Summary of irradiation conditions in all the in situ irradiation experiments in CC1, CC2, CC3, CC4, CFZ and CCZ alloys. 69
Figure 3-14: TEM-EDS mappings of CC2, CC1 and CFZ alloys irradiated with 1 MeV Ni^{+} ions to a mid-range dose of 10 dpa at 25 and 350 ºC. 71
Figure 3-15: Cross-section TEM microstructure of CC2 alloy irradiated with 1 MeV Ni^{+} ions at RT to a mid-range dose of 1 dpa. 72
Figure 3-16: Cross-section TEM microstructure of CC2 alloy irradiated with 1 MeV Ni^{+} ions at RT to a mid-range dose of 10 dpa. 73
Figure 3-17: Cross-section STEM-BF images of CC1 alloy irradiated with 1 MeV Ni^{+} ions at 350 ºC to a mid-range dose of 10 dpa. The cross-section depth at the center of the image is indicated below the photos. All images are at the same magnification. 76
Figure 3-18: Cross-section STEM-BF images of CC2 alloy irradiated with 1 MeV Ni^{+} ions at 350 ºC to a mid-range dose of 10 dpa. 68
Figure 3-19: Cross-section STEM-BF images of CC2 alloy irradiated with 1 MeV Ni^{+} ions at 350 ºC to a mid-range dose of 10 dpa. 68
Figure 3-20: Cross-section TEM microstructure of CFZ-0 alloy irradiated with 1 MeV Ni^{+} ions at 350 ºC to a mid-range dose of 0.1 dpa. 69
Figure 3-21: Cross-section TEM microstructure of CFZ-0 alloy irradiated with 1 MeV Ni^{+} ions at 350 ºC to a mid-range dose of 10 dpa. 80
Figure 3-22: Cross-section TEM microstructure of CC2 alloy irradiated with 1 MeV Ni^{+} ions at -117 ºC to a mid-range dose of 1 dpa. 81
Figure 3-23: Observed BEOR loss of coherency versus dose. 83
Figure 3-24: (a) TEM-BF image of a thermal aged CuCrNbZr alloy pre-cold rolled to 70% showing a large Cr precipitate in the matrix surrounded by a cluster of Cr_2Nb C15 Laves phase precipitates; (b) <111> SADP of Cr precipitate in (a); (c) CDF image of one of Laves phase

precipitates selected with white rectangle in (a); (d) HRTEM image from the white rectangle in (a); (e) <110> SADP according to (d); (f) the individual composition maps of Cu, Cr, Nb, Zr, and Fe indicating that Zr is uniformly distributed both in the matrix and Laves phases. 85
Figure 3-25: HAADF image and elemental TEM-EDS mappings of Cu, Fe, O, Zr, Cr, Nb and Sn focused on the Laves precipitate/matrix interface. 86
Figure 3-26: STEM-BF image showing a Cr precipitate located at the grain boundary and matrix coherent Cr precipitates uniformly distributed. This grain boundary precipitate will be characterized in detail later. 86
Figure 3-27: (a) TEM-BF image of the CuCrNbZr_70 alloy showing a coarse Cr precipitate located at the grain boundary; (b) <110> SADP of the right grain in (a) marked with white dotted lines; (c) <111> SADP of the grain boundary Cr precipitate in (a); (d) STEM-BF image on a larger area and the individual composition maps Cu, Cr, Nb, Zr and Fe [48]. 87
Figure 3-28: X-ray diffraction pattern of the CuCrNbZr_HP alloy in as-aged condition. (D. Sprouster, Stonybrook University) 93
Figure 3-29: (a) and (c) are the optical microstructures of the grain morphologies of CuCrZr and CuCrNbZr_HP alloys in as-aged conditions, respectively; (b) and (d) are SEM images with the inset line scan results showing the chemical compositions of those micro-scale precipitates within and along the grain boundaries. 93
Figure 3-30: (a) HAADF image and elemental TEM-EDS mappings of Cu, Cr, Nb, Zr and O showing the laves phase Cr_2Nb precipitated in the matrix; (b) [110] SADP of the Laves_Cr_2Nb taken from dotted blue rectangle showing the C15-type cubic structure, and (c) the corresponding HRTEM image of Laves_Cr_2Nb. 94
Figure 3-31: (a) STEM-BF image near the [110] Cu matrix zone axis with g=002, showing Cu_5Zr precipitates along two $\{111\}_{Matrix}$ planes [66]; (b) [112] matrix zone axis selected area diffraction pattern showing the precipitation orientation relationship of Cu_5Zr (red circles) with the Cu matrix. The superlattice reflections marked by purple arrows show the bcc Cr precipitates follow the N-W OR with the fcc Cu matrix; (c) and (d) high resolution TEM image of a Cu_5Zr precipitate along the <011> zone axis with the corresponding FFT pattern, indicating the precipitation habit plane is along $(\bar{1}\bar{1}1)$ of the Cu matrix. 95
Figure 3-32: STEM-BF images and Cr EDS mapping of coherent Cr-rich precipitates in the (a, b) CuCrZr alloy and (c, d) CuCrNbZr_HP alloys in as-aged condition. The images in (a, c) were

taken under dynamical diffraction conditions along the [011] zone axis using g=200 (diffraction vector direction shown by the white arrows). 96
Figure 3-33: (a) Ultimate tensile strength versus temperature curves and (b) uniform elongation versus temperature curves for newly developed CuCrNbZr_HP alloys compared with existing commercial Cu alloy [68]. 97
Figure 3-34: Plots of creep strain versus test time of CuCrZr and CuCrNbZr_HP alloys at 500 ^{o}C and 90 MPa. The test environment was in air. 99
Figure 3-35: Plots of creep strain versus test time at 500 ^{o}C for (a) CuCrZr and (b) CuCrNbZr_HP alloy under applied stresses of 90, 100, 110, 125 and 140 MPa. 100
Figure 3-36: Applied stress versus rupture time. 101
Figure 3-37: (a) Minimum creep rate versus applied stress for CuCrZr and CuCrNbZr_HP alloys on a double logarithmic scale; (b) minimum strain rate inversely proportional to rupture time on a double logarithmic scale. 102
Figure 4-1: TEM-BF images of CC1 alloy irradiated to 1 dpa at RT then post-irradiation annealed at 500 ^{o}C (left) and CC2 alloy irradiated to 0.25 dpa at 340 ^{o}C (right) with 1 MeV Kr^{++} ions. . 105
Figure 4-2: TEM-BF images of (a) CC1 and (b) CC2 alloys irradiated at 340 ^{o}C with 1 MeV Kr^{++} ions. 107
Figure 4-3: MD simulations results at 727 ^{o}C, 2 ns. 109
Figure 4-4: Cluster size distribution at 5 ns for (a) 227 ^{o}C and (b) 727 ^{o}C. 110
Figure 4-5: Cumulative fraction of interstitial versus distance from center of precipitate at (a) 227 ^{o}C and (b) 727 ^{o}C. 110
Figure 4-6: A 15 nm-diameter Co precipitate with the sink strength of 6.8×10^{14} m^{-2} at 727 ^{o}C at 0 ns (left) and 5 ns (right). 112
Figure 4-7: Perspective view of 2 separate 5 nm-diameter precipitates at 727 ^{o}C with a sink strength of 6.7×10^{14} m^{-2}. 112
Figure 4-8: Perspective side view of a 15 nm-dimeter Co precipitate/Cu matrix interface simulated at 727 ^{o}C with 24 interstitial clusters at 0 ps (left) and 15 ps (right). Co precipitate in blue and Cu matrix in grey. 113
Figure 4-9: Defect cluster density of CC1 alloys irradiated at 200 and 340 ^{o}C with 1 MeV Kr^{++} ions up to 0.125 dpa. 114

Figure 4-10: Defect cluster density of CFZ alloy initially irradiated at RT with 1 MeV Kr^{++} ions up to 0.625 dpa then post-irradiation annealed to temperatures of 300, 400 and 500 ^{o}C. 114
Figure 4-11: (a) Threshold stress calculation using linear extrapolation method for n=2, and (b) minimum strain rate versus effective stress at 500 ^{o}C. 117
Figure 4-12: Normalized minimum creep strain rate as a function of effective stress of CuCrZr (blue) and CuCrNbZr_HP (red) alloys. 121
Figure 4-13: (a) and (b) SEM images of the entire fracture of the CuCrZr and CuCrNbZr_HP alloys at 500 °C and 90 MPa, respectivley, (c) and (d) magnified images of dotted blue rectangle regions in (a) and (b) showing larger cracks (indicated by yellow arrows) at grain boundaries without Laves phases, and small cracks at grain boundaries covered by Laves phase (indicated by red arrows). 122
Figure 4-14: STEM-BF image showing a micron-scale Laves phase pinning the multi grains, leaving the dislocations pile up at the interface between the Laves phase and matrix in a crept CuCrNbZr_HP alloy. 123
Figure 4-15: Optical images showing grain size of the (a) CuCrZr and (b) CuCrNbZr_HP alloys after creep tests (images taken from unstressed tab area). 123
Figure 4-16: STEM-HAADF image and individual composition maps of Cu, Cr and Zr in CuCrZr alloy after creep at 500 ^{o}C and 90 MPa in air (images taken from stressed gauge area). 124
Figure 4-17: STEM-HAADF image and individual composition mappings of Cu, Cr and Zr and a two-elemental-composition map of Cr and Zr in CuCrNbZr_HP alloy after creep at 500 ^{o}C and 90 MPa in air (images taken from stressed gauge area). 125
Figure 4-18: High magnification STEM-EDS mappings of Cr precipitates in CuCrZr (left) and CuCrNbZr_HP (right) alloys after creep tests at 500 ^{o}C and 90 MPa in air (images taken from stressed gauge area). 125

CHAPTER 1

INTRODUCTION

1.1 Precipitate stability under irradiation

1.1.1 Precipitate shrinkage and coarsening

Under thermal exposure conditions the stability of precipitates is controlled by the balance between the diffusion of solute atoms to the precipitate and the thermally-activated release of atoms from the precipitate surfaces. When the rate of the dissolution process exceeds the rate of diffusion to precipitates, the precipitates disappear to maintain the solute atoms in solution (i.e. classic nucleation theory). However, at lower temperatures where a reduced solute concentration is in equilibrium with precipitates, the system attempts to lower its total free energy by the growth of large precipitates at the expense of smaller ones (i.e. Ostwald ripening effect). The driving force for coarsening stems from the interfacial energy and that the rate of coarsening is controlled by volume diffusion [1].

When an alloy containing precipitates is irradiated, two processes occur which perturb the equilibrium conditions set solely by thermodynamics. First, the irradiation can enhance the solute diffusion within the host matrix due to the supersaturation of point defects (vacancies and self-interstitial atoms) compared to thermal equilibrium values; and second, the irradiation can destroy the precipitates by atomic mixing of the precipitate and surrounding matrix atoms, particularly under energetic displacement cascade conditions. New equilibrium conditions are therefore set up which depend on the details of the irradiation environment [2-5]. Figure 1-1 shows a simple Kinetic Monte Carlo (KMC) simulation, which predicts the evolution of two nanocrystals (NCs) of different sizes in a closed box. Figure 1-1 (a) and (b) are for high and medium irradiation temperatures, respectively, presenting conventional Ostwald ripening and inverse Ostwald ripening, while Figure 1-1 (c) is for low irradiation temperatures, since the steady-state solute concentration under ion irradiation becomes so high that NCs can nucleate [6].

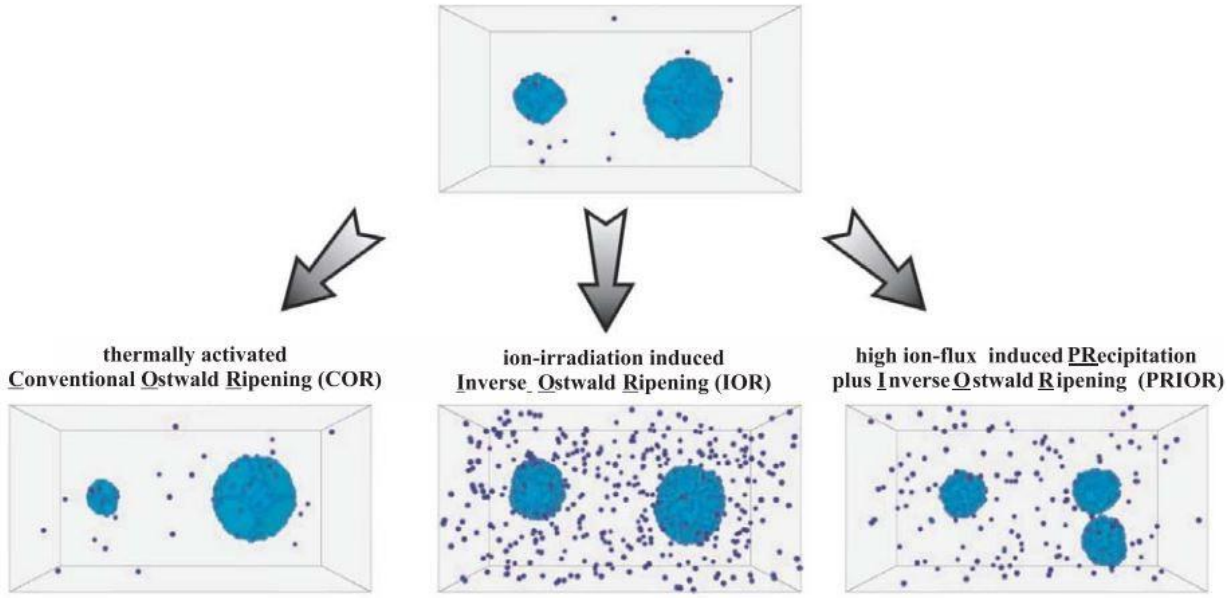


Figure 1-1: Computer simulation. (a) and (b) are for high and medium irradiation temperatures, while (c) is for low irradiation temperatures [6].

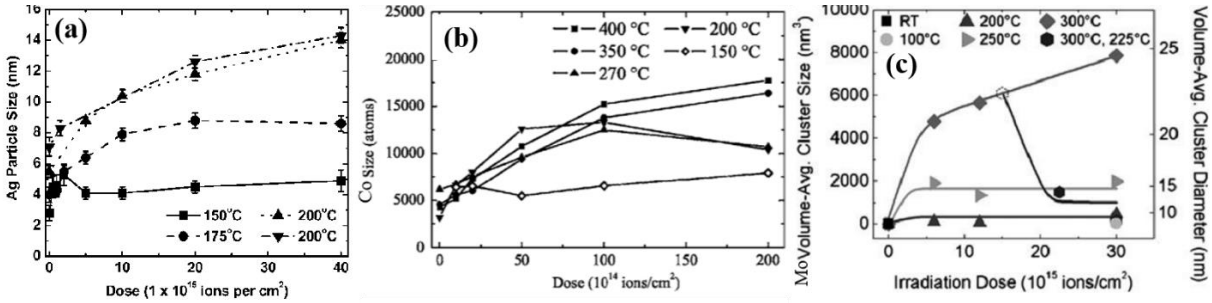


Figure 1-2: Cluster size versus irradiation dose with 1.8 MeV Kr ions at elevated temperatures in dilute (a) Cu-Ag, (b) Cu-Co and (c) Cu-Mo binary alloys [7].

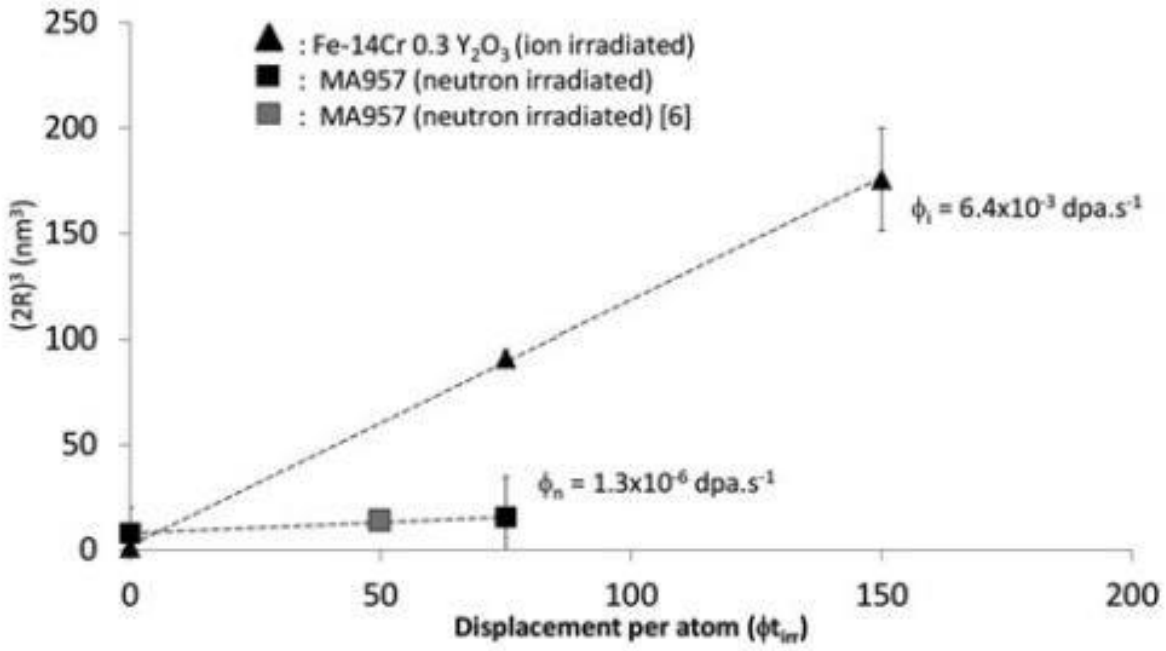


Figure 1-3: Plot of nanoparticle diameter cubed versus the displacement damage dose after ion irradiation at 500 °C and neutron irradiation at 430 °C [8].

For the different irradiation environments, irradiation temperature and displacement damage rate play important roles. Chee et al. [7] have studied phase separation in dilute $Cu_{(1-x)}M_x$ films under irradiation with 1.8 MeV Kr ions at elevated temperatures. They have found that precipitates gradually shrink at low irradiation temperatures due to the dominance of ballistic dissolution and renucleation processes, while at high temperatures precipitates gradually coarsen due to the dominance of radiation enhanced diffusion in this temperature regime. Figure 1-2 shows cluster size versus irradiation dose in dilute Cu-Ag, Cu-Co and Cu-Mo binary alloys. The critical temperature defining shrinkage and growth during irradiation was between 160 and 200 °C at a displacement rate of ~3×10^{-2} dpa/s. Ribis et al. [8] have compared neutron and ion irradiation response of nano-oxides in oxide dispersion strengthened (ODS) materials and found that for a given dose, the nanoparticle kinetics scales as the one third power of the displacement damage rate. Figure 1-3 shows nanoparticle diameter versus the displacement per atom for ion and neutron irradiated oxide dispersion strengthened steel. The growth rate for ion irradiation is roughly 4 orders of magnitude above that corresponding to the lower dose rate neutron irradiation.

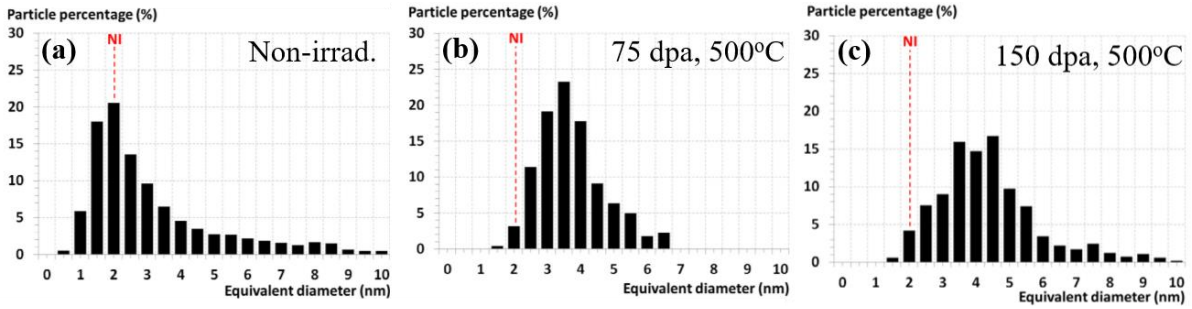


Figure 1-4: Evolution of the nanoparticle distribution during irradiation [9].

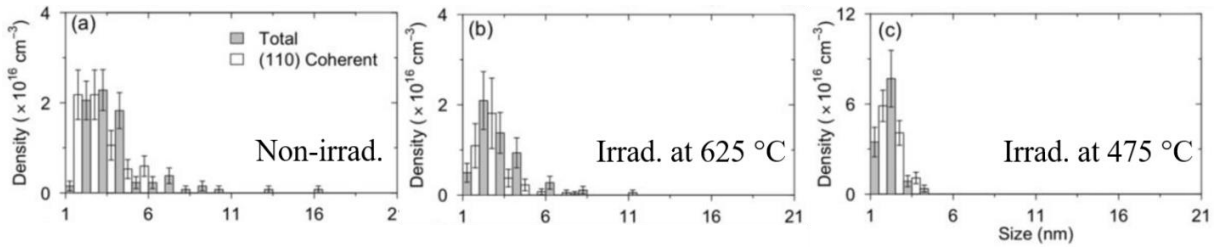


Figure 1-5: Comparison of dispersoid diameter distribution of ferrite and tempered martensite grains [10].

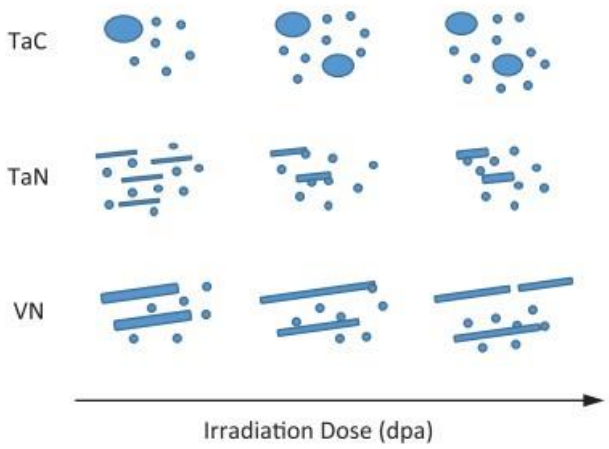


Figure 1-6: Schematic stability/evolution of the TaC, TaN and VN nanoprecipitates under ion irradiation from low to high doses. The tiny spots denote ejected atoms [11].

In addition, precipitate stability under ion irradiations varies according to precipitate size, coherency and composition in different materials. Lescoat et al. [9] found that particle size increased with a decrease in density in ODS ferritic steel after irradiation at 500 °C up to 150 dpa. The histograms presented in Figure 1-4 highlights the evolution of the nanoparticle size distribution from 0 to 75 to 150 dpa. He et al. [12] have studied stability of nanoparticles in ODS steel under heavy ion irradiation at elevated temperature from 300 to 600 °C to a damage level of 100 dpa. The most significant changes observed in their study is a decrease in both nanocluster size and number density at 300°C. However, Chen et al. [10] have found that coherent dispersoids in ODS ferritic/martensitic steel underwent modest size changes under ion irradiation, whereas semi-coherent and incoherent dispersoids would shrink in size and were only observed to remain after higher temperature irradiations. Figure 1-5 compares dispersoid diameter distribution in ferritic (black) and tempered martensite (white) grains before and after irradiation at 625 and 475 °C. Tan et al. [11] have studied the stability of MX-type strengthening nanoprecipitates in ferritic steels under ion irradiation at 500 °C. The stability of TaC, TaN and VN nanoprecipitates manifested differently through either dissolution, reprecipitation and growth. They discovered that smaller particles like TaC and TaN were easier to be dissolved under cascade irradiation, surpassing thermal-activated growth. They further found that particle size and geometry played an important role in particle stability. Despite the similar length between oval-shaped TaC (7.9 nm) and plate-like TaN (8.6 nm), the ultrathin (~1 nm) nature of TaN platelets resulted their significant dissolution. Although VN particles also had plate-like geometry, their "large" size (20.1 nm length by ~7.5 nm thickness) was able to withstand noticeable dissolution. The cascade ejected atoms and irradiation-enhanced diffusivity favored the growth of the particles in length. Figure 1-6 schematically illustrates the stability/evolution mechanisms of TaC, TaN and VN particles under ion irradiation from low to high doses.

For a better understanding of the phase stability of precipitates under irradiations, the comparisons of specific particle size, coherency and composition as well as the irradiation temperature and displacement damage rate are needed.

1.1.2 Coherency loss of precipitates after irradiation

In general, reliable information of coherency between a particle and the matrix can be obtained from conventional Transmission electron microscopy (TEM) analysis. Particle coherency can be judged from Ashby and Brown (AB) imaging methods [13], where the so-called "no contrast line" appears in normal direction to the diffraction $\boldsymbol{g}$ vector under dynamical diffraction conditions. Coherent precipitates are characterized in TEM bright field (BF) images, usually with uniform distribution of spherical shapes. It has been observed that coherent precipitates can grow to quite large sizes while retaining full coherency unless the constrained mismatch between precipitate and matrix lattice parameter is greater than a certain value (~5%). Iwamura and Miura [14] have studied the loss in coherency and coarsening behavior of Al_3Sc precipitates through thermal aging. Based on their TEM and simulation results, AB contrasts in BF images (Figure 1-7) become irregular on aging, suggesting that coherency begins to break down in accordance with particle growth. The energy of the Al/Al_3Sc interface was estimated to be lower for a coherent interface than for a semi-coherent interface, and the difference between the two values is regarded as the energy due to interfacial dislocations, which is consistent with the observation of network dislocations at the semi-coherent particles. Besides thermal aging, cold work or irradiation can also accelerate loss of coherency in precipitates.

Researchers have found that in typical dilute Cu-base binary alloys (Cu-Co and Cu-Fe) coherent precipitates (Co-rich and Fe-rich precipitates) may lose coherency by interaction with point defects or dislocation loops produced directly by electron bombardment [15, 16], fast neutron irradiation [5, 16] and heavy ion irradiation conditions [17, 18]. Images of coherency loss of precipitate in these three conditions are showed in Figure 1-8. We should note that, in the heavy ion irradiation experiments, the initial coherent Co-rich precipitates also became incoherent beyond end of the range (BEOR) as shown in Figure 1-8 (c).

In the in situ electron irradiation experiments [15], original coherent Co-rich precipitates lost the "line of no contrast" when the beam current increased to the maximum value of ~1 μA (3.1×10^{19} electrons/cm^2) at 450 kV and assumed a more complex appearance (the starting current is ~0.1 μA with condenser beam defocused to minimize the radiation damage). Other precipitates seemed to change contrast spontaneously without observable loop migration, suggesting that a dislocation loop had been nucleated directly at the precipitate.

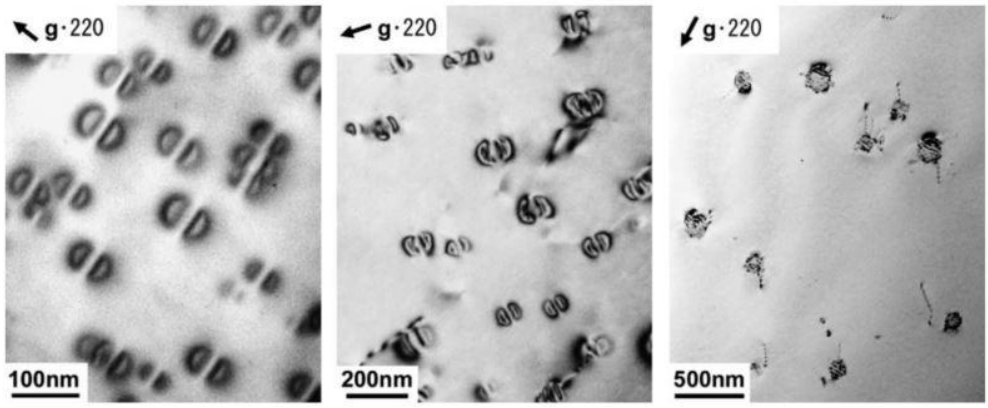


Figure 1-7: Thermal aging induced coherency loss of Al_3Sc [14].

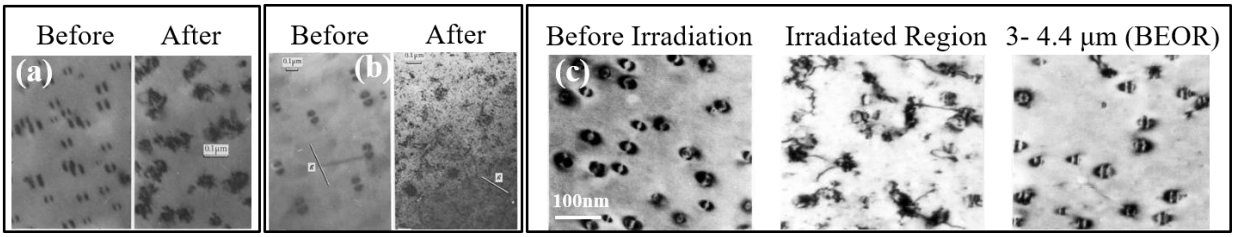


Figure 1-8: Coherency loss before and after (a) electron irradiation [15]; (b) fast neutron irradiation [16] and (c) heavy ion irradiation [18].

As a neutral sink, coherent precipitates act as traps that capture a defect but preserve its identity until it is annihilated by the opposite type defect [19]. The precipitate coherency can be envisioned by considering that a certain volume of matrix (copper) is removed and replaced by a different volume of product phase (Co precipitates). The difference in volume leads to a dilatational strain which is negative, due to the smaller lattice parameter of 'vacancy' type precipitate compared to matrix induced volume change. The interface of the coherent precipitate with the matrix can be modeled as containing a distribution of saturable traps. Figure 1-9 shows the schematic image of coherent and incoherent precipitate with the matrix. Suppose that a prismatic interstitial dislocation loop is introduced with its plane passing through the center of the precipitate. Such a loop is subject to two forces: (1) a force due to its line tension causing it to shrink; (2) a force due to the interaction with the stress field of the precipitate causing the loop to expand or contract, depending on its size relative to that of the precipitate. Two critical precipitate radii emerged from this theory:

$$r_{crit} = \frac{b}{16\pi|\varepsilon|(1-\nu)}\left[\ln\frac{8r_{crit}}{b} + \frac{3-2\nu}{4(1-\nu)}\right] \quad \text{(Eq. 1-1)}$$

$$r^{*} = \frac{b}{8\pi|\varepsilon|(1-\nu)}\left[\ln\frac{8r^{*}}{b} - 1 + \frac{3-2\nu}{4(1-\nu)}\right] \quad \text{(Eq. 1-2)}$$

where **ε** denotes the constrained misfit between precipitate and matrix, ***b*** the Burgers vector of the dislocation loop and **ν** the Poisson ratio of precipitate and matrix (assumed equal).

The quantity r_{crit} can be understood as the minimum precipitate radius when the stress on an interface loop due to the elastic field of the precipitate (tending to expand the loop) just balances the self-stress of the loop (tending to shrink it) and r^{*} as the maximum precipitate radius beyond which the precipitate tend to loss coherency due to lower energy of the incoherent precipitate than the coherent one of the same size. One important concept to note is that a precipitate, whatever its size, possessing an interfacial loop always has lower energy than the system consisting of fully coherent precipitate and an infinitely separately loop [16].

Here, we examine the behavior of two typical dilute Cu-base binary alloys (Cu-1%Co and Cu-1%Fe, wt.%) as example:

For Cu+Co, $|\varepsilon| = 0.013$ and $r_{crit} = 3.2$ nm, $r^* = 6.0$ nm

For Cu+Fe, $|\varepsilon| = 0.008$ and $r_{crit} = 5.8$ nm, $r^* = 13.1$ nm

The calculation results for Cu+Co condition are shown in Figure 1-10, where r_0 is the radius of the precipitate particle and r_l is radius of the dislocation loop. At $r_{crit} = 3.2$ nm a loop around the precipitate will expand, and at $r^* = 6.0$ nm creation of a dislocation loop around the coherent particle gives a decrease in energy.

In the electron irradiation experiments [16], the observed radii are 2.5 nm for Cu+Co and 7.0 nm for Cu+Fe. Conversely, in the case of neutron irradiation, the observed critical radius for coherency loss decreased as the fast neutron dose increased. It seems likely that if the dose were sufficiently high and the precipitate distribution suitably coarsened the theoretical critical sizes would be observed.

Based on the above neutron and electron irradiations, and the fact that 'vacancy' type precipitates require interstitial loops, two established mechanisms were proposed:

(1) Interstitial loops move by glide and conservative climb to equilibrium positions where they act directly as interfacial loops.

(2) Free interstitials are trapped within the precipitates due to the high attractive interaction energy and subsequently agglomerate into strain-relieving interstitial dislocation loops.

1.1.3 MD Simulations and experiments on defects migration behavior in fcc and bcc matrix

Energetic primary recoil atoms from fast neutron irradiation produce point defects and defect clusters. The surviving defects after the in-cascade spontaneous recombination of interstitials and vacancies are mainly responsible for the radiation damage. Self-interstitial mobility as well as defect cluster stability and mobility play key roles in the subsequent fate of defects in the overall microstructural evolution under irradiation.

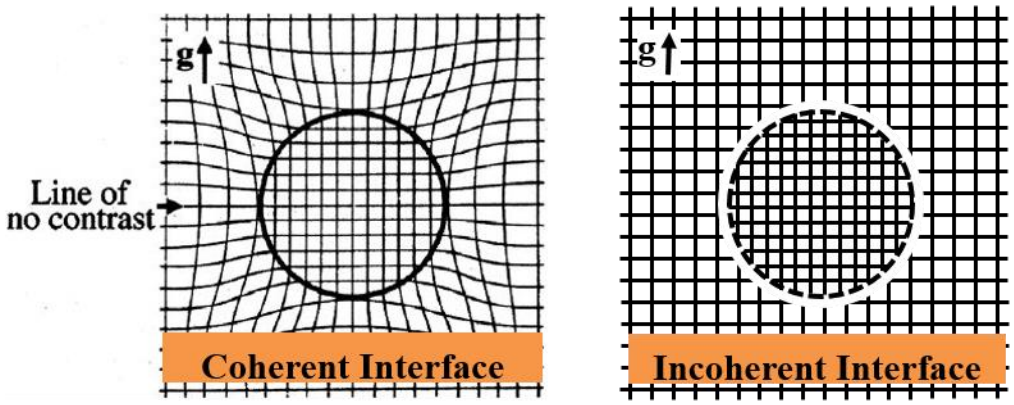


Figure 1-9: Schematic image of 'vacancy' type coherent precipitate and incoherent precipitate with the matrix [17].

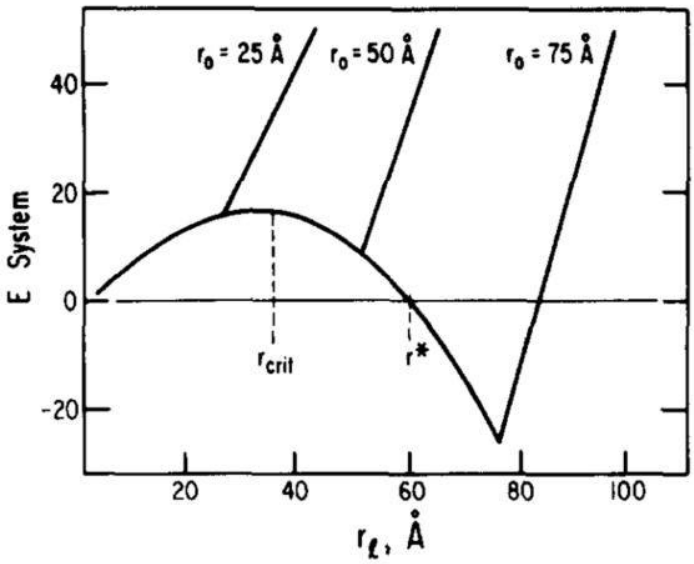


Figure 1-10: Energies of coherency loss versus radius of dislocation loop [16].

Some molecular dynamics (MD) simulations of defect clusters in face centered cubic (fcc) and body centered cubic (bcc) metals [20-22] predict that defect clusters with sizes from ~5 to >50 vacancies or self-interstitial atoms (SIAs) may be highly mobile and exhibit predominantly one-dimensional (1D) migration behavior. Wirth et al. [23] have done the MD simulations over a wide temperature range on α-Fe matrix and revealed that single interstitial migration is a two-step process involving rotations out of and into the ground-state <110> dumbbells configuration and translation of <111> dumbbells through the crowdion saddle-point configuration. Self-interstitial clusters are highly mobile and they migrate in a highly anisotropic, one-dimensional manner along their <111> orientation. Osetsky et al. [21] determined the most stable interstitial clusters and dislocation loops in α-Fe are glissile sets of <111> or <100> crowdions. These clusters and loops perform a thermally activated, 1D motion in the crowdion direction. Stable interstitial clusters and dislocation loops in Cu can be either glissile or sessile, and small glissile clusters perform thermally activated, 1D motion along <110> directions. Later, Osetsky et al. [20] studied thermally activated motion of clusters of self-interstitials in Fe and Cu through MD simulations over the temperature range of 180-1000 K. They found that the smallest clusters ($N \leq 3$) exhibit both 3D and 1D mechanisms of mobility. Clusters with $4 \leq N \leq 91$, being sets of parallel crowdions, are 1D mobile in the direction of the corresponding crowdions. Point defect clusters containing more than 100 SIAs in Cu and 300 SIAs in Fe have significantly reduced mobility.

Heinisch et al. [22] have reported the possibility of a transition from 1D to 3D defect cluster diffusion through Kinetic Monte Carlo (KMC) studies. Here, the diffusion of 1D gliding loops can be occasionally modified by a transient conversion to 2D migration due to conservative climb by dislocation core diffusion within a plane transverse to their 1D glide direction. The KMC results were compared to an analytical description of this diffusion mode in the form of a master curve relating the normalized sink strength to the disturbance of 1D diffusion. Based on this analysis, 1D glissile diffusion was predicted to be predominant for low sink strengths whereas high sink strengths induced interruptions of this glissile behavior and caused the overall diffusion to approach 3D random walk diffusion behavior due to frequent Burgers vector changes of the migrating defect clusters.

The mobile defects produced by irradiation are absorbed by immobile sinks, such as voids, dislocations, dislocation loops and grain boundaries, or second phases (precipitates) in the grains.

The interactions of migrating defects with various microstructural features are represented by the 'sink strength' k^2 of each type of sink. The contribution of a certain sink type to the total sink strength is a function of the sink type, size, shape and concentration (sink density). The sink strength is proportional to the inverse of the migrating defect's mean free path. For voids or second phase precipitates with radius R and number density N the sink strength k_3^2 for interactions with interstitial clusters diffusing by pure 3D migration is proportional to $4\pi RN$ (for relatively small R and N). On the other hand, if the clusters in the same system are migrating by pure 1D motion, the sink strength k_1^2 is proportional to $6\pi^2 R^4 N^2$ [22]. Note, the difference in sink strength results solely from the difference in diffusion dimensionality of the migrating interstitial clusters. The nature of the transition from pure 1D to pure 3D kinetics depends on the type of disruption of 1D motion that is involved, i.e., whether pure 1D gliding of the defect is interrupted by a change of glide direction (1D/3D-DC) or by a transverse climb excursion (1D/3D-TC). Figure 1-11 is a schematic illustration of defect migration as random walks on a 3D lattice: (a) 'Pure 3D' consists of a 3D random walk of equally probable hops to any nearest neighbor site. (b) 'Pure 1D' consists of a 1D random walk of equally probable hops along the same close-packed direction, as by gliding crowdion defects. (c) '1D/3D-DC' consists of a series of segments of 1D random walks in different random directions, as by crowdion clusters gliding along close-packed directions that occasionally change their glide direction. (d) '1D/3D-TC' consists of a series of segments of 1D random walks, all along the same direction, occasionally shifted transversely in two dimensions such as gliding interstitial loops that occasionally migrate by conservative climb.

Since vacancy clusters become thermally unstable at temperatures above ~150 °C (recovery "stage V") due to typical binding energies of ~1 eV whereas SIA clusters are typically stable up to temperatures above ~700 °C due to SIA cluster binding energies of >3 eV [21], the diffusion behavior of glissile SIA clusters are of particular importance for elevated operating temperatures relevant for nuclear energy applications. However, experimental confirmations of highly glissile 1D migration of defect clusters are incomplete, and mainly consist of occasional observations of 1D motion of SIA [24] or vacancy [25] clusters.

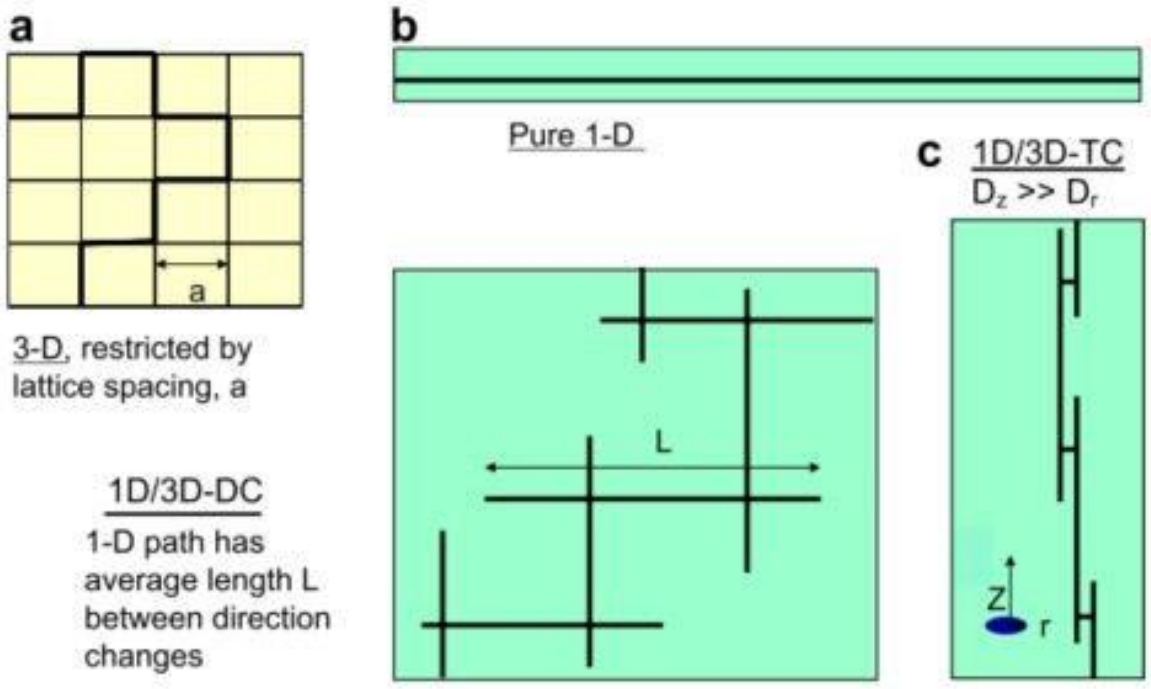


Figure 1-11: Schematic illustration of the nature of 1D migration interrupted both by direction change (1D/3D-DC) and by transverse climb excursions (1D/3D-TC) [22].

1.1.4 Motivation and objectives

Theme I focuses on fundamental understanding of phase stability of nanoscale precipitates within and beyond the ion displacement damage region in irradiated dilute Cu-base binary alloys.

The primary goal for theme I is to correlate the stability of precipitates to irradiation-induced defect migration behavior through various irradiation conditions with respect to temperature and damage dose. Phase stability of nanoscale precipitates is of key importance for the design of radiation resistant materials, yet relatively little fundamental information is available regarding the role of particle size, coherency and composition on dynamic stability during irradiation. A variety of irradiation-induced mobile defects and small defect clusters interact with precipitates and other microstructural features. Therefore, it's essential to understand radiation effects on the initial coherent precipitates. Through various temperature and damage dose ion irradiation experiments, TEM characterization and EDS mapping, the coherent precipitate stability after irradiation can be assessed.

Moreover, some molecular dynamics (MD) simulations have predicted that in face centered cubic and body centered cubic metals [20-22], defect clusters with sizes from ~5 to >50 vacancies or self-interstitial atoms (SIAs) may be highly mobile and exhibit predominantly one-dimensional (1D) migration behavior. However, experimental confirmations are incomplete, and mainly consist of occasional observations of 1D motion of SIA [24] or vacancy [25] clusters. In this research thrust area, initially coherent precipitates produced by thermal treatment may act as diagnostic indicators to monitor the radiation defect migration behavior, since the interaction between radiation defects and coherent precipitates produces loss of precipitate coherency.

1.2 Development of high strength high conductivity materials

The anticipated intense heat fluxes at the first wall and divertor in proposed DEMO fusion power plants (up to ~10 MWm^{-2} at steady state, with higher transient heat fluxes) are expected to require the use of high strength, high conductivity substrate structures. Due to their capability to simultaneously achieve high thermal conductivity (>300 $Wm^{-1}K^{-1}$) and high strength (>250 MPa yield strength) several types of copper alloys have been explored for demanding high heat flux applications in current and near term fusion devices including ITER (International Thermonuclear

Experimental Reactor). A variety of traditional physical metallurgy approaches are available to achieve high strength in metals, including deformation hardening, planar interface (i.e. grain or twin boundary) hardening, solution hardening and precipitation hardening. However, solute additions can cause dramatic reductions in the thermal conductivity of copper and therefore are generally not suitable for simultaneous optimization of strength and conductivity of Cu alloys.

Figure 1-12 compares the room temperature yield strength and thermal conductivity that has been achieved in a variety of high performance copper alloys with the corresponding values for Type 315 austenitic stainless steel and pure copper [26]. Generally, there's a tradeoff between high strength and high conductivity, with the highest strength Cu alloys (>1 GPa yield stress) having thermal conductivities <250 $Wm^{-1}K^{-1}$ and the highest thermal conductivity alloys (>350 $Wm^{-1}K^{-1}$) having yield strengths below 350 MPa in as-wrought or solutionized and aged conditions. Some of these copper alloys also contain elements that exhibit undesirable fusion neutron-induced activation (Nb) or introduce undesirable chemical hazards (Be).

1.2.1 Cu-Cr binary alloys

Copper and copper alloys are widely used for high strength, high conductivity applications near room temperature because of their excellent electrical and thermal conductivities, outstanding resistance to corrosion, ease of fabrication as well as good strength and fatigue resistance [27]. The optimized strength and conductivity near room temperature for copper alloys is typically achieved by introducing a small volume fraction of uniformly dispersed nanoscale (d, 3~10 nm) precipitates or dispersoids, involving precipitates produced by high temperature solution anneal plus intermediate temperature aging, or inert dispersoids such as fine-scale oxides produced by powder metallurgy approaches). For a given volume concentration of spherical particles ($f=\pi Nd^3/6$), where N is the number density and d is the particle diameter), the yield strength increase due to 'dispersoid hardening' obstacles that impede dislocation movement is given by $\sigma_y=\alpha\mu b(6f/\pi)^{0.5}/d$, where α is the normalized obstacle strength, μ is the shear modulus and b is the Burgers vector of the gliding dislocation [26]. The corresponding thermal and electrical conductivity can exhibit a complex dependence on precipitate size and density at small particle sizes, but in many cases the conductivity (k_{th}) can be well described by the Maxwell equation $k_{th}=k_m[(1-f)/(1+f/2)]$ where k_m is the matrix conductivity. Therefore, the optimized strength and conductivity near room temperature

for copper alloys is typically achieved by introducing a small volume fraction (f~10%) of nanoscale precipitates or dispersoids. Since chromium does not form intermetallic compounds with copper, it precipitates the form of Cr particles from a supersaturated Cu matrix after thermal aging. In investigations of the Cr precipitates from supersaturated Cu-Cr solid solution decomposition, much attention has been paid to the shape and the structure of the precipitates, and for a long time, the debate about their crystallography and orientation relationship with the fcc Cu matrix has no unanimous agreement.

The equilibrium crystallographic structure of Cr is bcc, but it has been proposed by several researchers that Cr particles are coherent with the fcc Cu matrix in the early stage of precipitation [28, 29]. Part of the enigma was finally solved by Fuji et al. [30]; they have observed that the "no contrast lines" varied in orientation in an aged specimen and confirmed that Cr particles can have the Kurdjumov-Sachs (K-S) or Nishiyama-Wassermann (N-W) relationships satisfying the invariant-line condition. In any case, nano-scale Cr precipitates induce large lattice distortions that make them difficult to observe by TEM. Chbihi et al. [31] have conducted TEM as well as atom probe tomography (APT) to explore the size, shape, chemical composition and density of the Cr precipitates and achieved reliable information. They have observed three kinds of Cr precipitates coexisting in the microstructure from bright-field TEM images after isothermal aging on Cu-1Cr-0.1Zr (wt.%) alloy at 440 °C for 10 h: i) spherical and face centered cubic (fcc) coherent precipitates with a cube-on-cube orientation relationship (OR) with the copper matrix; ii) ellipsoids and body centered cubic (bcc) with a NW-OR; iii) plate-shaped and bcc with a K-S orientation relationship. They have further stated that bcc Cr-rich precipitates with the N-W OR at the early stage of precipitation would have the size below 10 nm. Figure 1-13 shows TEM images of the Cu alloys aged for 10 h at 713 K. Figure 1-13 (a) and (b) are the selected area electron diffraction pattern (SAED) and the indexation, Figure 1-13 (c) is a BF image including three different kinds of precipitates and contributed to the SAED pattern, Figure 1-13 (d), (e) and (f) are three different kinds of Cr-rich precipitates according to the above description.

1.2.2 Commercial CuCrZr and ODS GlidCop Al25 alloys

In recent decades, CuCrZr alloys are being considered as the potential heat sink for the large-scale fusion plasma device ITER due to their high strength and high conductivity properties.

The high electrical conductivity is due to the very low solubilities of Cr and Zr in Cu at aging temperatures (i.e., very little solute remains dissolved in the Cu matrix after aging), whereas the excellent strength is attributed to precipitation and particle-dispersion strengthening mechanisms that are achieved by classic solution quench and aging techniques [32]. Also, the addition of Zr has been reported to mainly getter harmful impurity atoms like oxygen away from grain boundaries, thus can improve mechanical properties at intermediate temperatures without loss of the good electrical and thermal conductivities [33]. In order to control the microstructure and improve the properties of such alloys and optimize the production techniques, it would be of great value to identify the composition of the phases in the CuCrZr alloy. Zeng and Hamalainen have conducted theoretical [34] and experimental [35] investigations showing that three phases (Cu, Cr and Cu_5Zr) should exist in CuCrZr system, and these three phases have been widely agreed reported in the Cu-(0.1-0.3)Cr-0.15Zr (wt.%) alloys.

The mechanical properties of CuCrZr alloys strongly depend on the thermomechanical treatment for producing the Cr precipitates. In service, both of the first wall and divertor components of ITER will be exposed to an intense flux of fusion (14 MeV) neutrons while being subjected to thermo-mechanical stresses. Experimental investigations have demonstrated that neutron irradiation of prime aged CuCrZr at temperatures below ~200 ^{o}C leads to a substantial increase in strength, formation of a tensile instability, and a severe loss of work hardening ability and uniform elongation [26]. For a certain volume concentration of spherical particles, when the precipitates in the prime aged condition are in high density, they will be too small in size and thus too weak to serve as impenetrable Orowan obstacles to dislocation motion during deformation. This is generally based on the observation that the deformation channels observed in irradiated CuCrZr after tensile deformation are clear of Cr precipitates as well as defects and dislocations. This indicates the Cr precipitates will be sheared by the passing of dislocations due to no promotion of any work hardening [36].

On the other hand, neutron irradiated ODS GlidCop Al25 are not expected to suffer from pronounced volumetric swelling and softening because of the high density of alumina particles, which are the source of strengthening as well as swelling resistance, are thermally stable and are resistant to ballistic dissolution [37, 38]. To achieve optimized room temperature strength and

thermal conductivity in CuCrZr alloys, Cr matrix particles with an average size of 7~8 nm and a density of 10^{22} m^{-3} were targeted.

1.2.3 NASA CuCrNb alloys

Since its founding, NASA has been dedicated to the advancement of aeronautics and space science. GRCop-84 (Cu-8Cr-4Nb, at.%) was designed specifically for rocket engine main combustion chamber liners, and offers potential for high-heat-flux applications up to approximately 700 ^{o}C. GRCop-84 is a copper-based alloy with excellent elevated temperature strength, good creep resistance, long low-cycle fatigue lives and enhanced oxidation resistance. It also has a lower thermal expansion than copper and many other low-alloy copper-based alloys. GRCop-84 can be manufactured into a variety of shapes such as tubing, bar, plate, and sheet using standard production techniques and requires no special production techniques. To achieve a structural alloy with a combination of high strength, high conductivity and good long-term stability at high temperatures, a supersaturated CuCrNb alloy was designed with the high melting point intermetallic compound Cr_2Nb to precipitation strengthen the Cu matrix. By using the intermetallic phase, it was hoped that the precipitates would not coarsen readily and lose their strength as with Cu-Cr alloys do when exposed to elevated temperatures, particularly above 500 ^{o}C [39, 40].

Ellis et at. [39] used a chill block melt spinning (CBMS) method on Cu-based alloys containing (2-10)Cr-(1-5)Nb, at.% at a 2:1 atomic ratio. They found that the materials possess electrical conductivities in excess of 90% that of pure Cu at 200 ^{o}C and above, indicating the high thermal conductivities these alloys at temperatures above 200 ^{o}C. Besides, the strengths of the Cu-Cr-Nb alloys were much greater than Cu, Cu-0.6Cr, NARloy-A, and NARloy-Z in the as-melt spun condition. The tensile strengths of the consolidated materials were less than Cu-Cr and Cu-Cr-Zr below 500 and 600 ^{o}C, respectively, but were significantly better above these temperatures. The microhardness measurements on aged samples and the growth of precipitates have showed long term stability of the Cu-Cr-Nb alloys, indicating that the alloys overage rapidly, but do not suffer much loss in strength during aging between 10 and 100 h. The loss in strength from peak strength levels is significant, but nevertheless the strength remains acceptably high. Their TEM work on aged and consolidated materials showed that the precipitates do coarsen considerably, but remain in the submicron size range.

However, the CuCrNb alloys in their study can only be produced using rapid solidification technology. Conventional casting results in Cr_2Nb precipitates that grow to well over 1 cm in diameter during slow cooling. So far, the alloys have been successfully produced using CBMS and conventional gas atomization. Conventional argon gas atomization was chosen because it offered a large industrial base, relatively low cost, volume production capability, and a high cooling rate. Elemental copper, chromium, and niobium are melted to produce a uniform molten alloy. The molten metal is atomized to produce a fine powder. For extrusion and hot isostatic pressing (HIPing), -140 mesh (<106 μm) powder is used. Typically, this powder has a mean powder size around 40 μm. For vacuum plasma spraying, a finer powder is desired. The -270 and -325 mesh (<53 and <44 μm) have been used with great success.

Three conventional consolidation techniques have been successfully used to produce GRCop-84. At NASA Glenn Research Center, direct extrusion of the powder to a round or rectangular shape and HIPing to simple shapes have been examined. Both consolidation methods produce fully dense material NiCrAlY inner layer and functional gradient material. The sprayed powder was fully densified after spraying and HIPing. Once the powder is consolidated, the alloy can be processed like any other high-strength copper alloy. However, this fabrication method consumes a large amount of energy, which means it is expensive and not environmentally friendly.

1.2.4 Grain boundary embrittlement and sliding limit high temperature applicability

One problem related to the CuCrZr alloy is fast coarsening rate of Cr-rich precipitates at temperatures greater than 400 ^oC [30, 31, 41-44]. The existing CuCrZr alloys also suffer from poor creep resistance at 400 ^oC and higher temperatures due to high dislocation power law creep rate and grain boundary sliding [26]. This poor creep property limits its application as a structural material at higher temperature (>400 ^oC). In contrast, Cu-8Cr-4Nb (at. %) alloy has demonstrated excellent high temperature creep resistance due to the formation of large grain boundary Laves_Cr_2Nb precipitates [40, 45-47]. However, because of the high atomic ratio of Nb to Cr in this alloy, all of the Cr is consumed to form the Cr_2Nb precipitates and no Cr is available to form the matrix Cr precipitates. In addition, the large amount of Nb and Cr in the Cu-8Cr-4Zr alloy requires expensive powder metallurgy methods in order to avoid the formation of large Cr_2Nb precipitates that would form in the melt for conventional ingot metallurgy processing. Figure 1-14

shows all current commercially available high strength, high conductivity Cu alloys would be subject to significant thermal creep deformation when they are operating at temperatures above 300~400 ^{o}C for long time.

1.2.5 Motivation and objectives

Theme II aims to analyze and understand the mechanical deformation mechanisms, especially regarding elevated temperature creep resistance, of newly designed CuCrNbZr alloys compared to commercial CuCrZr alloys (the 1st heat contains undesirable impurities, worse thermal conductivity than this new heat).

The objective of this theme is to carefully characterize a new CuCrNbZr alloy that was specifically designed using computational thermodynamics to produce improved high temperature thermal creep strength. The characterization will include macroscopic physical and mechanical strength properties as well as crystallographic microstructures of precipitates in the matrix and at grain boundaries. Precipitation hardened commercial CuCrZr alloys have been considered as promising high heat flux structural due to their high strength and high conductivity properties at room temperature. However, these Cu alloys suffer poor creep resistance at 400 °C due to high dislocation creep rate and grain boundary sliding. Yang et al. [48] has developed a new CuCrNbZr alloy with the aid of computational thermodynamics. Their design strategy was to produce large Cr_2Nb-type Laves precipitates to pin grain boundaries and a high density of finer Cr-rich precipitates to strengthen the matrix and serve as radiation defect recombination centers. This desirable multi-modal precipitate distribution has been predicted according to the solidification path simulation and confirmed by TEM observations. Electrical conductivity and mechanical properties will be screened in this part compared with the existing commercial CuCrZr alloys. Precipitate stability after thermal creep will also be investigated. These experimental observations will be compared to existing models for thermal creep deformation to assess the potential for developing a robust Cu alloy that exhibits very high thermal stability and creep strength.

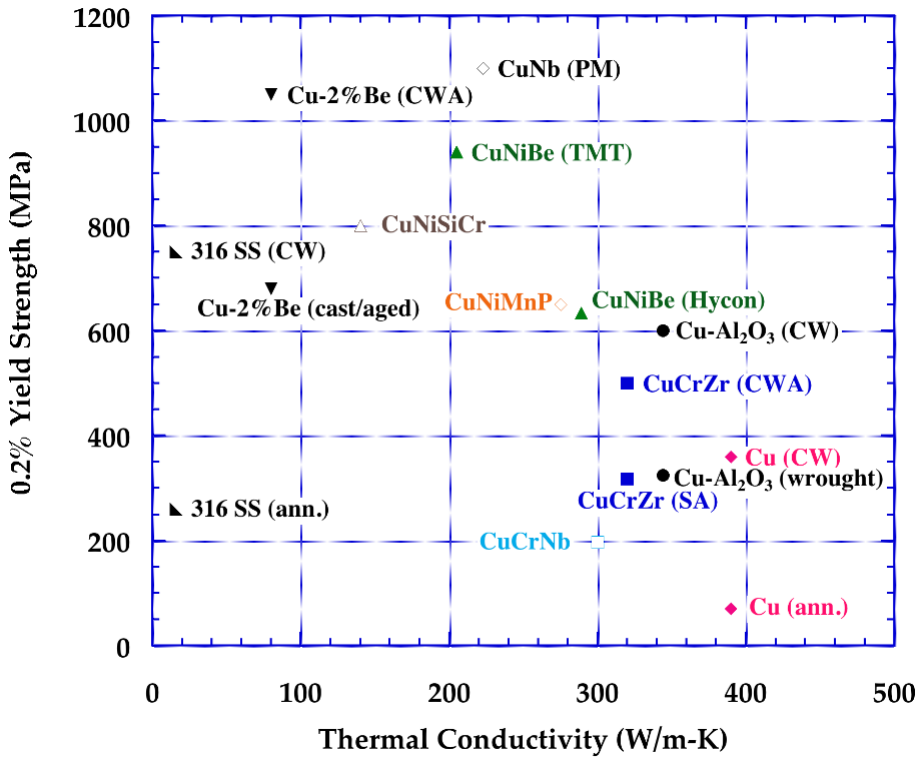


Figure 1-12: Room temperature strength and conductivity of selected high-performance Cu alloys [26].

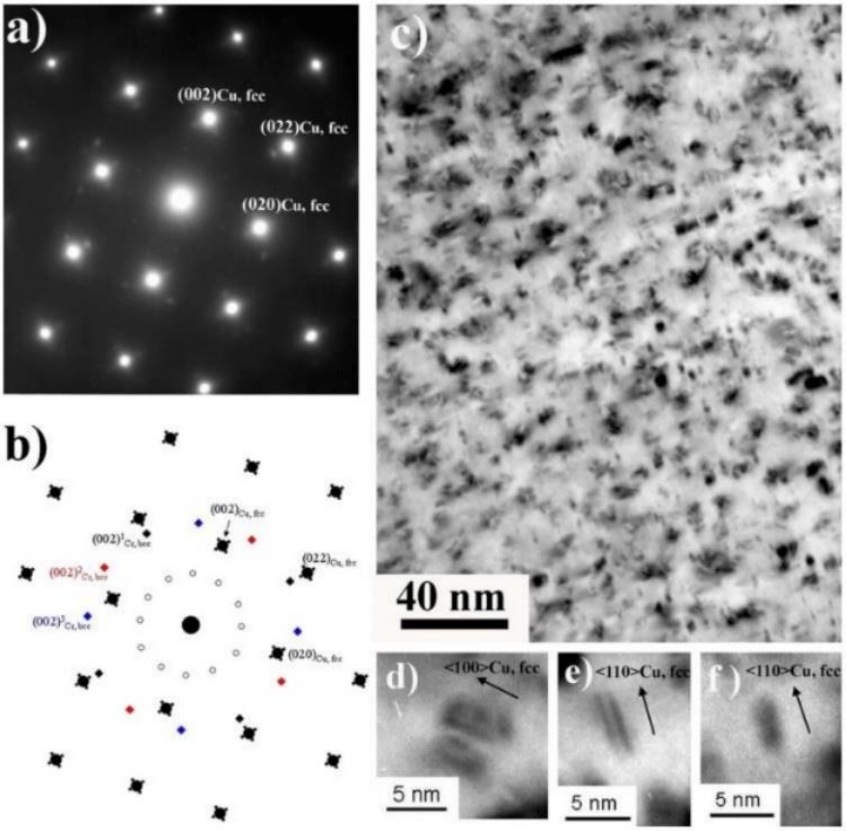


Figure 1-13: TEM images of the Cu alloy aged for 10 h at 440 ºC [31].

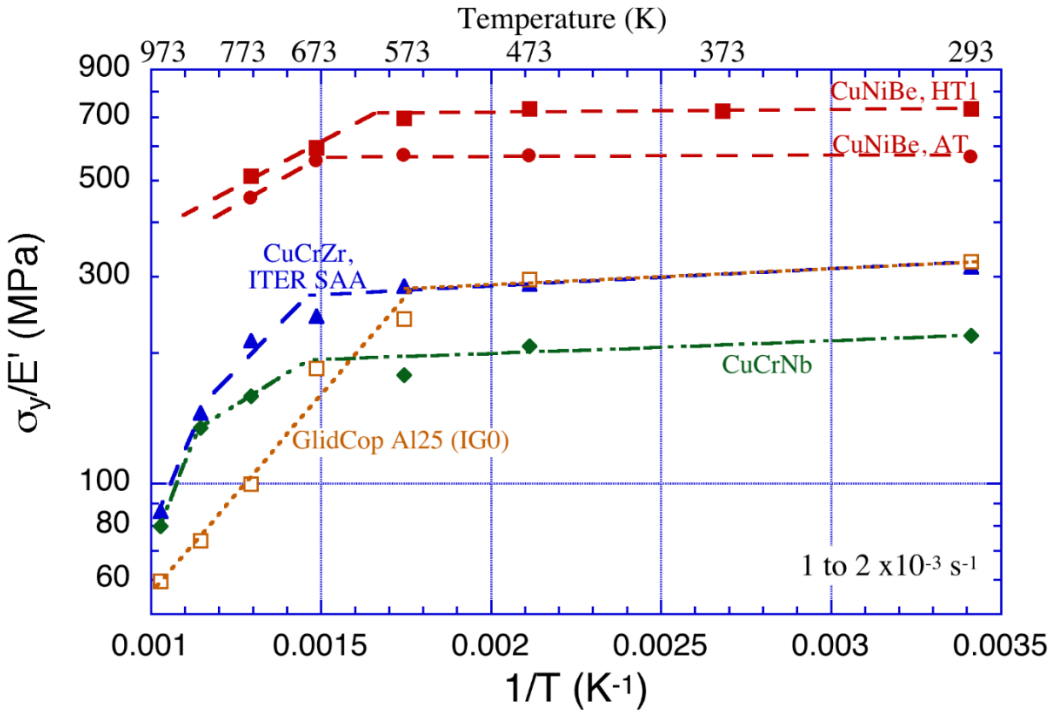


Figure 1-14: Yield strength (corrected for temperature-dependent elastic modulus, *E'=E(T)/E(20 °C))* versus reciprocal temperature for several copper alloys [26].

CHAPTER 2

METHODS AND TECHNIQUES

This work involves irradiation experiments and post-irradiation examinations using microscopy and specialized testing techniques. This chapter describes the sample description (Chapter 2.1), ion irradiation (Chapter 2.2), TEM (Chapter 2.3), electrical resistivity measurement (Chapter 2.4), mechanical tests (Chapter 2.5), and other microstructure characterization (Chapter 2.6).

2.1 Sample description

2.1.1 Dilute Cu alloys

In this work, two typical Cu-base binary alloys (1%Co and 1%Fe, at.%) were selected to initially produce uniformly distributed coherent Co- and Fe- rich precipitates with different sizes and number densities. Two plates of high purity Cu-Co and Cu-Fe binary alloys were purchased from Sophisticated Alloy Inc. with a nominal specification of 99.07% Cu:0.93 wt.% Co, and 98.98% Cu:1.02 wt.% Fe. However, the large melting point difference between Fe and Cu led to non-uniform distribution of solute Fe, thus, the size distribution of precipitates produced during thermal aging was nonuniform. Later, high purity Cu-1%Fe with minor Zr (98.94:0.9:0.16 wt.%) was made by Oak Ridge National Laboratory to overcome this problem. Commercial CuCrZr, Kabelmetal alloys were used as the third dilute Cu alloy, with the initial coherent Cr precipitates uniformly distributed in the matrix. Chemical concentrations of the three dilute Cu-base alloys are listed in Table 2-1. To produce well-proportioned coherent Co- and Fe-rich precipitates in the Cu matrix with different sink strengths (i.e. different precipitate size and densities), the specimens were cut into pieces and sealed in a quartz tube with an inert argon atmosphere (to protect against oxidation) in preparation for heat treatment. The conventional precipitation treatment typically consists of homogenizing the alloy at high temperatures, a fast quenching process to room temperature to retain the solute supersaturation effectively from high temperature, followed by a final aging treatment at intermediate temperature with subsequent air cooling (a.c.). The dilute Cu-1%Co and

Cu-1%Fe binary alloys were solutionized (1000 ℃), water quenched (w.q.) and thermal aged to produce well-proportioned coherent precipitates. Precipitate number density and diameter values, which will be shown in detail later, were calculated through TEM-BF and EDS. Table 2-2 shows the details of the heat treatment conditions for these dilute Cu base alloys. Figure 2-1 shows three typical coherent Co- and Fe-rich precipitates with "no contrast lines" normal to the $\boldsymbol{g}$ vectors of CC1, CC2 and CFZ-0 and the elemental mappings of Cu, Co and Fe in the thermal aged conditions according to Table 2-2; the insert images in this figure show SAED patterns for the TEM BF images. Since there are more than one different thermal treatment processes for the Cu-Co and Cu-Fe alloys we named sample CC1 as Cu-Co aged at 600 ℃ for 12 h, CC2 as Cu-Co aged at 625 ℃ for 12 h, CC3 as Cu-Co aged at 625 ℃ for 18 h, CC4 as Cu-Co aged at 625 ℃ for 69 h, CFZ-0 as Cu-Fe aged at 600 ℃ for 4 h, CFZ as Cu-Fe aged at 600 ºC for 15 h, CCZ as the only CuCrZr alloy in this research, was aged at 475 ºC for 2 h.

Table 2-1: Chemical composition of four dilute Cu alloys (wt.%).

Alloys	Co	Fe	Cr	Zr	Cu
Cu-1%Co	0.93	-	-	-	Balance
Cu-1%Fe-0	-	1.02	-	-	Balance
Cu-1%Fe (Zr)	-	0.9	-	0.16	Balance
Cu-0.8%Cr (Zr)	-	-	0.78	0.13	Balance

Table 2-2: Pre-ion irradiation heat treatment.

Alloys (wt.%)	Heat ID	Solution annealing	Cooling	Aging
	CC1	1000 ºC/1 h	w.q.	600 ºC/12 h
Cu-1%Co	CC2	1000 ºC/1 h	w.q.	625 ºC/12 h
	CC3	1000 ºC/1 h	w.q.	625 ºC/18 h
	CC4	1000 ºC/1 h	w.q.	625 ºC/69 h
Cu-1%Fe	CFZ-0	1000 ºC/1 h	w.q.	600 ºC/4 h
Cu-1%Fe	CFZ	1000 ºC/1 h	w.q.	600 ºC/15 h
Cu-0.8%Cr	CCZ	970 ºC/20 min	w.q.	475 ºC/2 h

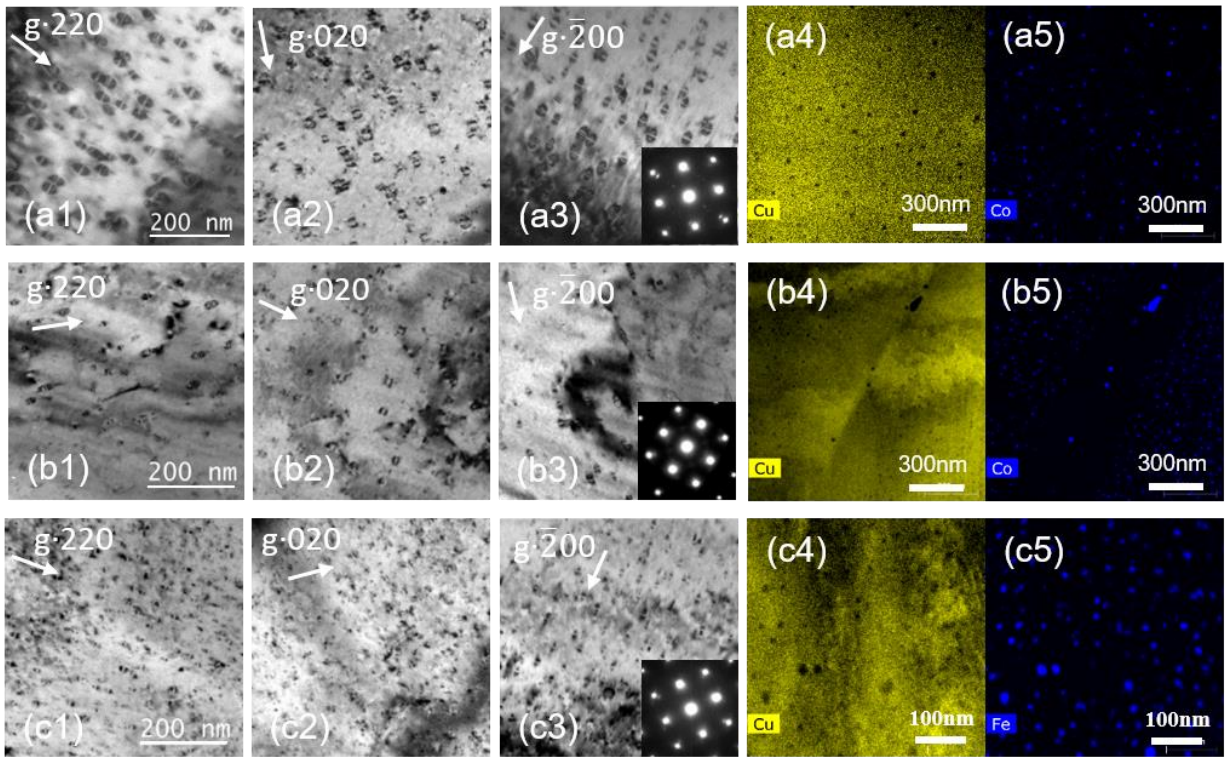


Figure 2-1: TEM bright-field images with inset diffraction patterns and individual elemental mappings of Cu, Co and Fe in (a) CC1; (b) CC2 and (c) CFZ-0 alloy.

2.1.2 CuCrNbZr alloys

To design new high performance Cu alloys with a multimodal precipitate distribution tailored for improved creep resistance, matrix hardening concepts associated with the commercial CuCrZr and oxide dispersion strengthened Cu-Al_2O_3 alloys were merged with grain boundary creep hardening concepts demonstrated in the NASA CuCrNb alloys, i.e., coarse precipitates at grain boundary and fine precipitates in the matrix in order to provide simultaneous resistance to diffusional creep (grain boundary sliding) and dislocation climb (power law creep) processes, respectively, that are calculated [26] to be the predominant contributors to thermal creep in Cu alloys at 300-500 ℃. Computer coupling of phase diagrams and thermo-chemistry, i.e., the CALPHAD approach [49] was used to aid the accelerated alloy design for specific compositions and heat treatments. In this approach, the Gibbs free energy of individual phases is modeled based on crystal structure, defect type and phase chemistry. The details of the computational thermodynamic calculation path are given elsewhere [48]. Figure 2-2 shows the solidification path of this alloy, which is featured by three steps. The first step is the solidification of Cr_2Nb from liquid. The size of this Cr_2Nb precipitate formed during this step is relatively large (due to rapid kinetics at high temperature) so that it can pin the grain boundary during the subsequent thermomechanical treatment. The amount of Cr_2Nb phase produced during this step is around 2 mol.%. The second step is solidification of Cu from liquid. The Cu amount solidified during this step is more than 90 mol.%, therefore, it is the dominant matrix phase of the fabricated alloy. The last step is the eutectic solidification of Cu and Cr. Although the Cr phase is desired to form matrix precipitates during a subsequent aging step, excessive Cr addition can lead to relatively large Cr particle formation in the liquid. Therefore, the amount of Cr needs to be carefully controlled. The Nb addition is subjected to Cr/Nb>1 but can still produce sufficient precipitates of Cr_2Nb. The CuCrNbZr ternary alloy was confirmed by optical microscopy to produce coarse precipitates at grain boundaries and by TEM characterizations to produce fine Cr-rich precipitates in the matrix, as shown in Figure 2-3.

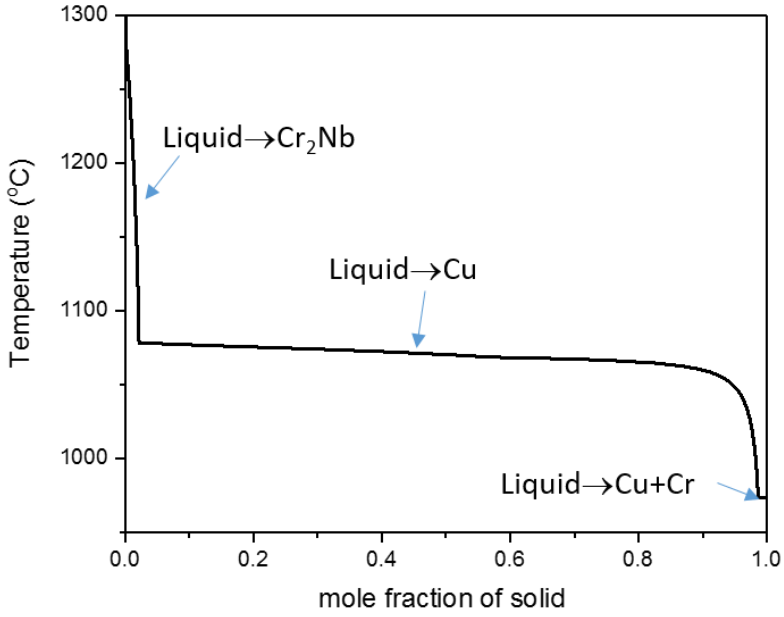


Figure 2-2: Solidification path simulation of the designed CuCrNbZr alloys [48].

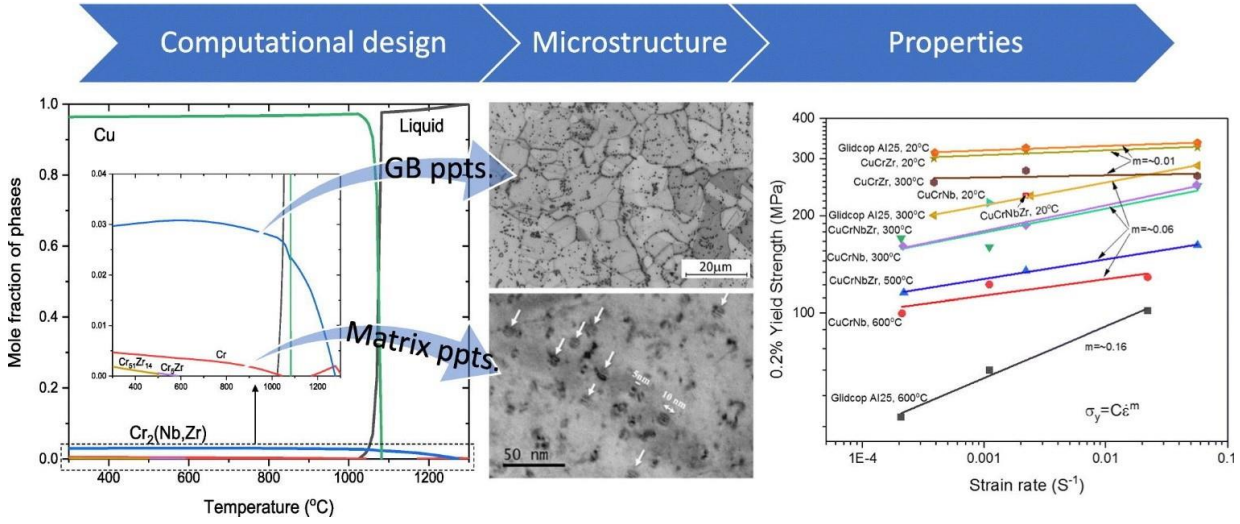


Figure 2-3: Calculated mole fraction of phases in the designed alloy as a function of temperature. The optical microscopy image shows coarse precipitates (Cr_2(Nb,Zr) Laves phase) at grain boundary and TEM image shows fine precipitates (Cr precipitates) in the matrix [48].

In the research work on second batch of newly made CuCrNbZr alloys (the 1st batch contains undesirable impurities which will be shown in Chapter 3 briefly), two Cu alloys were selected for detailed creep tests and microstructural characterization. The commercial 'Kabelmetal' CuCrZr alloy (Cu-0.78Cr-0.06Zr, wt.%) was used as a reference alloy, which had been solution annealed in flowing argon at 980 °C for 1 h then water quenched, followed by thermal aging at 475 °C for 2 h in flowing helium [50]. The designed composition of the new CuCrNbZr (Cu-2Cr-1.35Nb-0.18Zr, wt.%) alloy is listed in Table 2-3, together with the chemical analysis results from ingot that was fabricated at Oak Ridge National Laboratory. (Cu-1.77Cr-1.23Nb-0.18Zr, <0.2Sn, 0.3Fe, <0.6O and <1N, wt.%). The raw materials were Cu slugs (99.996 wt.%), Cr pieces (99.995 wt.%), Nb foil (99.97 wt.%) and Zr foil (99.94 wt.%) in metal basis. The dramatic difference in the melting temperature of Nb (2468 °C) and Cu (1083 °C) would cause excessive vaporization of Cu if the four elements were melted simultaneously. To minimize Cu vaporization, Cr (T_M=1907 °C) and Nb were pre-alloyed with a composition of Cr-18 at.%Nb, close to the eutectic composition of Cr and Laves_Cr_2Nb that melts at 1620 °C. The pre-alloy was crushed in small pieces in a steel mortar and then melted with Cu and Zr to form an ingot with the designed composition. The ingot was melted in an argon protected arc-melting furnace followed by drop-casting into the shape of 1.25×1.25×0.75 cm^3 bar, with an approximate mass of 100 g. The as-cast bar was then subjected to multiple-pass cold rolling at room temperature for a total 70% reduction in thickness. The multi-pass cold rolling process was done on a small Stanat rolling mill. For each cold rolling path, the mill was lowered by 0.254 mm followed by rolling the sample and then flipping the sample from the top to bottom plane in order to make it (the bottom plane) the top plane. For each rolling step the same rolling direction was maintained as marked on the original ingot. This was repeated for each pass through the mill two more times for a total of 3 rolling passes. The mill was then lowered 0.254 mm and the same process was repeated until the sample reached the desired thickness. This rolling step was intended to provide a high dislocation density to promote matrix precipitate nucleation and to promote recrystallization during subsequent heat treatment. Both dislocations and grain boundaries can serve as potential nucleation sites for large Cr_2Nb precipitates. The as-rolled materials were solution annealed at 970 °C for 20 min, followed by water quench. The solution anneal conditions were selected to allow the near-maximum amount of Cr to dissolve back into the Cu-rich matrix (for subsequent Cr precipitation strengthening via aging), while preventing sample melt or allowing excessive grain growth. The aging was

conducted at 475 °C for 3 h on the solutionized samples, followed by air cooling. Figure 2-4 represents the optical microstructure of the newly made CuCrNbZr alloy.

2.2 Ion irradiation

It is well established that ion irradiation can reproduce essentially all of the standard microstructural features observed in neutron-irradiated materials (dislocation loops, cavities, radiation-induced solute segregation, radiation-induced precipitation, etc.). In particular, ion irradiation can be conducted at a well-defined energy, dose rate, and temperature in a short time without material activation. These features along with the limited penetration depth of ions provides experimental control of microchemical and microstructural characterizations that is difficult or impossible to perform using neutron irradiation [51].

2.2.1 In situ ion irradiation

Coherent precipitates can act as traps that capture a defect but preserve its identity until it is annihilated by the opposite type defect. The degree of coherency of precipitates can strongly affect how precipitates perform as a defect sink. Also, the mechanical properties of materials depend on the coherency of particles. In situ irradiation experiments are a valuable approach to explore the threshold concentration of absorbed self-interstitial atoms needed to induce coherency loss as a function of precipitate size or initial degree of coherency. The detailed sample preparation methods for in situ irradiations will be provided in section 2.3.1.

In situ ion irradiation in thin foils were performed at the Intermediate-Voltage Electron Microscopy (IVEM)-Tandem facility in Argonne National Laborator (ANL) (see Figure 2-5 [52]) There the accelerator is coupled to a Hitachi-9000 TEM operated at 300 keV, impinging at a glancing 30^{o} into the electron-transparent specimen areas. The TEM thin foils were tilted in α direction to around -15^{o} from the incident electron beam, thus both ion irradiation and TEM observation can be simultaneously conducted without large deviation of the damage dose compared to the SRIM calculations. The ion beam is homogeneous over an area of 1.5 mm in diameter. The materials investigated were irradiated at room temperature, 340 ^{o}C and -223 ^{o}C with 1 MeV Kr^{++} ions. The irradiation temperatures were chosen in such way that the mobility of

vacancy defect clusters varies above three typical temperatures identified as defect recovery "stage I" (-223 ºC), "III" (-33 ºC) and "V" (150 ºC) for pure Cu. Damage dose and Kr implantation profiles were calculated with SRIM 2008 (stopping power version) code using quick Kinchin-Pease simulation mode and assuming a displacement threshold energy of 30 eV for pure copper, with ~0 eV binding energy [53] (Figure 2-6).

Irradiations were performed under three different conditions:

(1) Room temperature (RT) ion irradiation experiments were conducted as the first step to investigate the sink strength dependent coherency loss of the precipitates in all the heat-treated samples to the final fluences of $(0.5\sim4)\times10^{14}$ ions/cm^2 equal to 0.08~1 dpa, the corresponding fluxes were controlled at 6.25×10^{10} ions/cm^2·s (1×10^{-4} dpa/s). After the TEM observation on the last dose of the irradiation, the samples were post-irradiation annealed at 300 ºC for 10 min before TEM characterization on the precipitate contrast and defect clusters morphology, then the temperature was increased to 400 ºC, samples were annealed for another 10 min before TEM characterization. 500 ºC was the highest and last annealing temperature and samples were annealed for more than 40 min, allowing enough time for defects recombination before TEM characterizations.

(2) The second condition was a high-temperature (200 and 340 ºC) irradiation on CC1 and CC2 alloys to a fluence of 1×10^{14} ions/cm^2 (0.16 dpa), with the corresponding fluxes were controlled at 6.25×10^{10} ions/cm^2·s (1×10^{-4} dpa/s), for the purpose of investigating the effect of mobility difference of vacancy defect clusters on the coherency loss of the Co-precipitates with different sink strengths.

(3) The third condition was a low-temperature (-223 ºC) experiment on CC3 alloy to a final fluence of 0.25×10^{14} ions/cm^2 (0.04 dpa) to study the matrix impurity effect on mobility of defect clusters in a dilute Cu-base binary alloy. The irradiation dose rate was controlled at 6.25×10^{9} ions/cm^2·s (1×10^{-5} dpa/s) in order to record the coherency change of the Co-precipitates at a much slower speed. After the TEM observation on the last dose of the irradiation, the samples were post-irradiation annealed from -223 to -173, -123, -73, -23, 25, 300, and 400 and 500 ºC, similar to the post-irradiation annealing part in condition 1.

Details of the irradiation are listed in Table 2-4.

Table 2-3: Chemical composition and room temperature properties of CuCrZr compared with designed CuCrNbZr alloy.

Alloys	Cr (wt.%)	Nb (wt.%)	Zr (wt.%)	Cu (wt.%)	Hardness (VHN)/STD	Electrical Conductivity (%IACS)
CuCrZr	0.78	0	0.13	Balance	135.8/ 6.2	83.4
CuCrNbZr	1.77	1.23	0.18	Balance	137.9/ 7.0	72.1

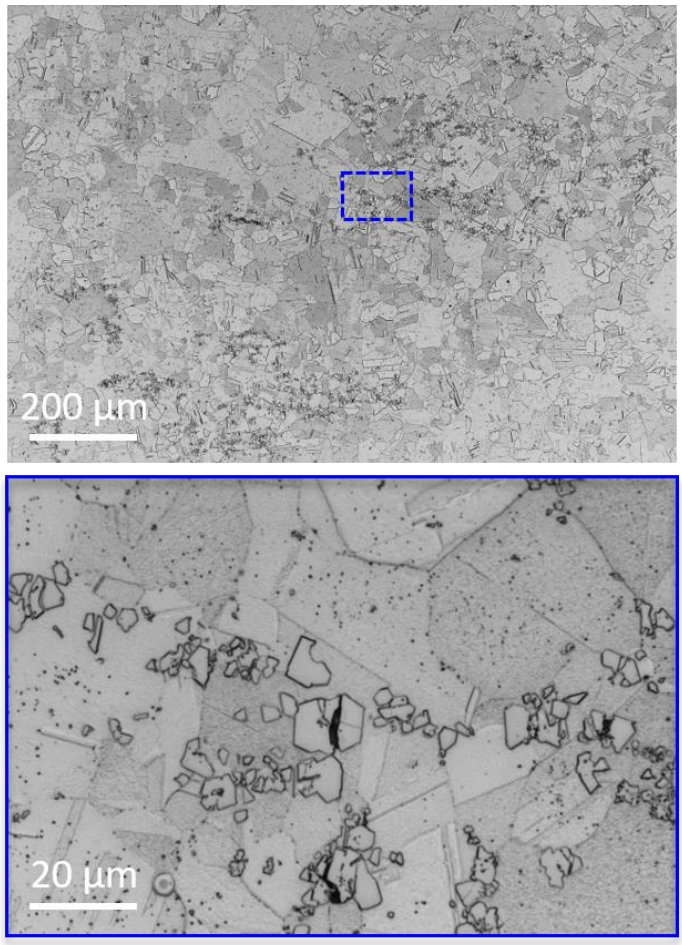


Figure 2-4: Typical optical images of newly fabricated CuCrNbZr alloys in low and high magnifications.



Figure 2-5: IVEM-Tandem facility at Argonne National Laboratory. The accelerator is coupled to a Hitachi-9000 NAR TEM operated at 300 keV, impinging at a glancing 30^{o} into the electron-transparent specimen areas [52].

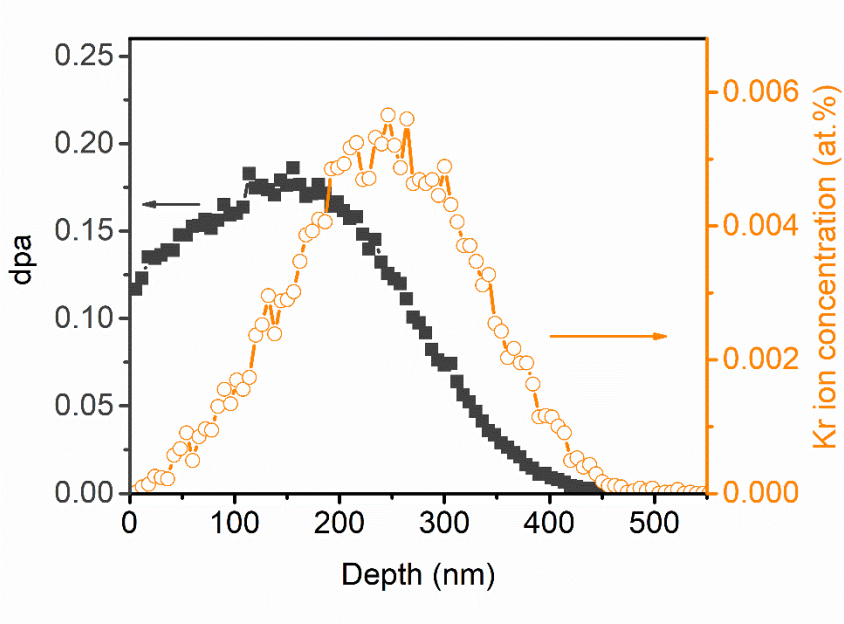


Figure 2-6: SRIM prediction profile of depth distribution of displacement damage and implanted ions for 1 MeV Kr^{++} ions irradiated to 1.0×10^{14} ions/cm^2.

Table 2-4: Summary of irradiation conditions of CC1, CC2, CC3, CC4, CFZ and CCZ alloys with concerns of irradiation temperature, damage dose and post-irradiation annealing.

Heat ID	Irradiation Temperature (°C)	Final damage dose (dpa)	Final post-irradiation annealed temperature (°C)
CC1	RT	0.25	500
	RT	1	500
	200	0.125	-
	340	0.0625	-
CC2	340	0.25	-
CC3	RT	0.25	500
	-223	0.0625	500
CC4	RT	0.0125	500
	RT	0.125	500
CFZ	RT	0.25	500
	RT	0.625	500
CCZ	RT	0.25	400

2.2.2 Ex situ ion irradiation

The length scale of the irradiation damage region for ion beams with MeV energies (~1 μm) is sufficiently large to extract microstructural information relevant for bulk irradiation conditions. By utilizing cross-section analysis techniques, the depth dependence of the damage rate and cumulative damage level can in principle be used to explore phase stability of precipitates in the ion irradiation damage region and defect migration behavior beyond the damage region within a single fluence specimen. In this work, ion beam irradiations can enable important experimental validation of fundamental radiation effects processes, such as confirmation of molecular dynamics simulation of glissile defect clusters that may exhibit one-dimensional migration [54, 55].

Before the ion irradiation, samples were prepared by conventional mechanical grinding up to #4000 grit SiC paper and using diamond paste up to 0.5 μm then final polishing using a Buehler's VibroMet polisher with a 50% colloidal silica and 50% distilled water suspension to achieve a mirror like surface. Polished samples were subsequently irradiated with 1 MeV Ni^+ ions to the fluences of 7×10^{13}, 7×10^{14} and 7×10^{15} ions/cm^2 at room temperature, 350 and -117 °C in UT-ORNL Ion Beam Materials Laboratory (IBML) located on the campus of the University of Tennessee, Knoxville (UTK). The corresponding fluxes were controlled at 1.4×10^{12}, 2.8×10^{12} and 2.8×10^{12} ions/cm^{2}s. This corresponds to a calculated mid-range damage level of 0.1, 1 and 10 dpa and a total damage range of 600 nm based on the SRIM 2013 code using quick Kinchin-Pease simulation mode and assuming a displacement threshold energy of 30 eV for pure copper, with ~0 eV binding energy [53]. The damage and implanted ion concentration profiles are shown in Figure 2-7 experimental details are listed in Table 2-5. A defocused beam was used to create a nearly homogeneous implantation fluence across the face of the sample [56]. Figure 2-8 shows the ion irradiation accelerator at UTK and the ion irradiation sample stage. The polished samples were attached to the sample holder by using high temperature resistant silver paste and the position of the beam irradiation area was monitored by luminescence. Thermocouple for monitoring the irradiation temperature was connected to the nearby location at the irradiated area, shown in Figure 2-8 (b), and the fluence was quantified by periodic measurement of the beam current using Faraday cups.

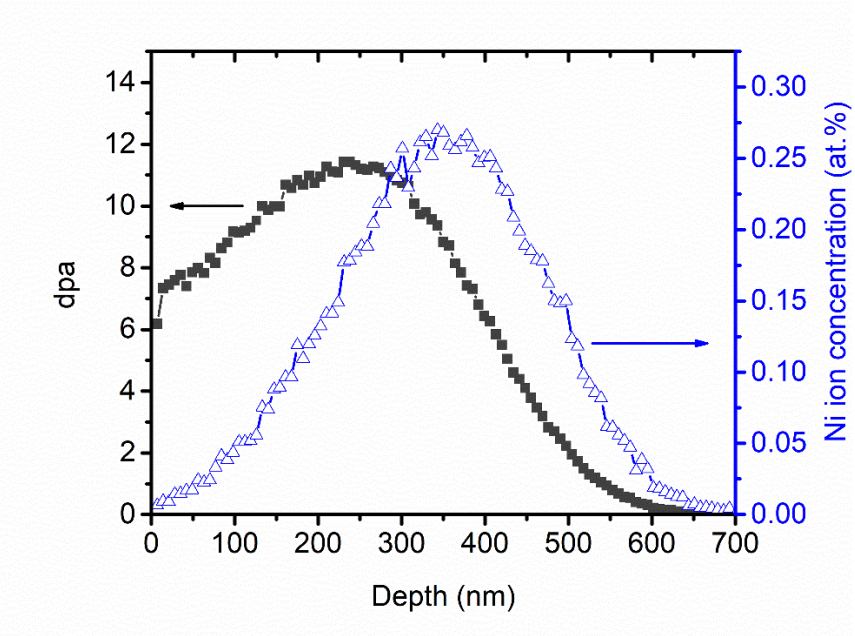


Figure 2-7: Depth profiles of displacement per damage (dpa) and induced Ni ion concentration predicted by SRIM code for dilute Cu alloys irradiated with 1 MeV Ni^+ ions to fluences of 7 × 10^{15} ions/cm^2.

Table 2-5: Summary of ex situ ion irradiation conditions of CC1, CC2, CFZ-0 alloys with concerns of irradiation temperature, damage dose, fluence and flux.

Materials	Ion species	Temp. (°C)	Dose (dpa)	Fluence (cm^{-2})	Flux ($cm^{-2}s^{-1}$)
CC1,		-177	0.1	7×10^{13}	1.4×10^{12}
CC2,	1 MeV Ni^+	25	1	7×10^{14}	2.8×10^{12}
CFZ-0		350	10	7×10^{15}	2.8×10^{12}

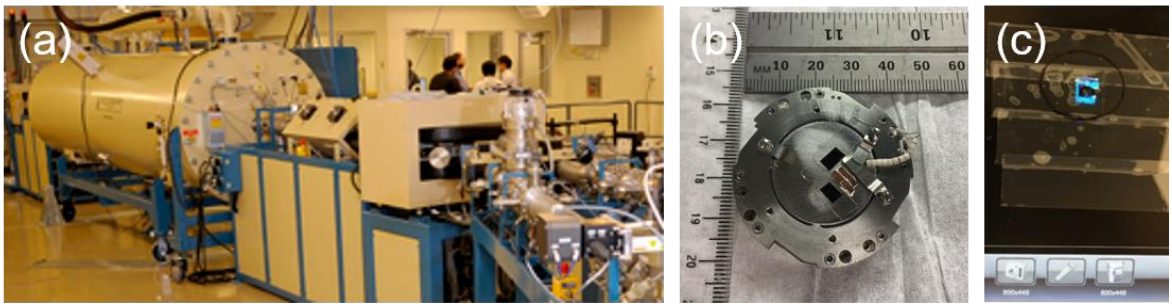


Figure 2-8: (a) Ion irradiation accelerator; (b) ion irradiation sample stage; (c) beam area judgement.

2.3 TEM

2.3.1 TEM specimen preparation

TEM thin foils for in situ ion irradiation experiments were first mechanically polished from a plate thickness of 0.5 mm to certain thickness (~100 μm) and punched into 3-mm diameter. The samples were further thinned to electron transparency by jet-polishing method at room temperature (20±1 ^{o}C) with an electrolyte of 250 mL phosphoric acid, 250 mL ethylene, glycol and 500 mL distilled water. Jet-polishing was performed using a Tenupol-5 facility with the applied voltage of 17 V. The jet-polished samples were rinsed in RT methanol for 4 times to remove un-wanted remaining chemicals from the specimen surface.

Although jet-polished TEM thin foils are ideal for TEM characterization because of their clean surface and uniform increment on the thickness from the hole edge, there are some conditions (small bulk sample available, μm-depth cross-section view for irradiated material) that do not meet the sample requirement for jet-polishing technique Thus, other TEM thin foil preparation methods were used. Cross-sectional TEM foils for ex situ irradiated materials and SS-3 tensile bars were prepared via focused ion beam (FIB) lift-out techniques with Ga^{+} ions at 30 kV and a finishing energy of 5 kV using an FEI Quanta 3D 200i Dual Beam workstation at Low Activation Materials Development and Analysis (LAMDA) and a Zeiss Crossbeam Auriga FIB-SEM system (Figure 2-9) at Joint Institute of Advanced Materials (JIAM). In order to reduce un-wanted FIB-induced damage and surface oxide layers, all samples were further thinned using Ar^{+} ions at 900 eV in a

Fischione Nanomill 1040 system with an incidence angle of ±10° for 3 min (Figure 2-9), and then cleaned in a Fischione 1020 Plasma Cleaner for another 3 min.

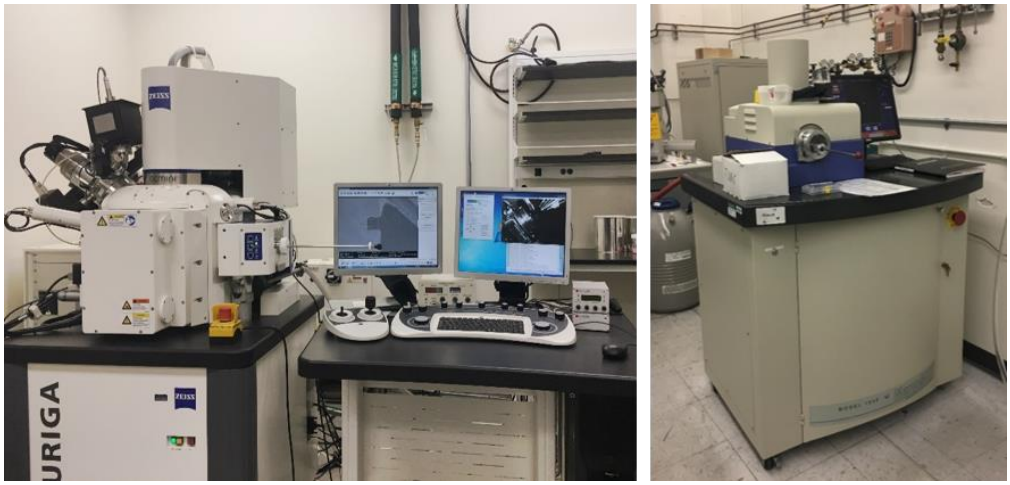


Figure 2-9: Zeiss Crossbeam Augria FIB/SEM instrument at JIAM (left); and Fischione Nanomill 1040 system at LAMDA (right).

2.3.2 Basics of TEM and imaging conditions

TEMs make use of two electron properties for magnifying features (e.g. nanoparticles, thin edges, defect clusters…) that are too small to see by optical techniques. A basic TEM consists of electron source, an assembly of magnetic lenses and the imaging device all arranged in a vertical column, with a high vacuum pressure of 5×10^{-7} torr or less. In the TEM, electrons are accelerated to the desired energy by applying a voltage. The potential energy of these electrons for metal or alloys characterizations are normally 200 and 300 keV; the corresponding relativistic wavelength are 0.00251 and 0.00197 nm. Details of the calculations can be referred to Williams's TEM book [57].

The TEM imaging conditions for coherent precipitates in dilute Cu alloys were mostly g=220 and 200 dynamical bright field (BF) and dark field (DF). Such bright-field conditions are

typical for a case of a spherically symmetrical strain field, that is a misfitting sphere in elastically isotropic material. In the BF images, coherent precipitates show black/black lobes with a line of no contrast that is always perpendicular to $\boldsymbol{g}$ (Figure 2-10). The coherency of small precipitates up to 50 nm diameter, e.g. Co-, Fe- and Cr-precipitates, in FCC structured copper matrix can be judged based on these imaging conditions, which will be shown in detail in Chapter 3.

Additionally, images for defects like stacking fault tetrahedra (SFTs) in FCC copper were taken using g=200 (g, 3g) DF and kinematical BF with beam direction close to [011]. High-resolution TEM images were conducted when the precipitates phase information was required.

In this research, conventional TEM examination was performed in a LAMDA facility JEOL 2100F TEM/STEM (scanning TEM) operated at 200 kV (Figure 2-11) to characterize the precipitate microstructures and the defects. A Hitachi-9000 TEM operated at 300 keV connected to IVEM-Tandem facility (Figure 2-5) was applied for the same purpose during in situ irradiation experiments.

2.3.3 Quantitative measurements of precipitates and defect clusters

To calculate the initial coherent precipitate sink strength and compare the radiation damage in various irradiation conditions, it is important to measure the size and number density of coherent precipitates and radiation induced defect clusters, e.g. dislocation lines, SFT, etc.

A common way of measuring the size of the coherent precipitates is averaging the lengths measured in two normal directions, one of which is parallel to the line of no contrast in dynamical two beam conditions [13]. To get the density of the precipitates or defect clusters, it is necessary to determine the thickness of the thin area where the density measurements were taken. Several techniques can be available, while in this research, thickness fringes and energy filtered TEM (EFTEM) methods were mainly applied.

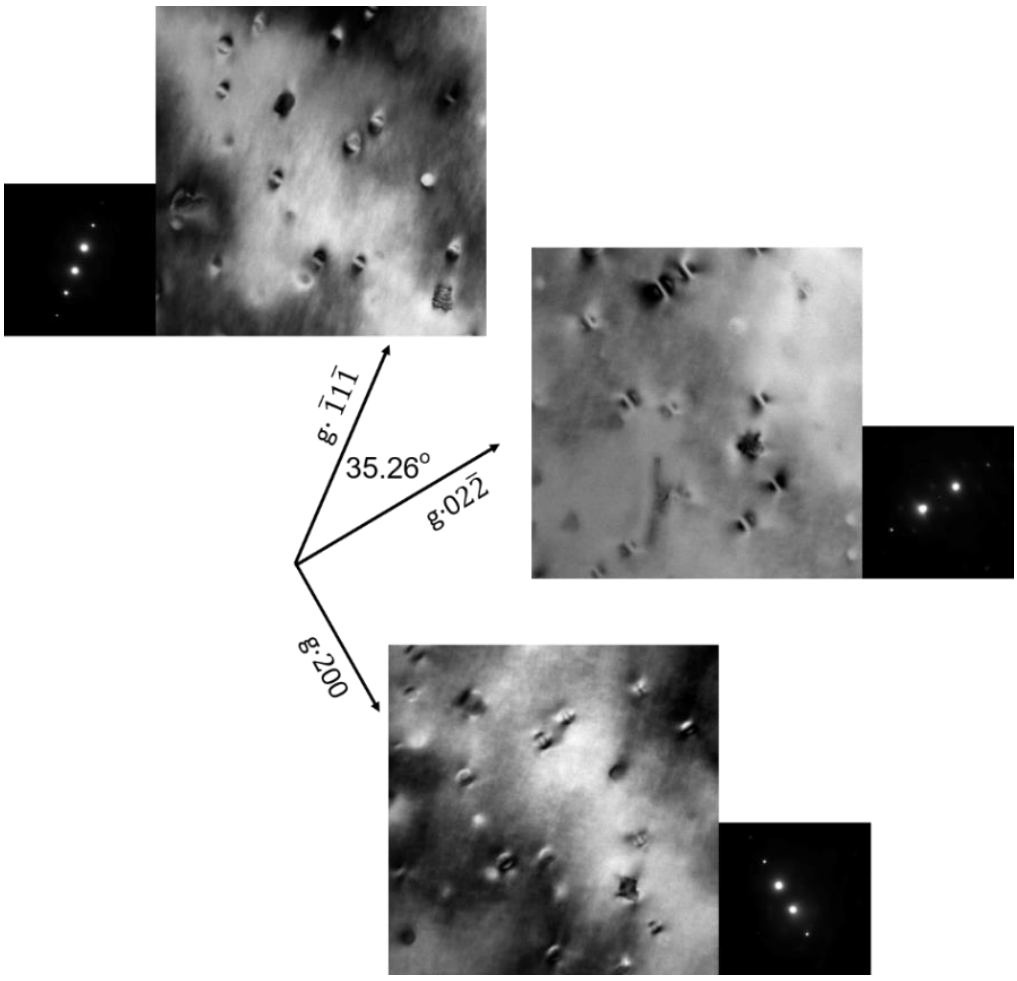


Figure 2-10: Coherent Fe-precipitates in a Cu-1%Fe alloy thermal aged at 600 ^{o}C for 15 h.



Figure 2-11: JEOL 2100F S/TEM instrument at LAMDA.

Thickness fringes are produced as the result of the intensity oscillation between the incident beam and the diffracted beam. When the TEM thin foil is tilted to dynamical two beam imaging condition, the thickness of the thin foil can be determined by counting the number of thickness fringes from the edge. Each fringe contains a pair of a white band and a black band in DF image. Figure 2-12 shows an example of thickness measurement through dynamical diffraction contrast images.

The thickness increment t can be calculated through:

$$t = \left(s_{eff}\right)^{-1} = \left(\sqrt{s^2 + \frac{1}{\xi_g^2}}\right)^{-1} \quad \text{(Eq. 2-1)}$$

$$s = \frac{1}{2}(n-1)|g|^2\lambda \quad \text{(Eq. 2-2)}$$

$$|g| = \frac{1}{d_{hkl}} \quad \text{(Eq. 2-3)}$$

where ξ_g is the extinction distance for diffraction $\boldsymbol{g}$. λ is the electron wavelength, n is the position where the Ewald sphere cut through the g-systematic row. The calculated t and relevant parameters for various diffraction conditions used in in situ irradiation experiments on dilute Cu alloys are shown in Table 2-6.

The thickness contour method was the primary method used to measure localized foil thickness in jet-polished TEM thin foils before ion irradiation. The uniform thickness increment from the hole edge would gradually disappear with defect accumulation in the sample and electron beam-sample interaction, which caused pronounced bend contours. Thus, it was difficult to precisely measure the defect density after irradiation.

Another thickness measurement for TEM thin foils applied in this research is energy filtered TEM (EFTEM). This method can be used on TEM thin foils prepared by jet-polishing and FIB techniques. Basically, in TEM mode, a relative thickness map can be achieved by acquiring unfiltered and zero-loss images from the same region under identical conditions (Figure 2-13).

The relative thickness is based on Poisson statistics of inelastic scattering:

$$\frac{t}{\lambda} = \ln\left(\frac{I_{unfilt}}{I_0}\right) \qquad \text{(Eq. 2-4)}$$

where I_{unfilt} is total electron intensity including intensities of elastically and inelastically scattered electron when no energy-selecting slit is inserted, I_0 is zero loss intensity, only the intensity from elastically scattered electron when specific slit width is selected, note that the wavelength would be different according to TEM voltage. The details of this technique can be found in [57].

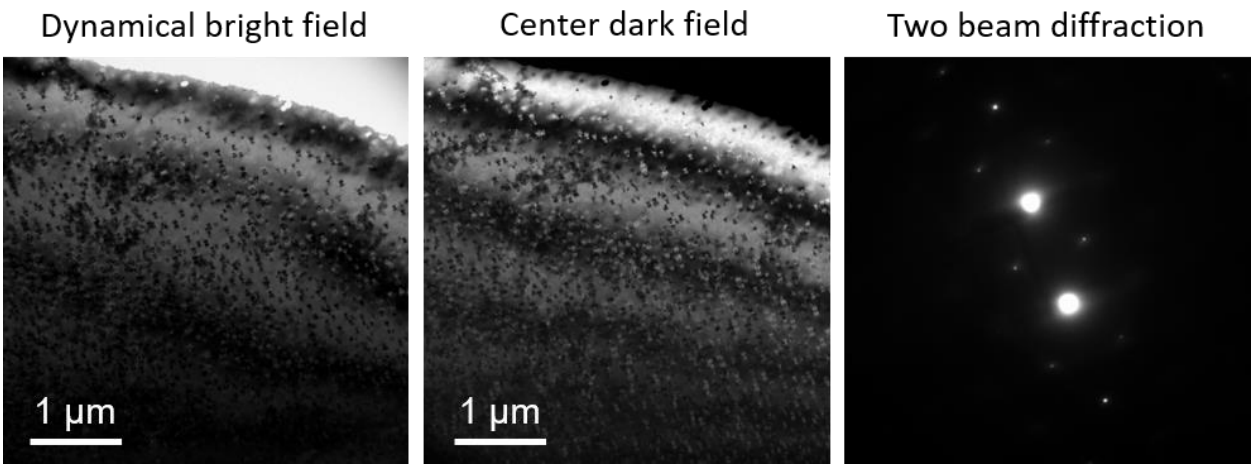


Figure 2-12: TEM images of CC2 alloy before RT irradiation. The imaging condition is g=220 dynamical for BF and DF.

Table 2-6: Parameters for calculating the thickness using thickness contour method [58].

Condition	g=220 dynamical two beam	g=220 (g, 3g)	g=200 dynamical two beam	g=200 (g, 3g)
Electron Voltage (kV)	300			
λ (nm)	0.00197			
d_{hkl} (nm)	0.1278	0.1278	0.1808	0.1808
n	1	3	1	3
ξ_g (nm)	41.6	41.6	28.1	28.1
s (nm^{-1})	0	0.121	0	0.060
t (nm)	41.6	8.1	28.1	14.3

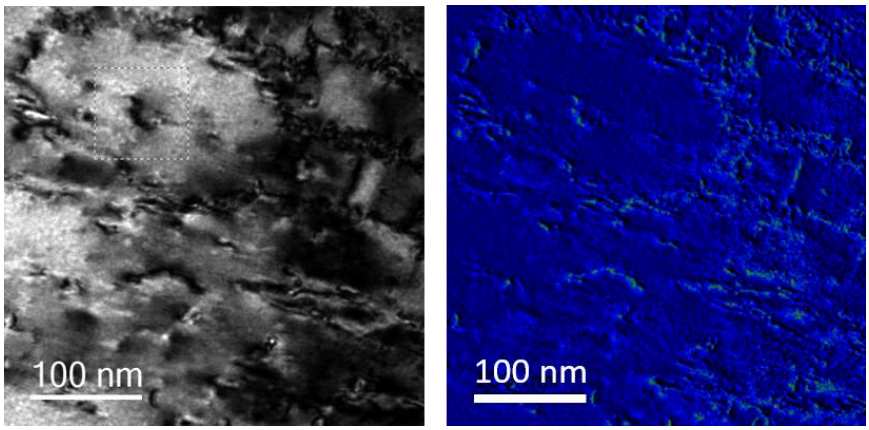


Figure 2-13: Unfiltered thickness map (left) and relative thickness map (right) of a FIB-prepared TEM thin foil from an un irradiated CC1 alloy.

2.3.4 In situ TEM

The IVEM-Tandem facility features the unique capability of high-quality conventional TEM during in situ ion irradiation at controlled sample temperatures. It is an investigatory technique that helps to understand the microstructural responses of materials to ion irradiation in real time including defect formation, mobilities, and interactions. TEM thin foils that are prepared through different techniques can be loaded into either a cryo-temperature double tilt holder or a double tilted holder that can be heated up to 1000 ^{o}C. In the heating holder, samples that were originally irradiated at RT to a certain damage dose can be post-irradiation annealed to higher temperatures after RT characterization. In the dilute Cu alloy in situ irradiation experiments, one of the difficulties is to characterize nano-precipitates during RT irradiation due to the high number density of less mobile vacancy defects and interstitial clusters compared to high temperature irradiation. In situ annealing experiments can solve this problem with controlled heating speed and annealing time at certain temperatures. However, the final heating temperature should not reach too high for Cu alloys. It was found that the surface near the hole edge region would diffuse more than thousand-nanometers, leaving behind regions of amorphous thin film. Figure 2-14 shows an overview TEM-BF image of a CC1 thin foil annealed at 500 ^{o}C. The TEM-DF image is an enlarged image showing the thickness from the amorphous edge to more uniform thickness contour regions changed significantly about 70 nm (imaging conditions was in kinematic DF condition with

g=200), the measured width of this amorphous region when the TEM thin foil was tilted was 56 nm in width.

2.3.5 Chemical composition analysis

X-ray energy dispersive spectroscopy (EDS) mappings of precipitates in dilute Cu alloys in Theme I were conducted in a FEI Talos F200X scanning/transmission electron (S/TEM), using a SuperX four-detector EDS system (Figure 2-15). A FEI Titan 80-300 probe aberration corrected microscope was applied in Theme II, this TEM operated at 200 kV is equipped with a X-FEG field emission electron source and four Bruker SuperX energy dispersive spectrum detectors. This configuration, also known as the ChemiSTEM method, allows to facilitate collection of characteristic X-ray signals at high counts per second and, furthermore, enables qualitative mapping of the elemental distribution.

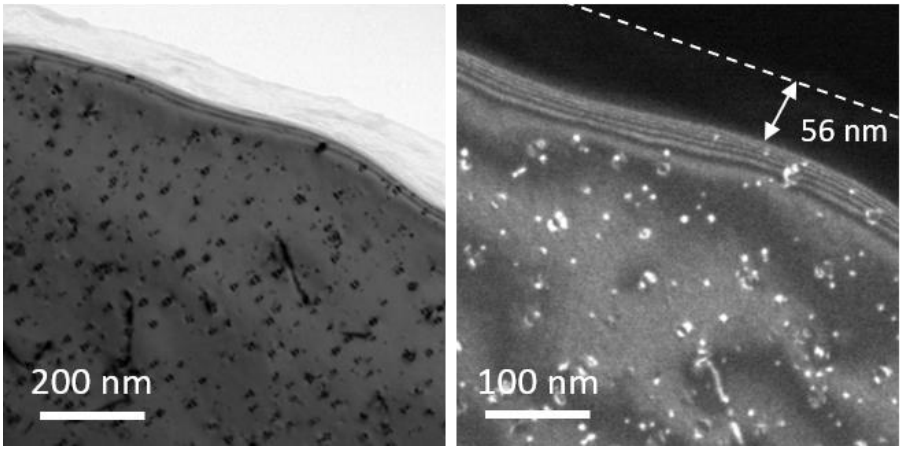


Figure 2-14: Kinematic TEM images of RT irradiated CC1 alloy post-irradiation annealed at 500 ^{o}C for 40 min.

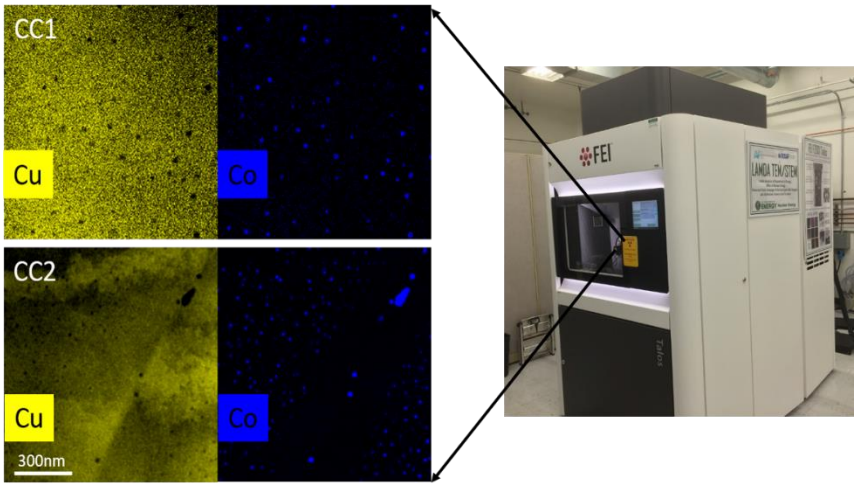


Figure 2-15: FEI Talos F200X S/TEM, along with a SuperX four-detector EDS system at LAMDA.

2.4 Electrical resistivity measurement

Four-wire electrical resistivity measurement (Figure 2-16) was performed on three SS-3 sheet tensile specimens (overall length of 16 mm and nominal gage dimensions of 7.62 × 1.52 × 0.76 mm^3, with the gauge length parallel to the rolling direction) of as received CuCrNbZr alloys near room temperature with a Keithley Model 182 Sensitive Digital Voltmeter. Current was applied to the outer electrodes in 10 mA increments from 10 to 100 mA with a Model 237 High Voltage Source Measure Unit. Individual specimen thickness and width in the tensile gage region were measured using a Mitutoyo digital micrometer to an accuracy of ±1 μm, and the room temperature were recorded at the beginning and end of the measurement period with a thermometer.

The correlation between resistance R, outer electrode current I, voltage V, electrical resistivity ρ, gauge length L and tensile bar cross-sectional area A follow the relationship below:

$$R = \frac{V}{I} \quad \text{(Eq. 2-5)}$$

$$\rho = \frac{RA}{L} \quad \text{(Eq. 2-6)}$$

Figure 2-16 shows an example of three electrical resistance values fitted from the V-I curves.

Control electrical resistivity measurements were performed on similar tensile specimens machined from a pure annealed copper plate (1.72×10^{-8} ohm·m resistivity, 101% International Annealed Copper Standard, IACS at 20 ^{o}C). The resistivity value at environment temperature was determined from the average of at least 3 electrical measurements for each alloy, then corrected to a standard reference temperature of 20 ^{o}C using the Cu matrix electrical resistivity temperature coefficient of 6.7×10^{-11} ohm·m/K. Following measurement of the electrical resistivity on the tensile samples, they were subjected to tensile testing at temperatures between 23 and 500 °C. The general test procedures for electrical resistivity testing on metals are summarized in ASTM B 193-87 (reapproved 1992), Standard Test Method for Resistivity of Electrical Conductor Materials.

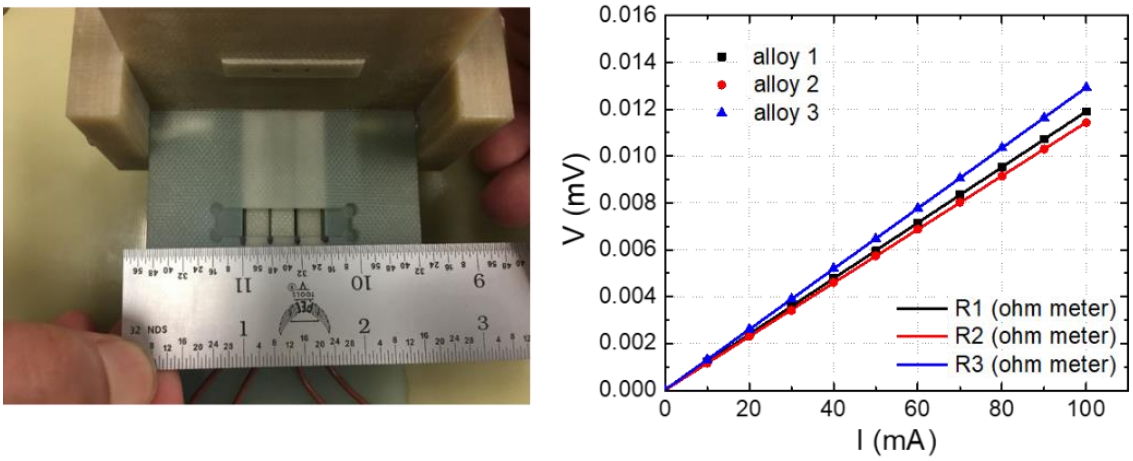


Figure 2-16: Four-wire electrical resistivity measurement for SS-3 tensile bar (left); linear fitting for resistance (right).

2.5 Mechanical tests

Room temperature Vickers hardness measurements were conducted using a LECOM-400-H2 hardness tester with a load of 1000 g and a holding time of 15 s. All the specimens were prepared to a mirror-finish following conventional metallographic sample grinding and polishing.

Hardness measurements were performed on five different locations on the specimen surfaces parallel to rolling directions. All tests used the type SS-3 miniature sheet tensile specimens that were machined from the cold-worked + solutionized + aged alloys, parallel to the rolling direction, the gauge section of which was of 7.62×1.52×0.76 mm^3.

Tensile tests were performed in air with a strain rate of 1×10^{-3} s^{-1}, at room temperature, 300 and 500 °C, respectively. Samples were shoulder loaded and deformation was restricted to the gauge section. Given the relatively high plasticity of the samples (10–20 % uniform elongation) and prior testing experience on similar subsized samples, the estimated strength uncertainty is ±10 MPa and the uncertainty in the tensile elongation is ± 2 %.

Creep testing on the CuCrZr and CuCrNbZr_HP alloys was conducted in accordance with the American Society for Testing and Materials (ASTM) standard E139-11, Standard Test Methods for Conducting Creep, Creep-Rupture, and Stress-Rupture Tests of Metallic Materials. All tests used the type SS-3 miniature sheet tensile specimens that were machined from the cold-worked + solutionized + aged alloys, parallel to the rolling direction, the gauge section of which was of 7.62×1.52×0.76 mm^3. The initial creep test was conducted at 500 °C and 90 MPa in air and significant oxidation was observed. The subsequent creep testing was conducted at 500 °C in inert gas environment under various applied stress levels, i.e., 90, 100, 110, 125 and 140 MPa.

2.6 Other Microstructure characterization

2.6.1 SEM

The Scanning Electron Microscope (SEM)- X-ray energy dispersive spectroscopy (EDS) line scan was performed in a Zeiss EVO SEM at 20 kV using an Oxford software to analyze the chemical composition of coarse precipitates in the matrix and at the grain boundaries.

2.6.2 XRD

X-Ray Diffraction (XRD) measurements were performed at Brookhaven National Laboratory's National Synchrotron Light Source-II (NSLS-II) using the high-energy X-rays available at the X-ray Powder Diffraction (XPD, 28-ID-2) beamline [59]. The wavelength of the

incident X-rays was 0.1875 Å (66.11 keV) with a beam size of 500×500 μm^2. Measurements were performed in transmission mode. The sample-to-detector distance and tilts of the detector relative to the beam were refined using a LaB_6 powder NIST standard. The raw two-dimensional patterns were background corrected by subtracting a dark current image. Noticeable artifact regions of the detector (beam stop, detector edge pixels, outlier pixels and dead pixels) were masked. The corrected and masked two-dimensional detector images were then radially integrated to obtain one-dimensional diffraction patterns. Phase identification was performed using MATCH. The corrected XRD patterns were Rietveld refined with the MAUD software package.

CHAPTER 3

EXPERIMENTAL RESULTS

The results obtained on the precipitate behavior of the thermally aged dilute Cu alloys (Theme I) are described in sections 3.1 (as fabricated characterization), 3.2 (in situ observation during thin foil ion irradiation) and section 3.3 (post-irradiation cross-section characterization after bulk ion irradiation), and the results on the precipitate characterization in as-fabricated and creep-tested CuCrNbZr alloys (Theme II) are described in section 3.4.

3.1 As fabricated characterization

The conventional precipitation treatment typically consists of homogenizing the alloy at high temperature, and a fast quenching process to room temperature to effectively retain the solute supersaturation from high temperature. In this work, Cu-Co and Cu-Fe alloys were all solution annealed at 1000 ^{o}C for 1 h and then were subjected to different thermal aging procedures. The Cu-1%Co alloys were subsequently aged isothermally at 600 ^{o}C for 12 h (CC1) and 625 ^{o}C for 12 h (CC2), 18 h (CC3) and 69 h (CC4) to form different size range of Co precipitates. The Cu-1%Fe with minor Zr element (CFZ) alloys were aged at 600 ^{o}C for 15 h to mainly produce Fe precipitates and low-density Cu_5Zr intermetallic compounds were precipitated out simultaneously, Cu-0.8%Cr with minor Zr element (CCZ) alloys were initially thermal aged at 475 ^{o}C for 2 h when received, nominal 3-nm diameter Cr precipitates were reported [50].

The uniformly distributed and nano-scale Co, Fe and Cr precipitates produced by heat treatment before irradiation are shown in Figure 3-1. The coherency of these precipitates can be judged from the electron microscope contrast when the so-called “no contrast line” appears in normal direction to the diffraction $\boldsymbol{g}$ vectors under dynamical diffraction conditions. The inset electron diffraction patterns indicate the dynamical bright field conditions when the images were taken. By measuring the two directions of the spherical precipitates and TEM image thickness, the precipitate mean size, density and point defect sink strength ($2\pi Nd$, where N and d are the precipitate density and diameter) can be calculated and they are listed in Table 3-1. It is noted that

the Co precipitate mean size in CC1 alloy (11.5±3.2 nm) is the lowest among all the Cu-Co alloys, while its precipitate density (1.7×10^{21} m^{-3}) is the highest, while precipitates in CC4 alloy seemed partially semi-coherent after the long-time thermal aging at 625 ^{o}C, based on the multi-no contrast lines visible in the image. The calculated sink strength of CC1 alloy (1.3×10^{14} m^{-2}) is approximately 2 times that of CC2 (5.3×10^{13} m^{-2}), 4 times CC3 (3.0×10^{13} m^{-2}), and 10 times CC4 (1.7×10^{13} m^{-2}) alloy. The Fe precipitate mean size (16.0±3.5 nm), density (7.3×10^{20} m^{-3}) and sink strength (7.3×10^{13} m^{-2}) in CFZ alloy are all between the levels of Co precipitates in CC1 and CC2 alloys. CCZ is a precipitation strengthened Cu alloy, one of the candidate structural materials for fusion energy applications. It achieves the lowest precipitate mean size (2.6±0.7 nm), highest precipitate density (7.0×10^{22} m^{-3}), and highest sink strength (1.1×10^{15} m^{-2}) among all the Cu-base alloys investigated in this research.

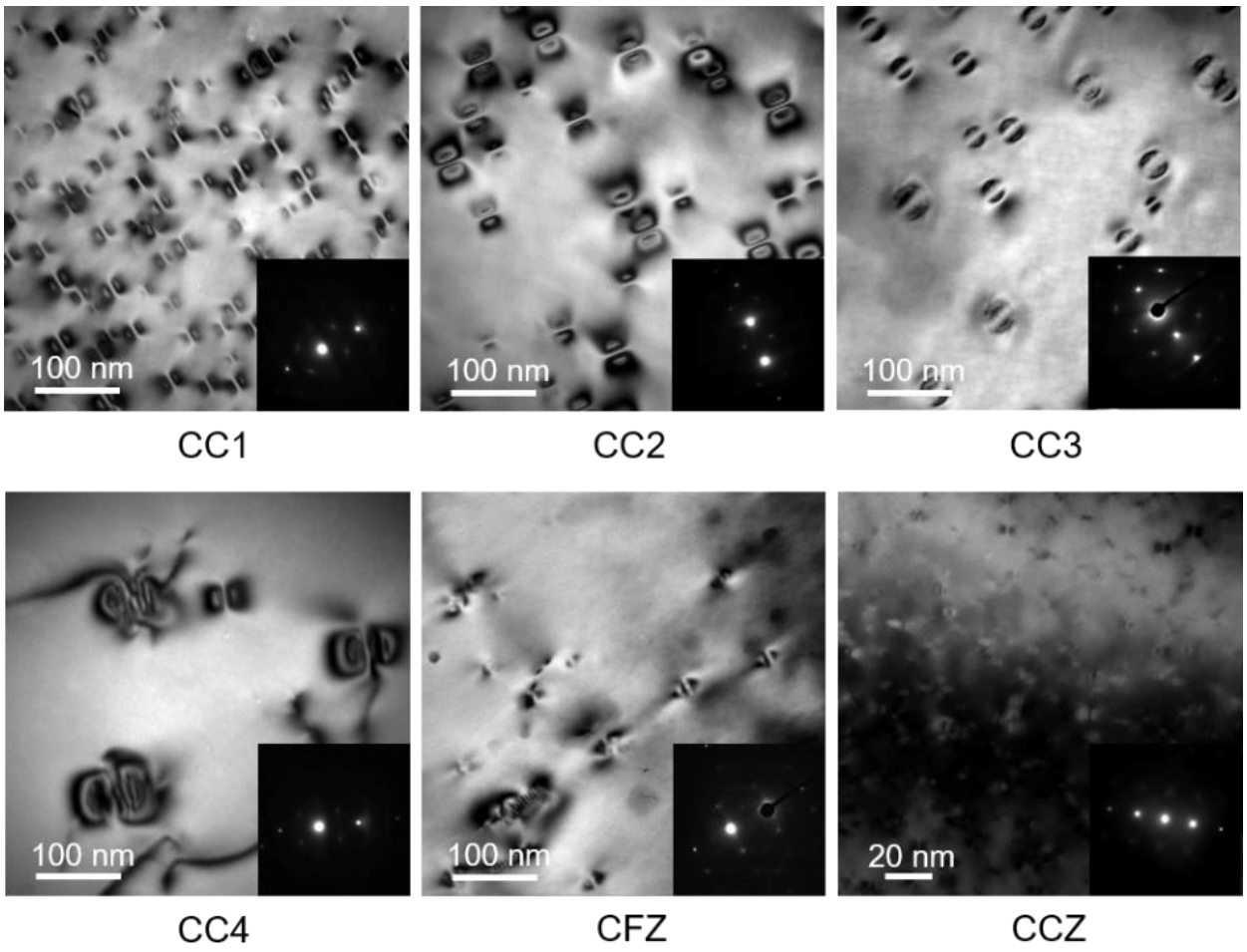


Figure 3-1: Typical microstructures of thermal-aging-produced coherent Co precipitates (CC1, CC2, CC3, CC4 alloys), Fe precipitates (CFZ alloy) and Cr precipitates (CCZ alloy). TEM images were taken in dynamical two-beam conditions as indicated in the inset electron diffraction patterns.

Table 3-1: Summary of initial precipitate mean size, density and sink strength corresponding to different thermal aging conditions in Cu-1%Co, Cu-1%Fe (minor Zr) and Cu-0.8%Cr (minor Zr) alloys.

Alloys (wt.%)	Heat ID	Precipitate Mean size (nm)	Precipitate Density (m^{-3})	Precipitate Sink strength (m^{-2})
Cu-1%Co	CC1	11.5±3.2	1.7×10^{21}	1.3×10^{14}
	CC2	19.6±3.6	4.3×10^{20}	5.3×10^{13}
	CC3	22.6±5.2	2.1×10^{20}	3.0×10^{13}
	CC4	41.2±8.3	6.7×10^{19}	1.7×10^{13}
Cu-1%Fe	CFZ	16.0±3.5	7.3×10^{20}	7.3×10^{13}
Cu-0.8%Cr	CCZ	2.6±0.7	7.0×10^{22}	1.1×10^{15}

3.2 In situ observation during thin foil ion irradiation

3.2.1 In situ observation of precipitate coherency loss during RT irradiation

Figure 3-2 shows typical microstructural evolution of initially coherent Co precipitates in CC3 alloy irradiated with 1 MeV Kr^{++} at RT to 0.125 dpa and then post-irradiation annealed at 300 ^{o}C for 10 min (the increasing temperature speed was about 60 ^{o}C/min), annealed at 400 ^{o}C for another 10 min, and finally annealed at 500 ^{o}C for 40 min. Here, all micrographs were taken under two-beam dynamical BF condition using a diffraction vector $\boldsymbol{g}$=220. In Figure 3-2 (a), Co precipitates became less visible with increasing damage dose due to the dense appearance of radiation induced defect clusters. Thus, it is impossible to judge the coherency loss of the precipitates irradiated to 0.125 dpa at RT because the high number density of the point defect or defect clusters contributed to the complicated TEM diffraction contrast. Figure 3-2 (b) presents that damage density decreased gradually when the TEM thin foil in the right side of Figure 3-2 (a) was post-irradiation annealed after RT irradiation to 300, 400 and 500 ^{o}C. The Co precipitates became more recognizable with increasing annealing temperature since vacancy clusters thermally dissolve to release vacancies (i.e. above recovery "stage V") that recombine with interstitial defect clusters, leaving less clusters in the matrix as dislocation loops or dislocation lines. After the RT

irradiation to 0.125 dpa, Co precipitates in CC3 alloy were judged to be incoherent due to lack of a singular "no contrast line" under dynamical BF contrast conditions (as evident in the right-hand image in Figure 3-2 (b)) after post-irradiation annealing at 500 ^{o}C.

Figure 3-3 shows the TEM images of Fe-precipitates in CFZ alloy irradiated with 1 MeV Kr^{++} ions at RT to 0.0025, 0.0125 and 0.625 dpa, then post-irradiation annealed sequentially to 300, 400 and 500 ^{o}C, the annealing procedure was basically the same as described in previous CC3 alloy condition. TEM imaging conditions were taken in kinematic bright field and weak beam dark field (WBDF) condition with g=200 (g, 3g) close to [011] zone axis in order to observe the evolution of vacancy defect clusters, especially SFT. The foil thickness at the center of the images taken at RT and 300 ^{o}C is roughly 43 nm, while thicker regions were focused for SFTs characterization at 400 ^{o}C and 500 ^{o}C because the original thin area near the hole edge was lost due to thermal diffusion.

Figure 3-4 shows the final precipitate microstructures in the five alloys initially irradiated at RT with damage doses of 0.0125~0.125 dpa then post-irradiation annealed to 300, 400 (CCZ annealed up to 400 ^{o}C only) and 500 ^{o}C. The results show that:

- With increasing damage dose (dpa), the microstructures of the precipitates were still coherent with the matrix up to 0.0125 dpa for CC1, CC2, CC3, CC4 and CFZ alloys, while for CCZ alloys, the Cr precipitates showed weak lobe-lobe contrast during RT irradiation, more oxide features showed up, indicating the instability nature of Cr precipitates after irradiation.
- There were no clear images to show if (or at what dose) the precipitates lost coherency up to 0.25 dpa at RT due to the high number density of defect clusters that obscured the visibility of the precipitates. Thus, it is difficult to judge whether or not the precipitates lose coherency during RT irradiation from the as-irradiated specimens.
- The post-irradiation annealed microstructures of the precipitates in RT irradiated CC1, CC2 (340 ^{o}C), CC3, CC4, CFZ, CCZ alloys are shown in Figure 3-4. The CC1 and CFZ alloys showed clear coherent precipitates in the matrix, while precipitates in the other four alloys differ. Initial coherent Co precipitates with sink strength $>10^{14}$ m^{-2} were more radiation resistant to loss of coherency than those with 10^{13} m^{-2}, while Fe precipitates may have lower coherency loss threshold dose compared to Co precipitates.

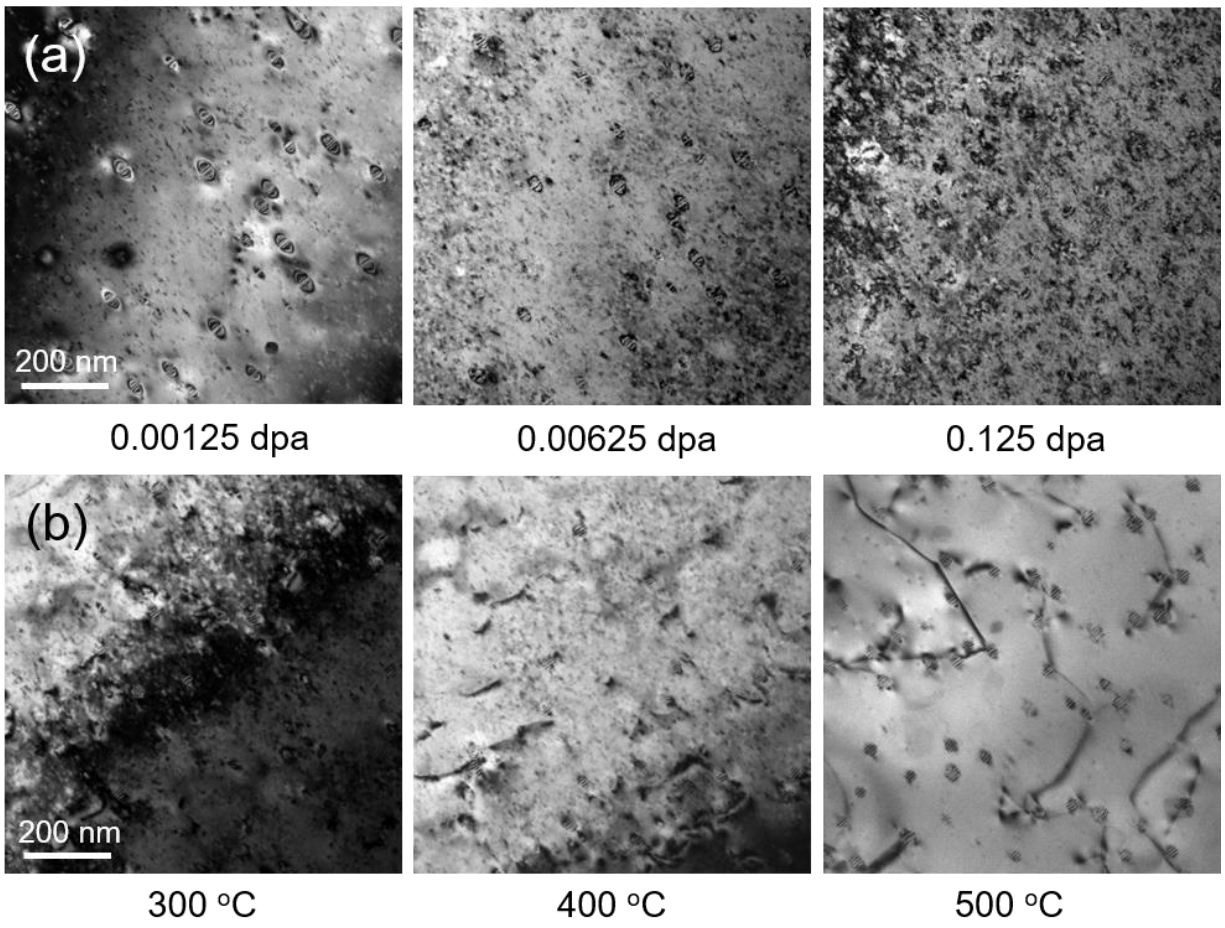


Figure 3-2: (a) CC3 thin foil irradiated with 1 MeV Kr^{++} ions at RT to 0.00125, 0.00625, 0.125 dpa; (b) irradiated CC3 thin foil post-irradiation annealed from RT to 300 °C and stayed for 10 min then annealed to 400 °C for 10 min, 500 °C for 40 min. The imaging condition is **g**=220 dynamical BF.

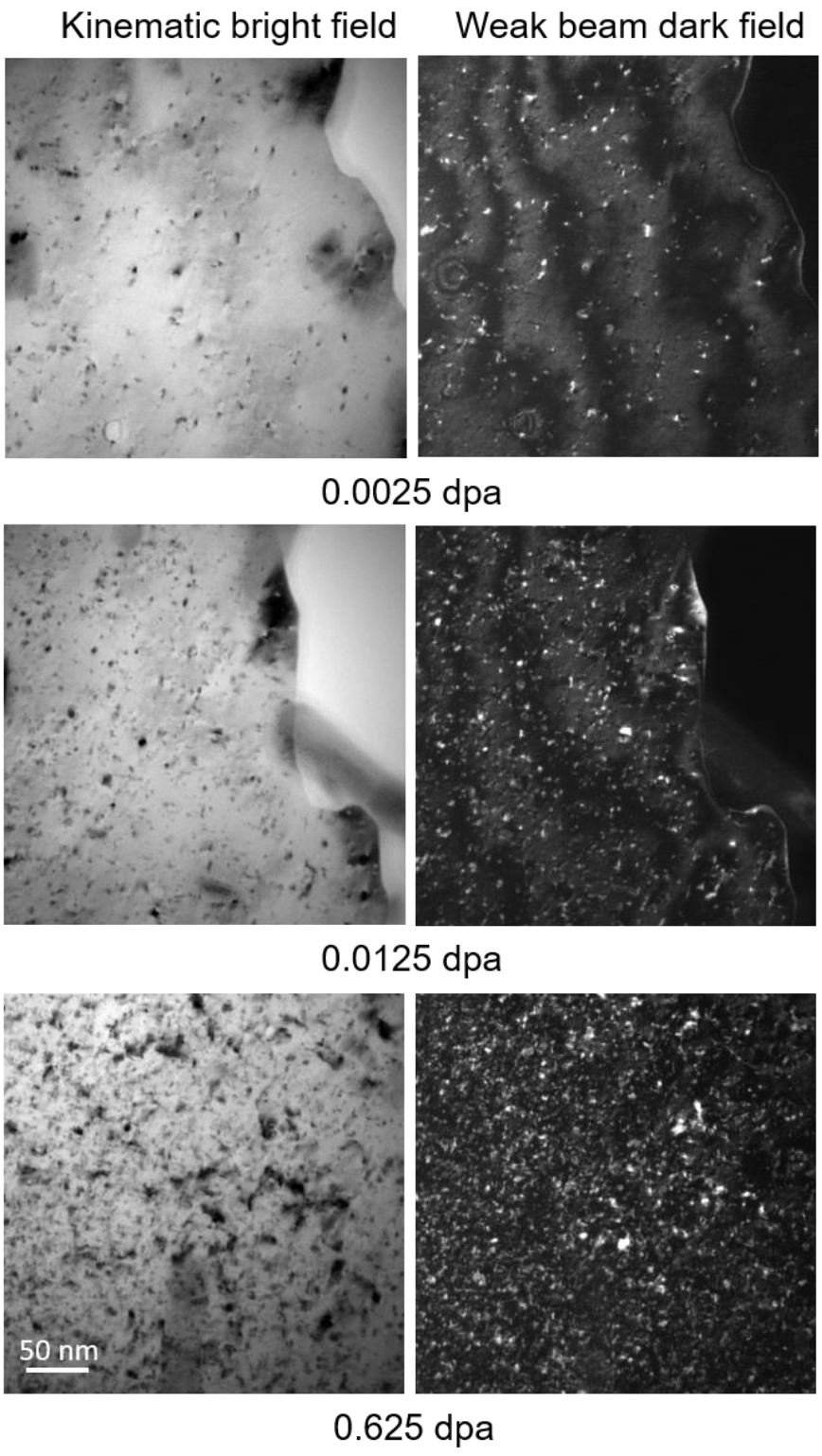


Figure 3-3: CFZ thin foil irradiated with 1 MeV Kr^{++} ions at RT to 0.0025, 0.0125 and 0.625 dpa, then annealed to 300 ºC and held for 10 min then annealed at 400 ºC for 10 min, and 500 ºC for 40 min. Imaging condition is g=200 (g, 3g) kinematic for BF and WBDF.

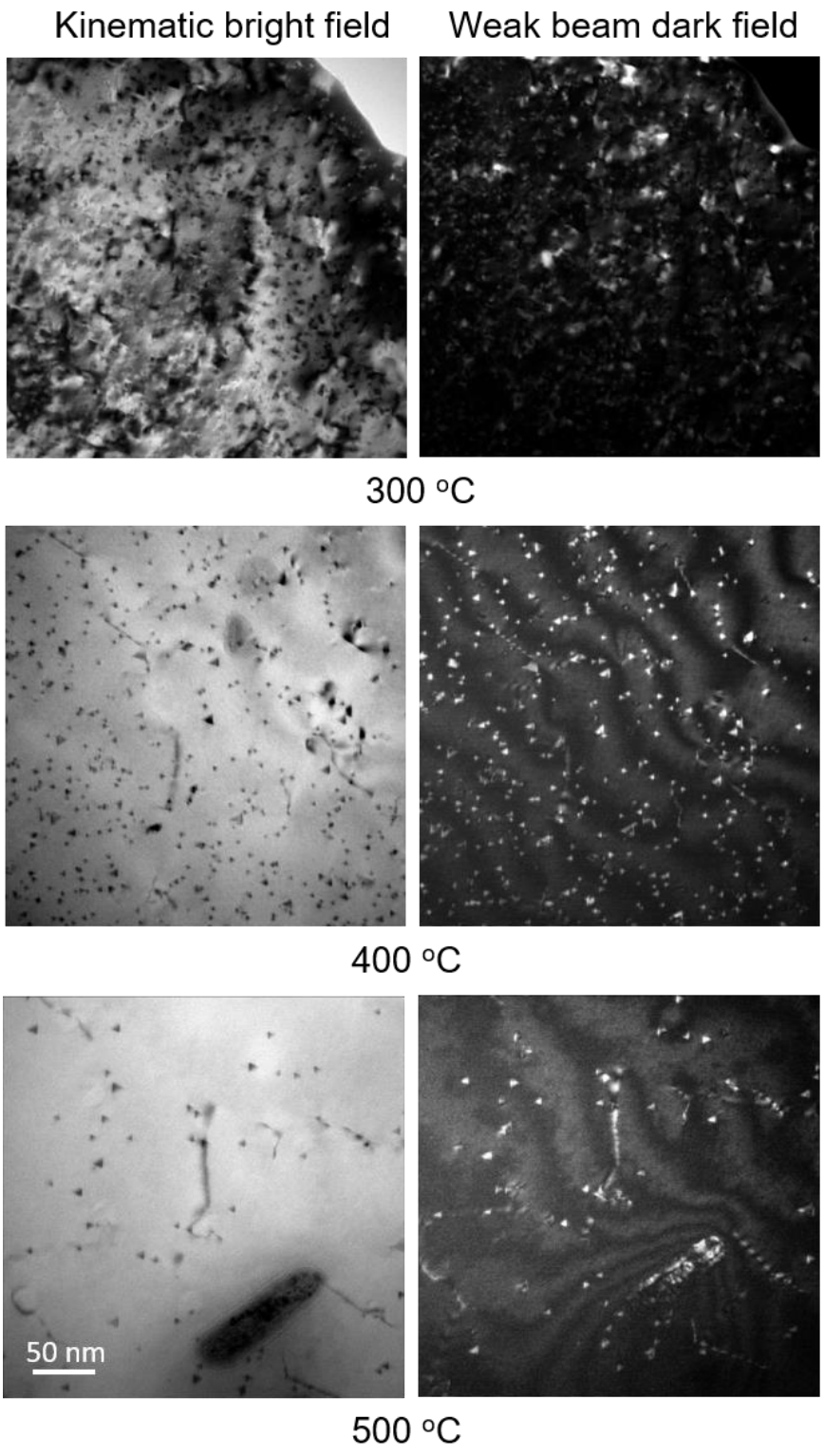


Figure 3-3: Continued. CFZ thin foil irradiated with 1 MeV Kr^{++} ions at RT to 0.625 dpa, then annealed at 300 °C for 10 min, 400 °C for 10 min, and 500 °C for 40 min. Imaging condition is g=200 (g, 3g) kinematic for BF and WBDF.

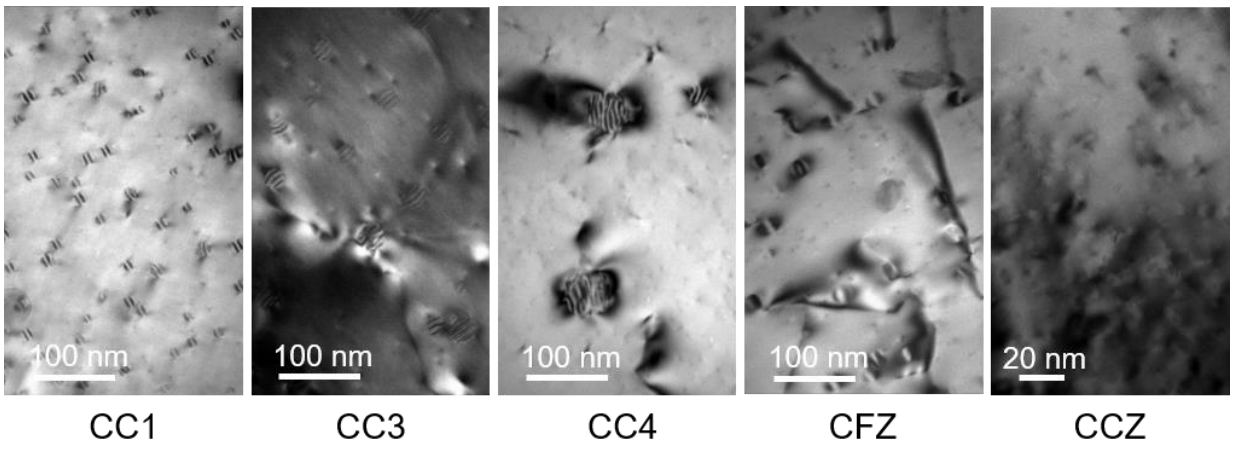


Figure 3-4: Microstructures of initial coherent precipitates after RT irradiation to 1.25 dpa, 0.25 dpa, 0.0125 dpa, 0.25 dpa and 0.25 dpa and post-irradiation annealing at 500 ^{o}C (400 ^{o}C for CCZ alloy) in CC1, CC2, CC3, CC4, CFZ and CCZ alloys. Images were taken in strong two-beam conditions.

3.2.2 In situ observation of precipitate evolution during high temperature irradiation

In RT irradiations, the high sink strength from thermally stable SFTs and dislocations in irradiated regions would result in fewer surviving interstitial defects to interact with coherent precipitates. Thus, irradiation temperatures of 200 ^{o}C and 340 ^{o}C were selected for further study because both of these temperatures are well above recovery "stage III" temperature for pure Cu (approaching "recovery V"), and therefore the effect from SFT sink strength is expected to be less than the RT irradiation condition. Conversely, the TEM thin foil hole edge diffusion effect is also expected based on results at different post-irradiation annealing temperatures after RT irradiation.

Two alloys (CC1 and CC2 alloy) were irradiated with 1 MeV Kr^{++} ions at high temperatures (200 and 340 ^{o}C) up to 0.125 and 1.25 dpa at a damage dose rate of 10^{-4} dpa/s. The major difference between the high temperature irradiation experiments is the Co precipitate sink strength in the two alloys.

Figure 3-5 shows diffraction patterns of a CC1 alloy first annealed to 200 ^{o}C before irradiation. Figure 3-6 shows low magnification images for thickness measurement. The imaging conditions in dynamic BF and DF were g=200 (g, 3g) for kinematic BF and WBDF images, with

both of the diffraction conditions close to the [011] zone axis. Figure 3-7 presents high magnification TEM images from near hole edge regions in Figure 3-6, showing coherent precipitates in different diffraction contrast conditions. Both dynamic BF and CDF images give strong lobe contrasts while in kinematic diffraction conditions, weaker strain fields around precipitates are presented.

Figure 3-8 shows dynamic BF and WBDF TEM images of CC1 alloy irradiated with 1 MeV Kr^{++} ions at 200 ^{o}C to 0.0025, 0.0125, 0.0625 and 0.125 dpa. The number density of vacancy defects increased with increasing damage dose, and the lobe contrast of initial coherent Co precipitates gradually faded. Figure 3-9 compares the vacancy defect cluster microstructure in irradiated CC1 alloy at 0.0025 and 0.125 dpa in the near hole edge region magnified from Figure 3-8. No significant difference on defect distribution between these two doses were observed except for the defect density, thus, vacancy defects distribution is not related to precipitate locations. The foil thickness at the center of the image is roughly 57 nm. Details of defect cluster densities will be analyzed in Chapter 4.

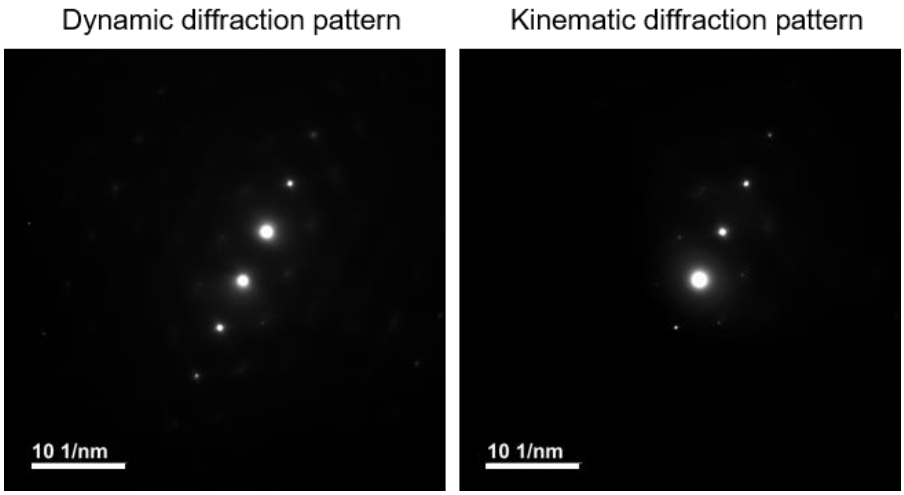


Figure 3-5: Diffraction patterns of CC1 alloy annealed to 200 ^{o}C before irradiation. The imaging conditions are **g**=200 for dynamic BF and CDF, **g**=200 (g, 3g) for kinematic BF and WBDF.

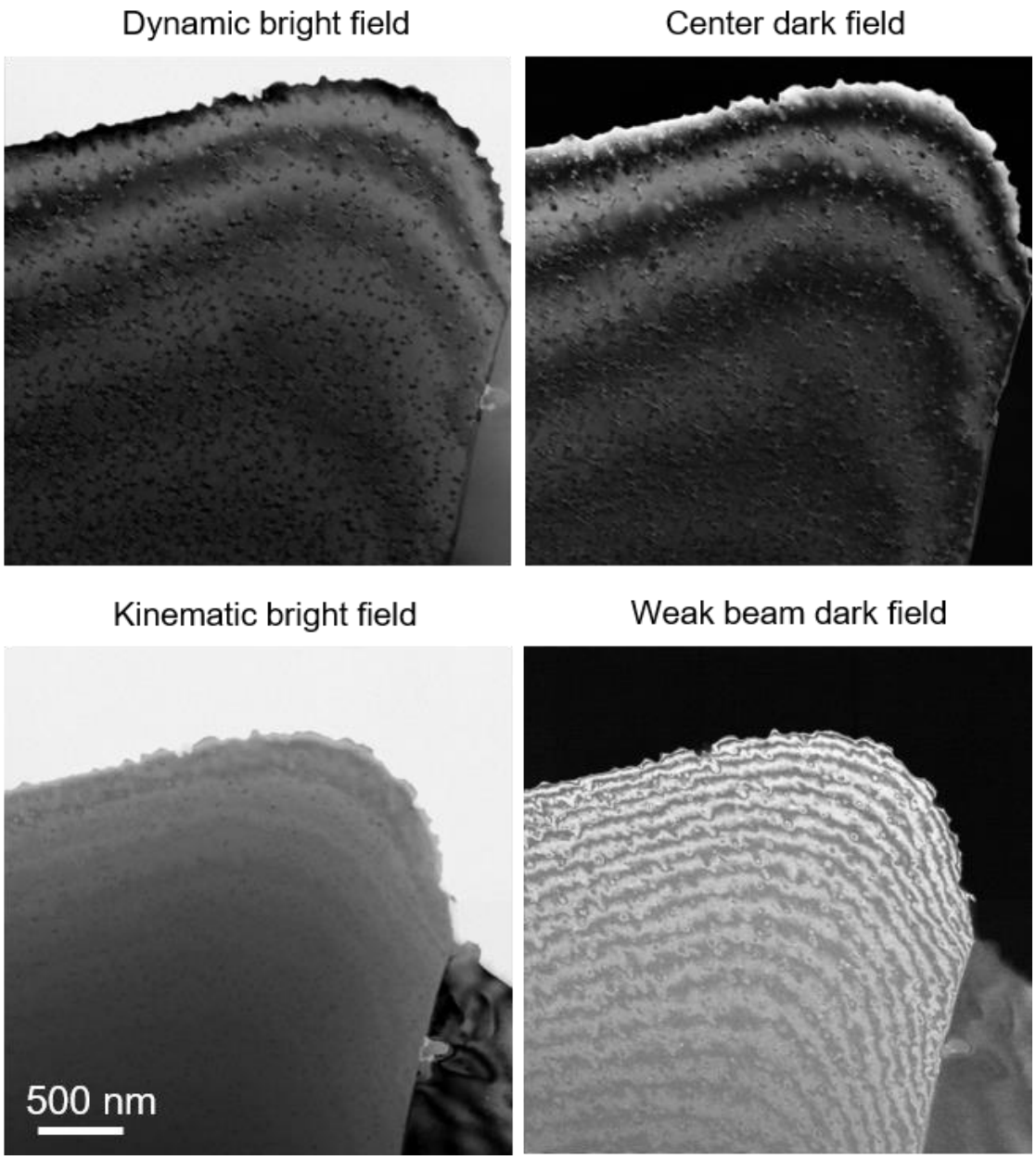


Figure 3-6: Low magnification TEM images of un-irradiated CC1 alloy at 200 ^{o}C. The imaging condition is g=002 for bright field and (g, 3g) for weak beam dark field with beam direction close to [110].

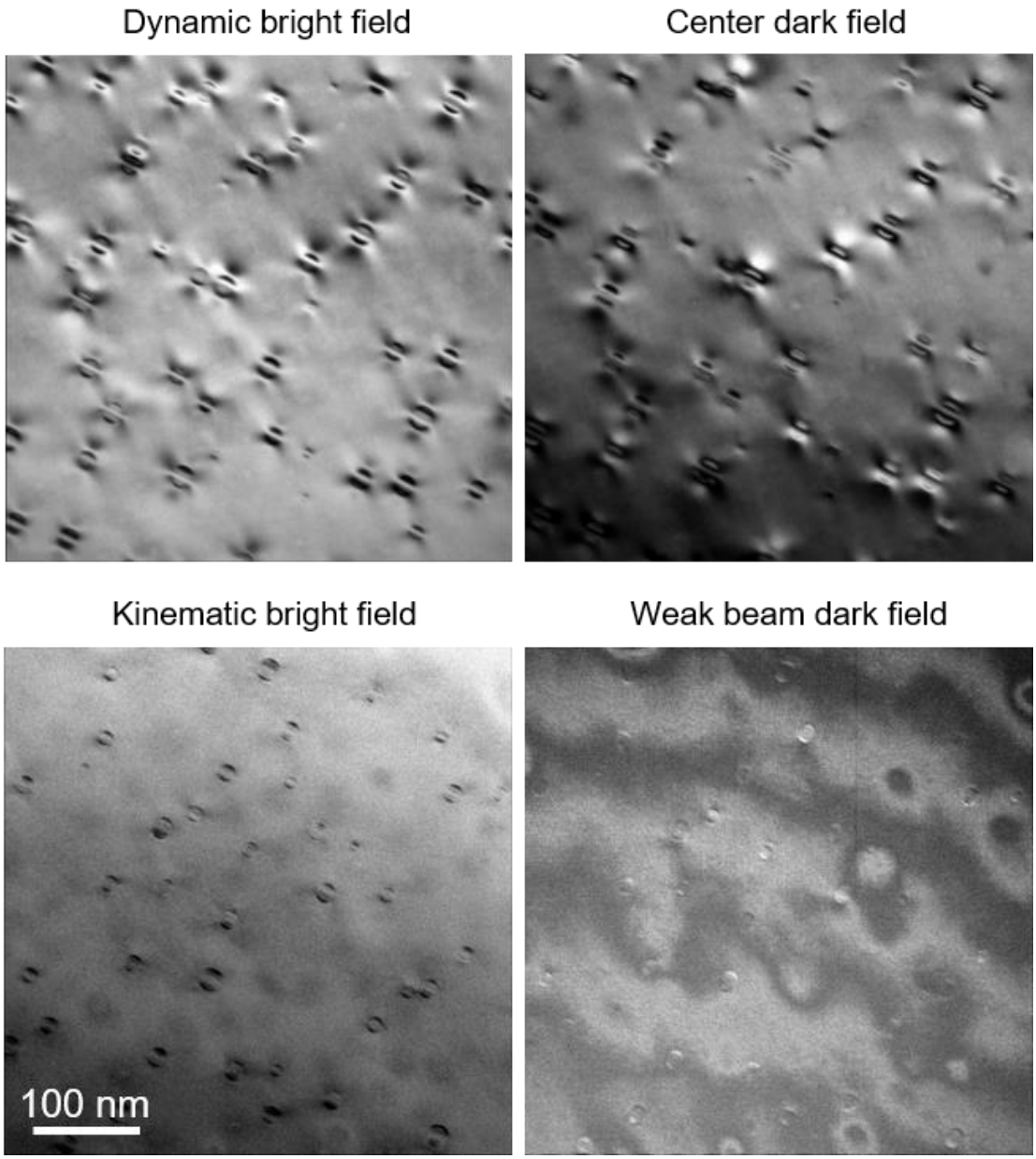


Figure 3-7: High magnification TEM images from the center area of Figure 3-6. The imaging condition is g=002 for bright field and (g, 3g) for weak beam dark field with beam direction close to [110].

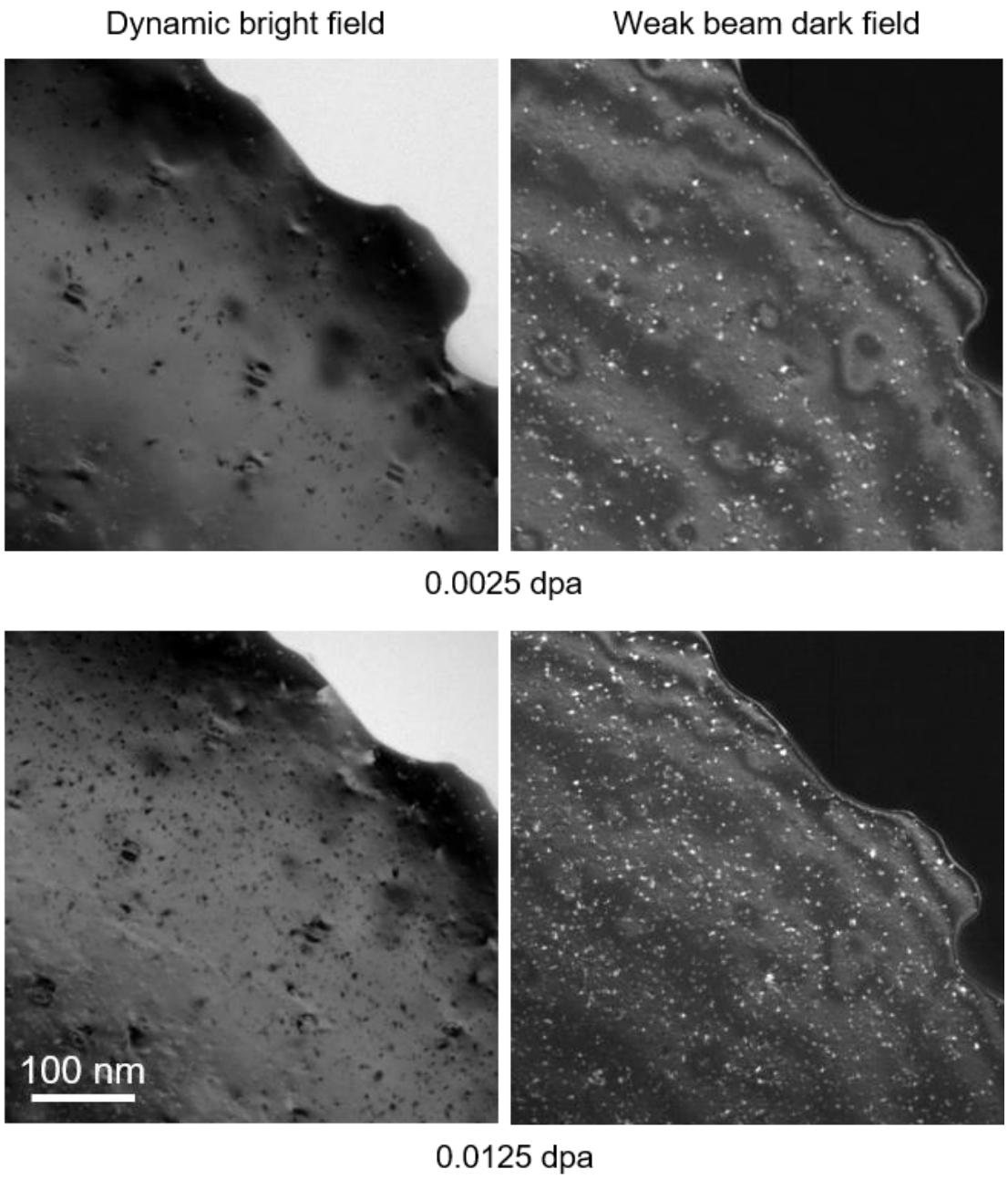


Figure 3-8: TEM images of CC1 alloy irradiated at 200 ^{o}C to 0.0025, 0.0125, 0.0625 and 0.125 dpa. The imaging condition is g=002 for bright field and (g, 3g) for weak beam dark field with beam direction close to [110].

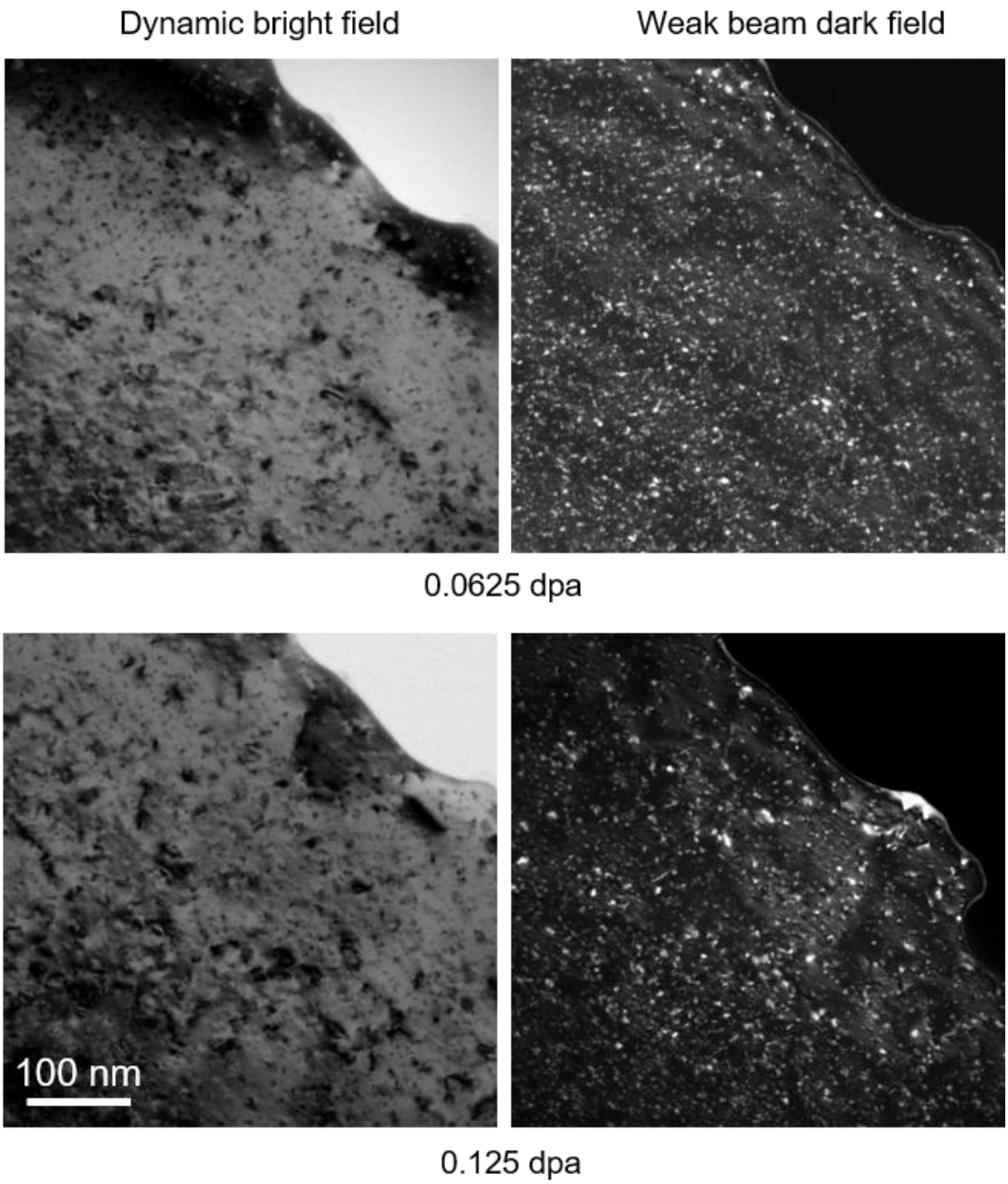


Figure 3-8: Continued. TEM images of CC1 alloy irradiated at 200 ºC to 0.0025, 0.0125, 0.0625 and 0.125 dpa. The imaging condition is g=002 for bright field and (g, 3g) for weak beam dark field with beam direction close to [110].

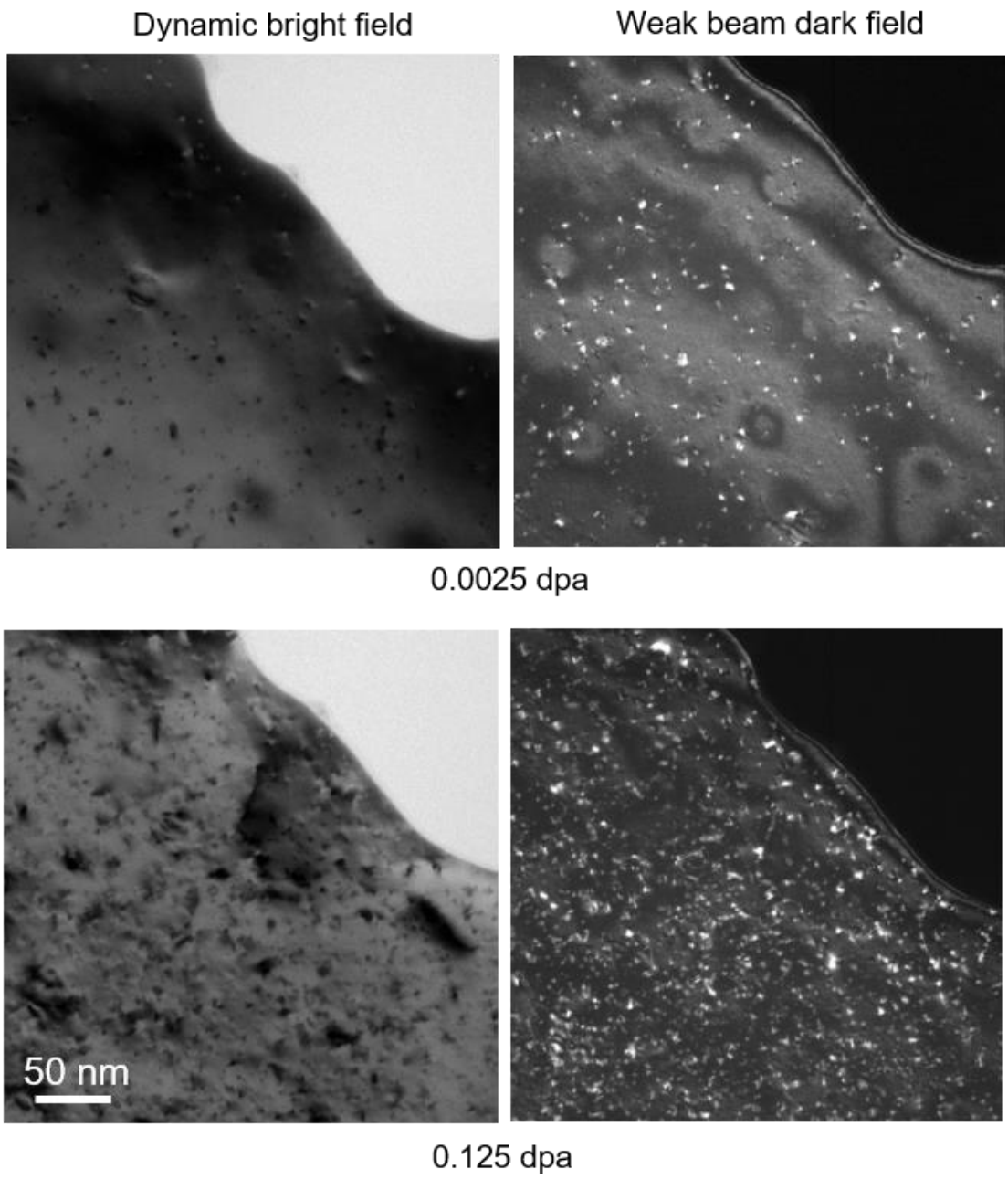


Figure 3-9: High magnification TEM images of CC1 alloy irradiated at 200 ºC to 0.0025 and 0.125 dpa. The imaging condition is g=002 (g, 3g) for weak beam dark field with beam direction close to [110].

3.2.3 In situ observation of precipitates evolution during cryogenic temperature irradiation

A CC3 alloy was irradiated at -223 ^{o}C where all vacancy defects in pure Cu are expected to be immobile and single interstitial atoms are only slight mobile. Therefore, interstitials can be absorbed by precipitates or form interstitial clusters. The TEM thin foil was irradiated up to 0.0625 dpa with the dose rate of 10^{-4} dpa/s; the recording speed is 1 frame/s. The first 9 s frames are shown in Figure 3-10. Precipitates strain field contrast kept changing with increasing irradiation damage dose. This thin foil was first post-irradiation annealed from -223 ^{o}C to RT, with increasing step of 50 ^{o}C, then sample was loaded to a high temperature TEM holder, and sequentially annealed to 300, 400 (Figure 3-11) and 500 ^{o}C (Figure 3-12). The observed defect cluster density decreased and size of the defect clusters increased with increasing annealing temperature.

3.2.4 In situ irradiation summary of coherent precipitate stability

Figure 3-13 summarizes the conditions applied for the in situ irradiation experiments with 1 MeV Kr^{++} ions at various temperatures on CC1, CC2, CC3, CC4, CFZ and CCZ alloys. The dose rates are all controlled at 10^{-4} dpa/s to make sure only damage dose and irradiation temperature are the variant parameters for any specific alloy. The high sink strength precipitates (~1×10^{14} m^{-2} for dilute Cu-Co alloys and ~7×10^{13} m^{-2} for dilute Cu-Fe alloys) show stronger suppressed loss of coherency, as precipitates remain coherent when the precipitate sink strength and irradiation damage dose are within the yellow shaded region. This may be due to nearly equal numbers of interstitials and vacancy defects arriving at the precipitate interface (effectively canceling each other out before loss of coherency from net absorption of a sufficient number of interstitial defects can occur). At low sink strengths, there might be a preferential medium-range strain-induced bias (in favor of) for absorption of interstitial defects at the precipitates that accelerates precipitate coherency loss. Cr precipitates seemed to be relatively susceptible to loss of coherency, suggesting that their small size and/or a structural instability between its FCC structure and BCC structure might be responsible.

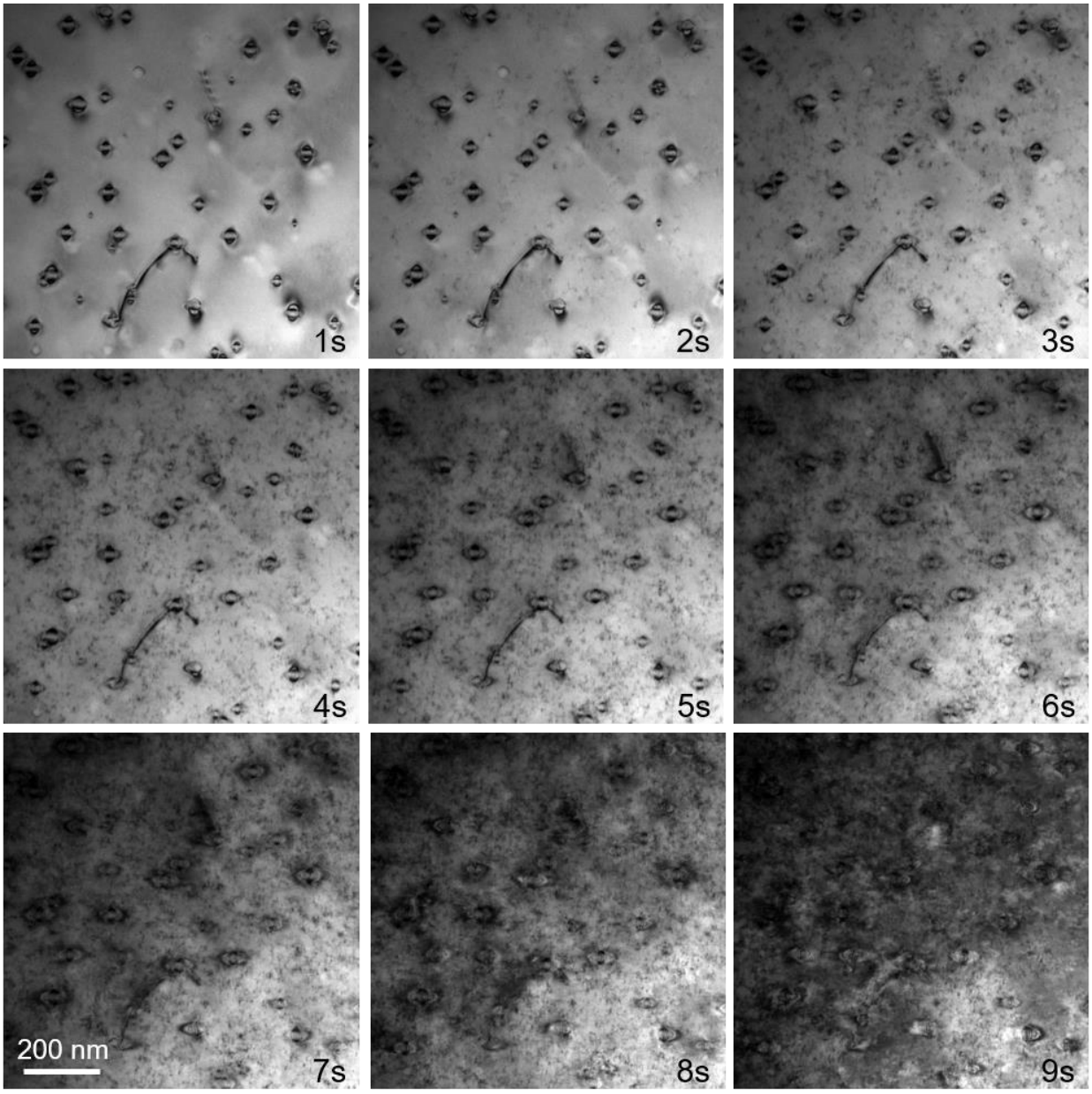


Figure 3-10: TEM images of CC3 alloy irradiated at -223 ^{o}C with 1 MeV Kr^{++} ions, the dose rate was controlled at 10^{-4} dpa/s, the first 9 s recorded the precipitate strain field change. The imaging condition is g=022 for bright field with beam direction close to [100].

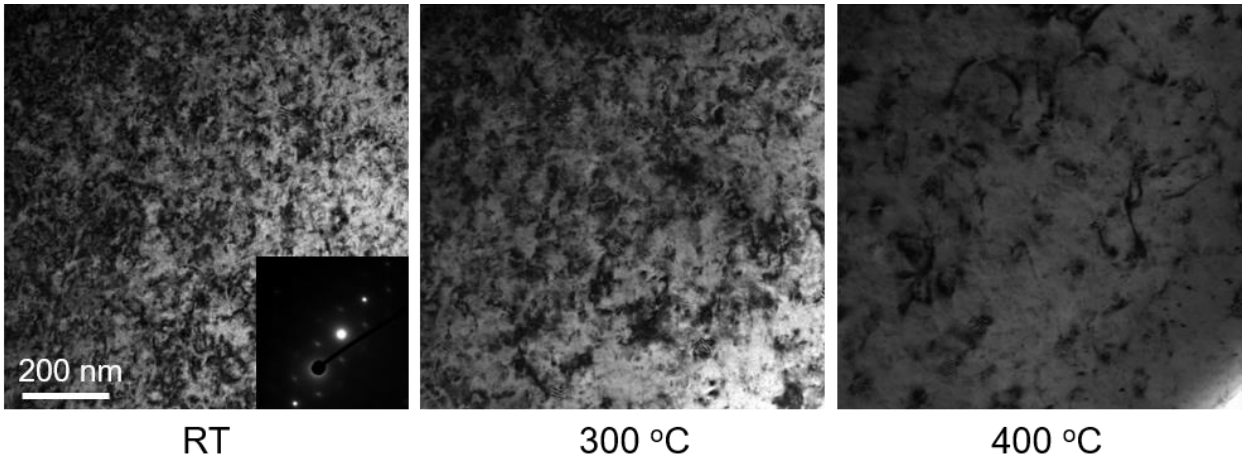


Figure 3-11: TEM images of CC3 alloy initially irradiated at -223 °C to 0.0625 dpa with 1 MeV Kr^{++} ions then sequentially post-irradiation annealed to RT, 300 and 400 °C. The imaging condition is g=022 for bright field with beam direction close to [100].

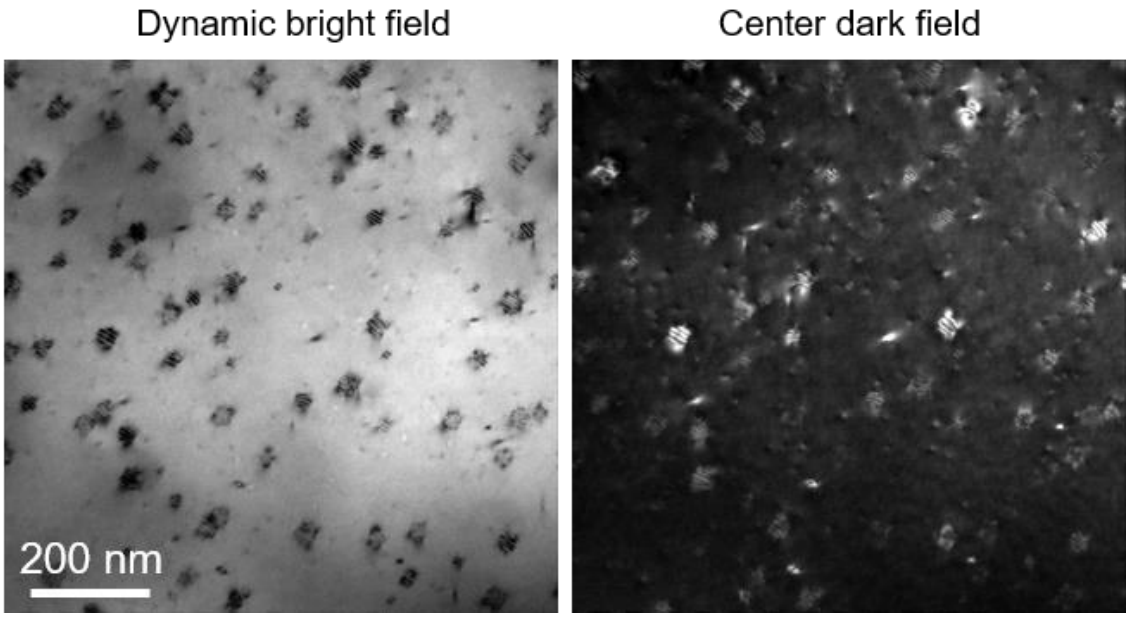


Figure 3-12: TEM images of CC3 alloy initially irradiated at -223 °C to 0.0625 dpa with 1 MeV Kr^{++} ions then post-irradiation annealed to 500 °C. The imaging condition is g=022 for bright field and center dark field with beam direction close to [100].

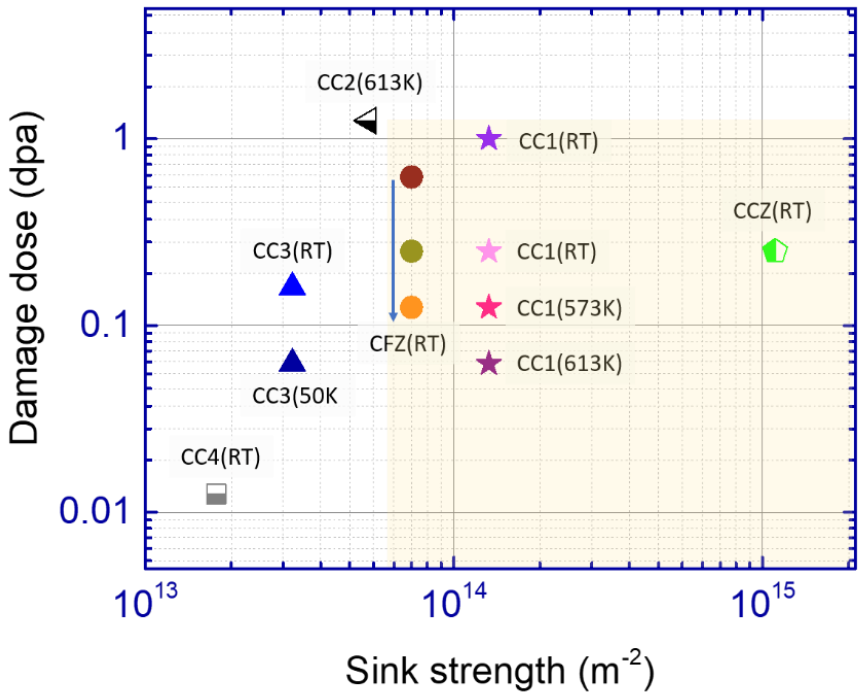


Figure 3-13: Summary of irradiation conditions in all the in situ irradiation experiments in CC1, CC2, CC3, CC4, CFZ and CCZ alloys.

3.3 Post-irradiation cross-section characterization after bulk ion irradiation

Ex situ ion irradiation experiments using 1 MeV Ni^{+} ions were applied on bulk CC1, CC2 and CFZ-0 alloys. The average grain diameter of thermal aged samples is around 150 μm (much larger than the ion irradiated range of 0.6 μm investigated in this work) and the observed unirradiated dislocation density was very low. Therefore, the majority of the irradiation-induced point defects and defect clusters would be preferentially trapped at the interface between Co precipitates and the matrix because of their affinity in terms of lattice strain.

3.3.1 Damage region

Precipitate stability in irradiated alloys is a competition between ballistic dissolution and radiation enhanced coarsening. At high temperatures, precipitates tend to gradually coarsen due to radiation enhanced diffusion. Conversely, at low temperatures where solute diffusion via substitutional (vacancy) diffusion is limited, ballistic dissolution becomes dominant and causes precipitate shrinkage. In this research, precipitates may be expected to slightly dissolve at 25 ℃ and maintain the same size at 350 ℃ to three different doses, since the recovery "stage III" temperature in Cu is near -23 ℃ [60]. Figure 3-14 shows TEM-EDS mappings of CC2, CC1 and CFZ alloys irradiated with 1MeV Ni ions to a peak dose of 12 dpa at 25 (RT) and 350 ℃. The white dotted line is separating the irradiated regions from non-irradiated regions. CC2 alloy with lower sink strength of 5.3×10^{13} m^{-2} show a slight precipitate coarsening effect in damaged regions with a mean size of 22.5 nm compared to the initial precipitate mean size of 19.6 nm. CC1 alloy and CFZ alloy show stable precipitate sizes in the irradiated regions, indicating that ballistic dissolution is not predominant and that there's not much coarsening effect on Co and Fe precipitates for RT and 350 ºC irradiation to 12 dpa. Precipitate dissolution tends to become pronounced for energetic displacement cascade irradiation conditions when the precipitate size is comparable to or smaller than the displacement cascade size (~5 nm) and when solute diffusion is sluggish (e.g. when the irradiation is performed at temperatures near or below the onset temperature for vacancy migration). Similarly, precipitate coarsening would be expected for conditions where there is very high solute mobility.

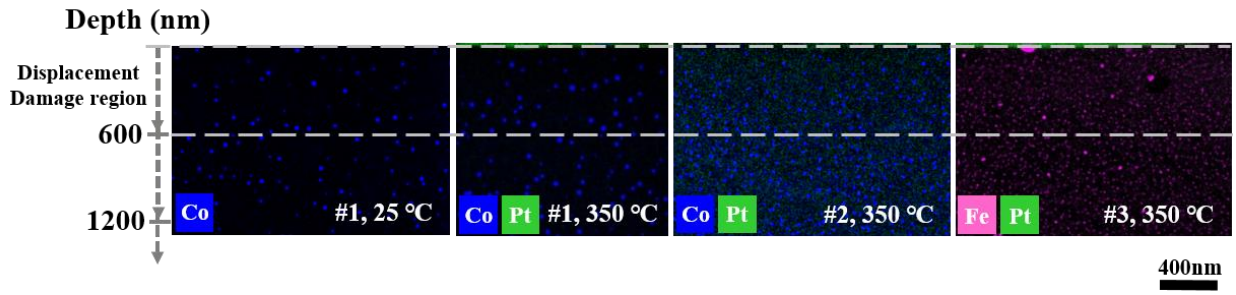


Figure 3-14: TEM-EDS mappings of CC2, CC1 and CFZ alloys irradiated with 1 MeV Ni^{+} ions to a mid-range dose of 10 dpa at 25 and 350 ℃.

3.3.2 Post-irradiation microstructure after room temperature irradiation

Microstructures of CC2 alloy with the sink strength of 5.3×10^{13} m^{-2} irradiated at RT to mid-range dose of 1 and 10 dpa are shown in Figure 3-15 and Figure 3-16, respectively. The imaging conditions are both g=220 dynamic for BF image. Figure 3-15 shows precipitates remain coherent beyond the irradiated region. Conversely, Figure 3-16 shows precipitate loss of coherency extends to a depth of 1100 nm from the surface, which is ~550 nm beyond the end of the directly irradiated region; this indicates that surviving defects from the irradiated region are able to diffuse long distances (hundreds of nm) and interact with precipitates.

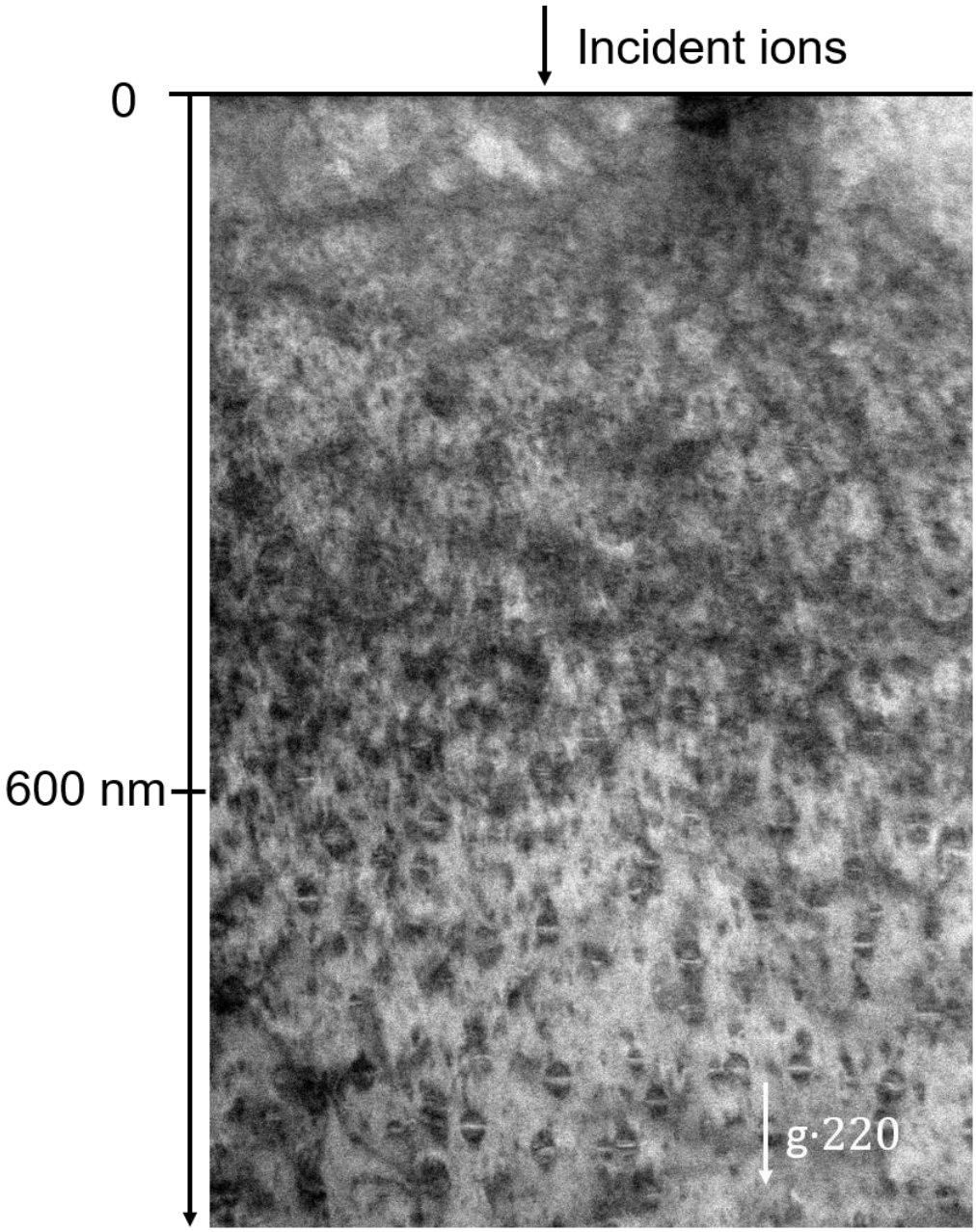


Figure 3-15: Cross-section TEM microstructure of CC2 alloy irradiated with 1 MeV Ni^{+} ions at RT to a mid-range dose of 1 dpa.

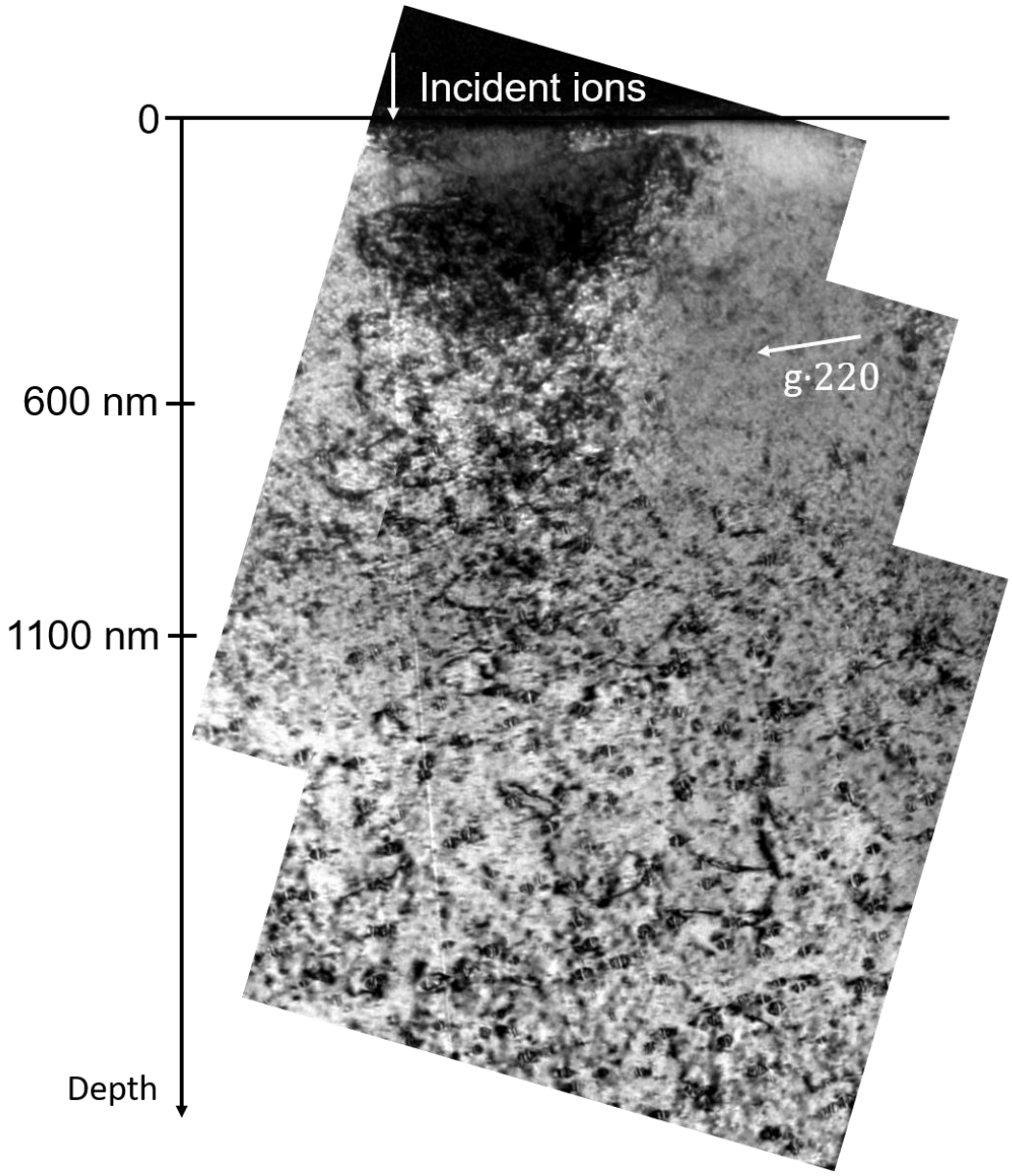


Figure 3-16: Cross-section TEM microstructure of CC2 alloy irradiated with 1 MeV Ni^{+} ions at RT to a mid-range dose of 10 dpa.

3.3.3 Post-irradiation microstructure after high temperature irradiation

The STEM-BF images of CC1 alloy with the sink strength of 1.3×10^{14} m^{-2} irradiated at 350 ℃ to mid-range dose of 10 dpa are shown in Figure 3-17. Co precipitates were observed in different depth regions and remained coherent within and beyond the radiated regions.

Figure 3-18 and Figure 3-19 display the precipitate microstructure of CC2 alloy, following irradiation to a mid-range dose of 10 dpa, under two different g=220 dynamic diffraction conditions. Here, three interesting regions were observed, each of which is depicted in several high magnification BF and DF images highlighted by numbers in the center cross-section BF image (Figure 3-19). The first region is called 'incoherent region' and is visible through the whole ion-irradiated region (depths of 0 to 600 nm). In this region, Co-precipitates lose coherency due to absorption of interstitials and vacancies at the interface of the coherent precipitate with the matrix and become totally incoherent with the matrix. In other words, the precipitate loss of coherency is indicative that the coherency strain is relieved by absorbing radiation defects. The third region we call 'coherent region'; it has uniformly distributed coherent and spherical precipitates and is located a couple of micrometers deeper than the irradiated region. In the second intermediate region between the irradiated incoherent region and deep unirradiated coherent region, where incoherent and coherent precipitates co-existed, approximately 90% of the Co precipitates become incoherent with some small dislocation loops nearby. This transition region extends from the irradiated maximum depth ('end of range') to 1700 nm beyond the end of range.

Figure 3-20 and Figure 3-21 are TEM images of CFZ-0 alloys irradiated at 350 ^{o}C to mid-range dose of 0.1 dpa and 10 dpa. No coherency loss is observed in both of the irradiation conditions, either within the ion irradiation region or beyond.

3.3.4 Post-irradiation microstructure after cryo-temperature irradiation

Cryo-temperature irradiations were performed to more specifically explore the interstitial diffusion behavior since at this temperature, vacancy defects are immobile, whereas single interstitial atoms and small interstitial clusters are expected to be highly mobile in Cu. However, even in the low sink strength CC2 alloys, precipitates were observed to retain their coherency

within and beyond the irradiated regions (Figure 3-22). This implies that interstitial defects may be less mobile than expected based on MD simulation studies.

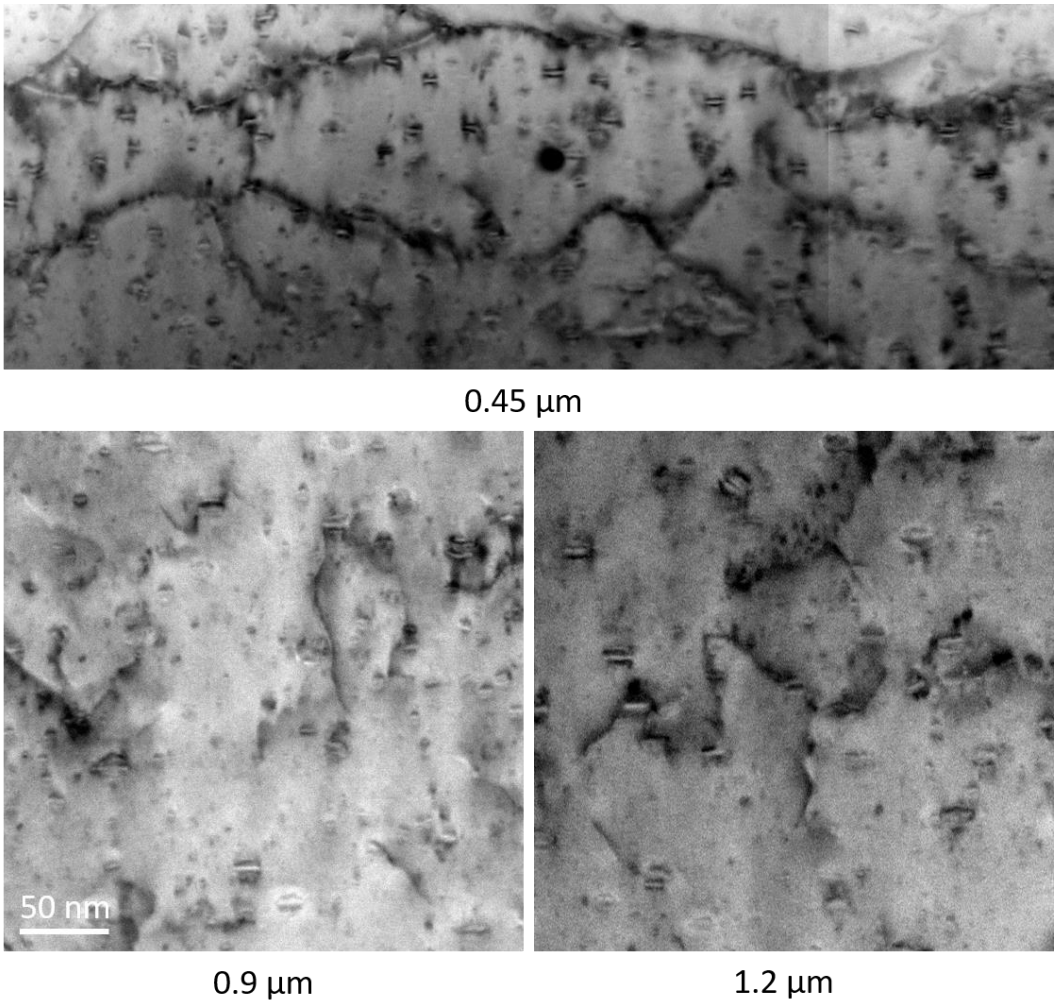


Figure 3-17: Cross-section STEM-BF images of CC1 alloy irradiated with 1 MeV Ni^{+} ions at 350 ^{o}C to a mid-range dose of 10 dpa. The cross-section depth at the center of the image is indicated below the photos. All images are at the same magnification.

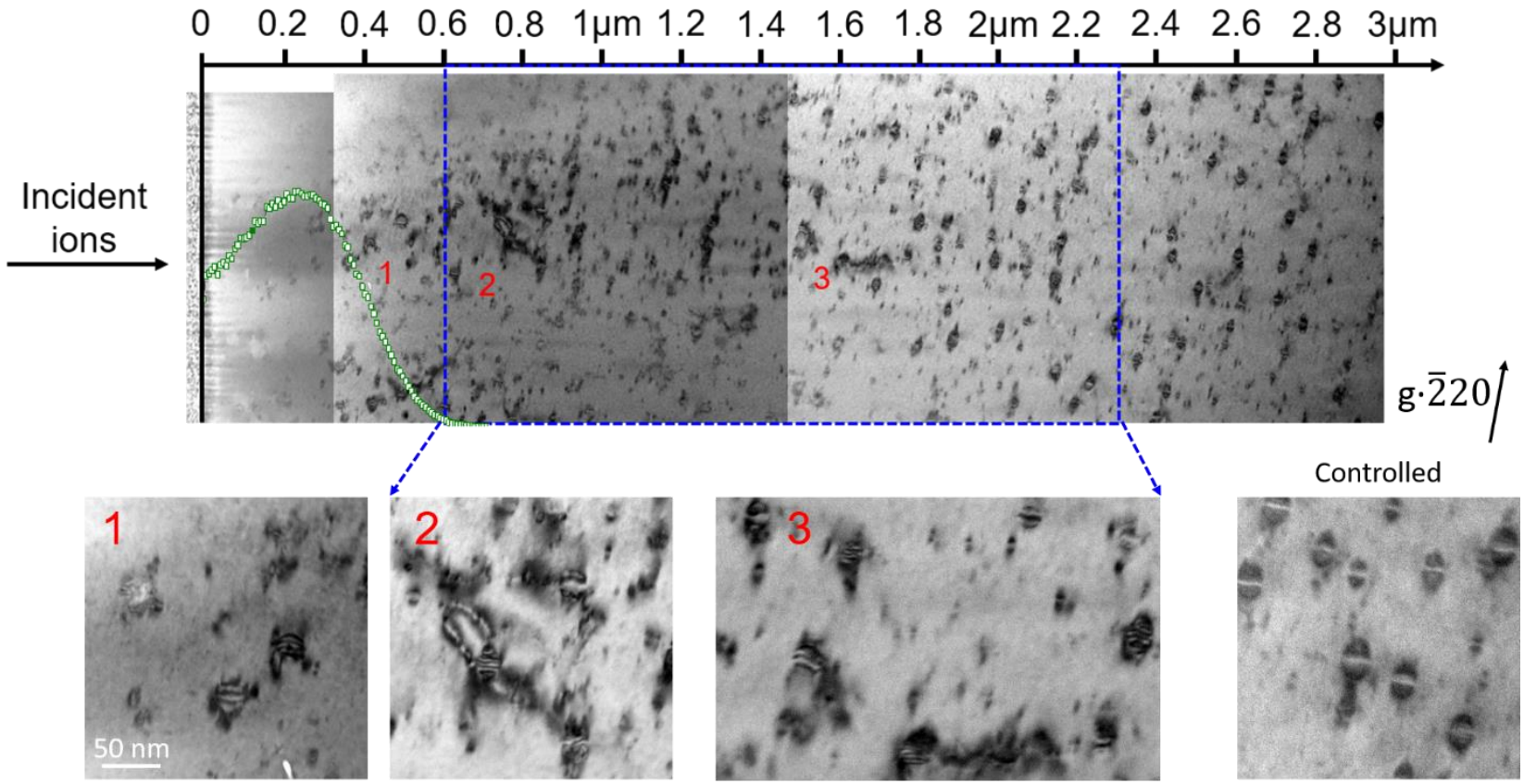


Figure 3-18: Cross-section STEM-BF images of CC2 alloy irradiated with 1 MeV Ni^{+} ions at 350 ^{o}C to a mid-range dose of 10 dpa.

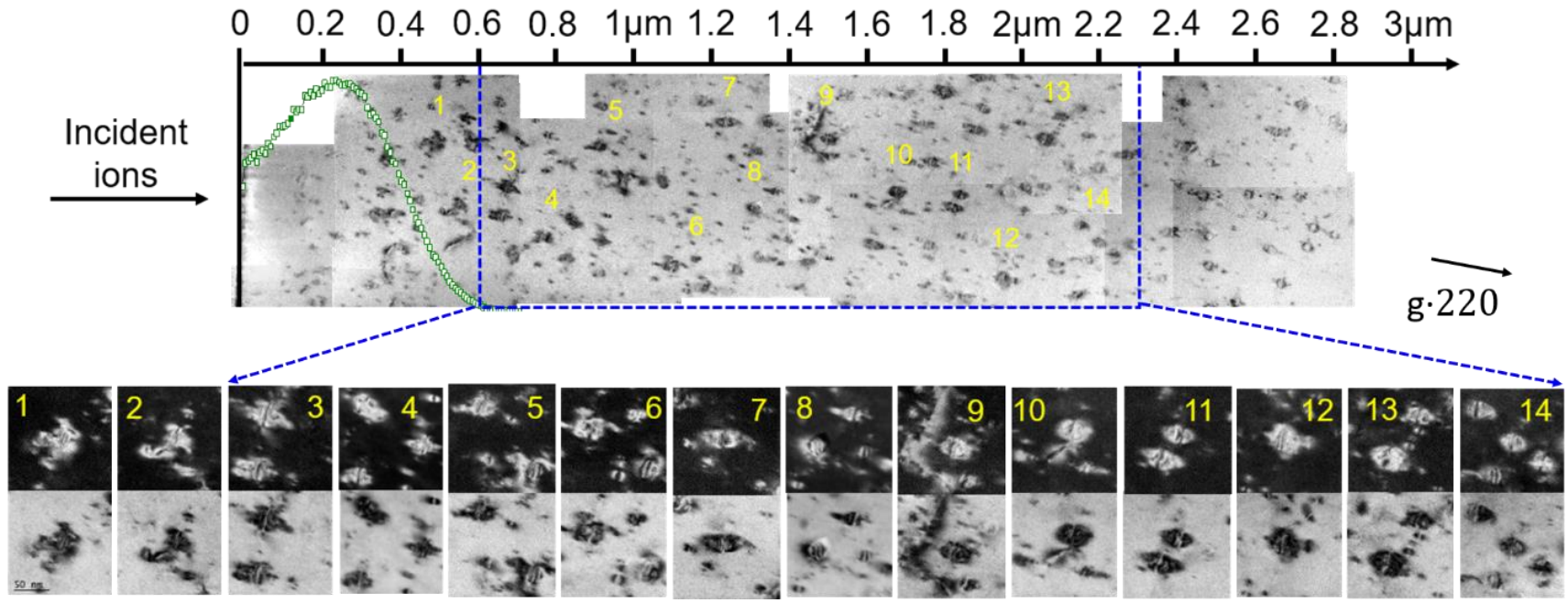


Figure 3-19: Cross-section STEM-BF images of CC2 alloy irradiated with 1 MeV Ni^{+} ions at 350 ^{o}C to a mid-range dose of 10 dpa.

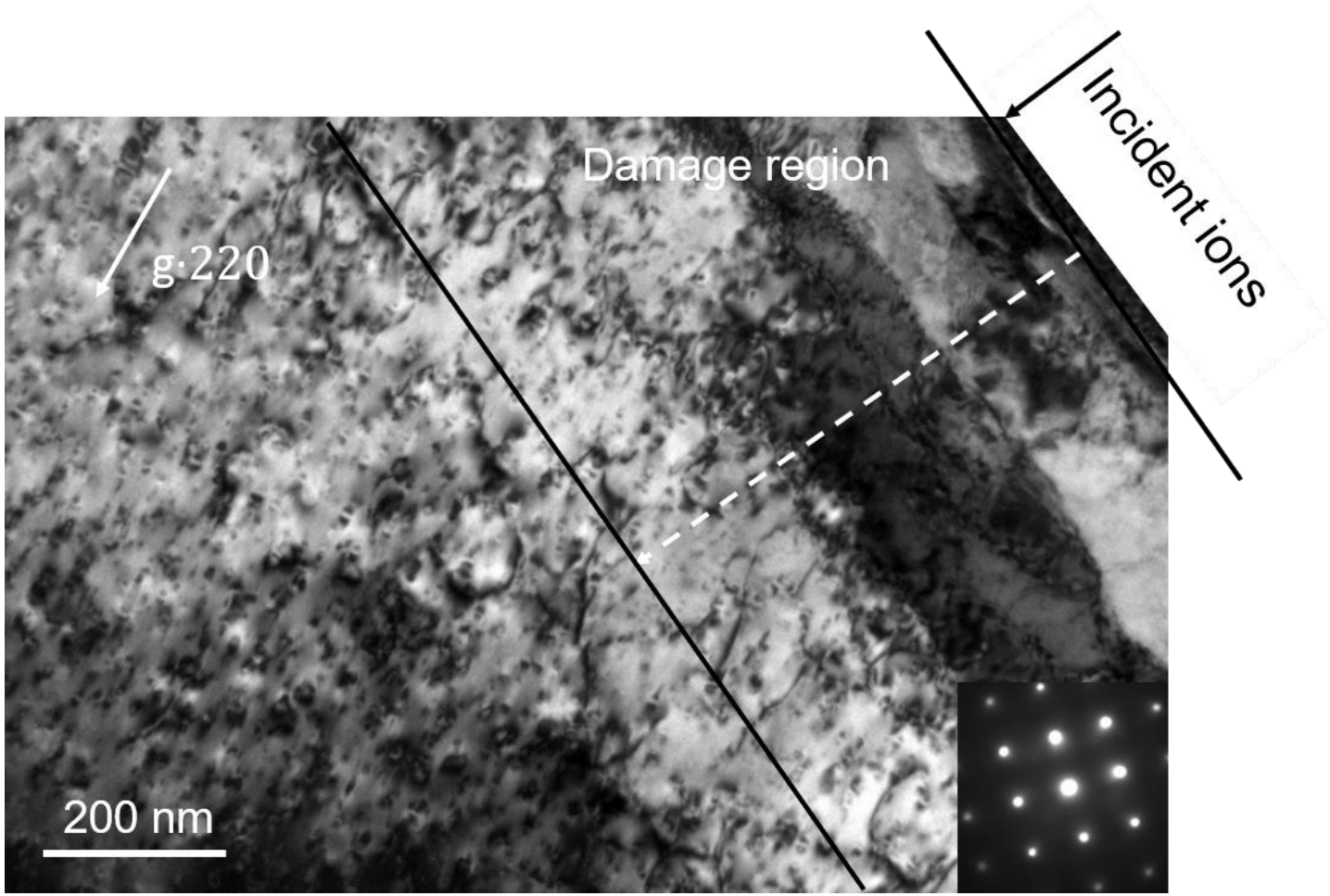


Figure 3-20: Cross-section TEM microstructure of CFZ-0 alloy irradiated with 1 MeV Ni^{+} ions at 350 ^{o}C to a mid-range dose of 0.1 dpa.

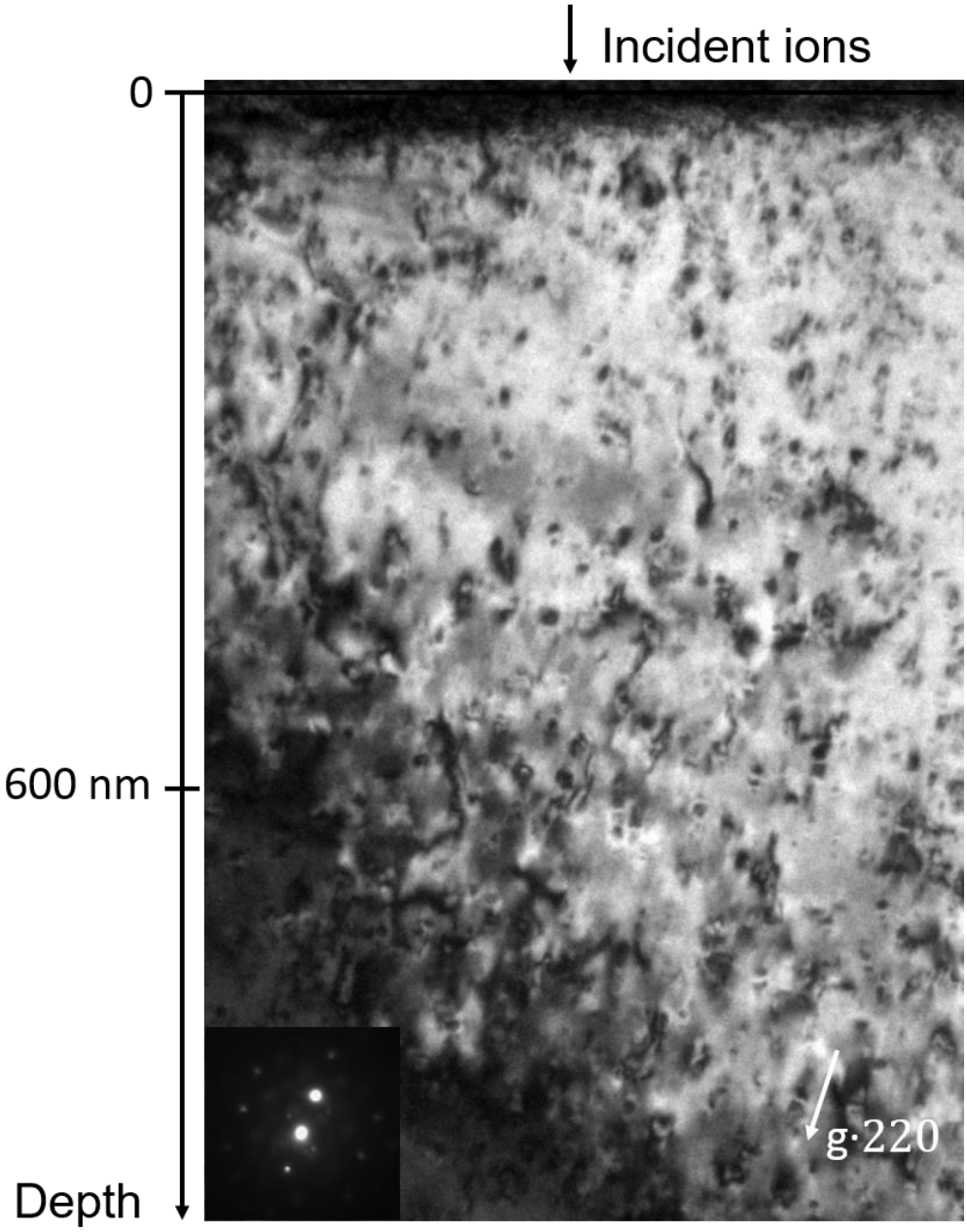


Figure 3-21: Cross-section TEM microstructure of CFZ-0 alloy irradiated with 1 MeV Ni^{+} ions at 350 ^{o}C to a mid-range dose of 10 dpa.

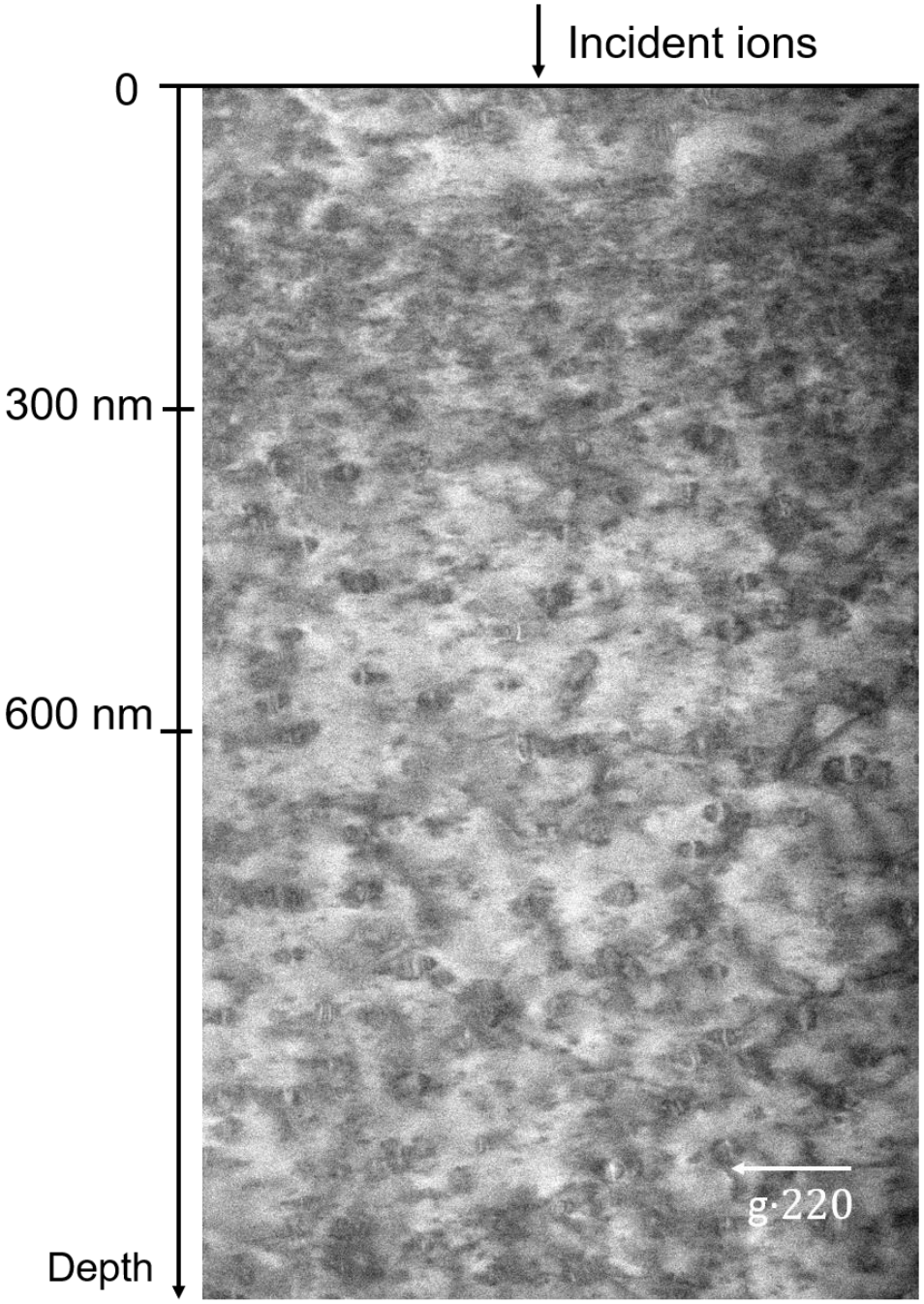


Figure 3-22: Cross-section TEM microstructure of CC2 alloy irradiated with 1 MeV Ni^{+} ions at -117 °C to a mid-range dose of 1 dpa.

3.3.5 Post-irradiation summary of precipitate stability within and beyond damage region

(1) TEM-EDS mappings showed good phase stability of Co and Fe precipitates after ion irradiation experiments at 25 and 350 ^{o}C up to ~10 dpa. Slight coarsening was observed in the Co precipitates in the lower sink strength CC2 alloy after 10 dpa, whereas no significant change in precipitate size or density was observed for the irradiated Co precipitates in the higher sink strength CC1 alloy or for the Fe precipitates in the CFZ alloy. These results indicate that there's no significant irradiation induced dissolution or coarsening effects for the examined irradiation conditions.

(2) Incoherent precipitates were observed in CC2 alloys with the relatively low precipitate sink strength of 5.3×10^{13} m^{-2}, existing well beyond the nominal maximum 600 nm depth of irradiated region due to the migration behavior of SIAs clusters under irradiation condition at 25 and 350 ^{o}C with dose of 1 and 10 dpa. However, no evidence of precipitate coherency loss was obtained in the CC2 alloys for a dose of 0.1 dpa at RT or after 1 dpa at -117 ^{o}C (Figure 3-23).

(3) Evidence for pronounced defect migration beyond end of ion irradiation region (much larger ranges than can be attributed to 3D motion of mobile radiation defects) suggests significant 1D migration of defect clusters.

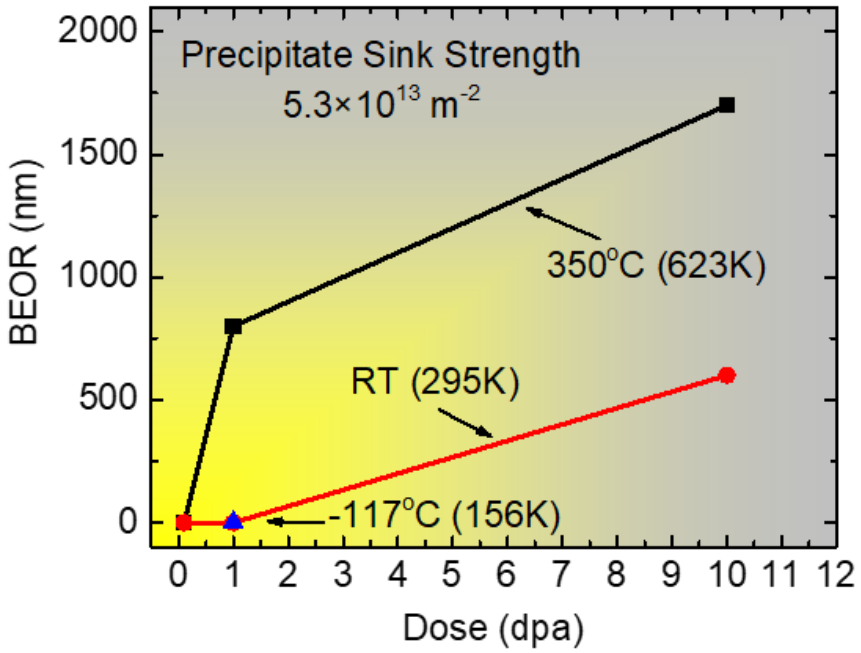


Figure 3-23: Observed BEOR loss of coherency versus dose.

3.4 Precipitate characterization in as-fabricated and creep-tested CuCrNbZr alloys

For the second topical theme investigated in this thesis, the precipitates in a newly designed high strength, high conductivity copper alloy were extensively characterized and compared with creep properties in order to uncover the roles of the various produced precipitates. A Cu based CuCrNbZr alloy has been developed with the aid of computational thermodynamics and fabricated through economic conventional ingot-metallurgy methods. The new alloy is designed to produce a multimodal distribution of precipitates in microstructure to improve creep behavior. The large Cr_2Nb Laves precipitates with typical size of 300~500 nm are distributed along grain boundaries (Figure 3-24 and Figure 3-25), dislocation lines and stacking faults. Two sizes of Cr precipitate sizes were observed. The coarser ones with a size from 150 to 350 nm can precipitate at both grain boundaries (Figure 3-26 and Figure 3-27) and in the grain interior (Figure 3-24 and Figure 3-27) and are formed during the latter stages of solidification or the solutioning process. The fine scale Cr precipitates with size of 5~10 nm are homogeneously distributed in the Cu matrix and form during the final aging treatment at 475 ^{o}C (Figure 3-26). The high density of fine-scale Cr precipitates (10^{22} m^{-3}) forming coherent interfaces with the Cu matrix [48], and are similar to the coherent Cr matrix precipitates examined in the irradiation effect on precipitate coherency presented earlier (Theme I, Chapter 3.2). Table 3-2 summarizes the screening test results on room temperature hardness, electrical resistivity and tensile properties of the first scoping heat of the CuCrNbZr alloy. The measured properties are comparable for samples initially given 50 and 70% deformation prior to solution annealing and aging except for the elongation and ultimate strength being somewhat lower for the 50% cold-work condition. The heavier deformation may be more efficient to evenly nucleate the Cr_2Nb clusters, leading to greater tensile elongation. However, this batch of alloys was found to high Fe and Sn impurities in the matrix (Figure 3-25), which degraded their room temperature tensile properties and deteriorated the thermal conductivity due to high amount of impurity solutes in the matrix.

Table 3-2: Summary of room temperature properties of the 1st heat of CuCrNbZr alloys [48].

Alloy and TMT	Hardness (VHN)	Electrical conductivity (%IACS)	Yield strength (MPa)	Ultimate strength (MPa)	Uniform elongation (%)	Total elongation (%)
CuCrNbZr-50 (50%CW+SAA)	123.2±1.9	55.8±1.1	230	336	12.2	21
CuCrNbZr-70 (70%CW+SAA)	126.2±7.7	56.7±0.5	255	385	20.2	29

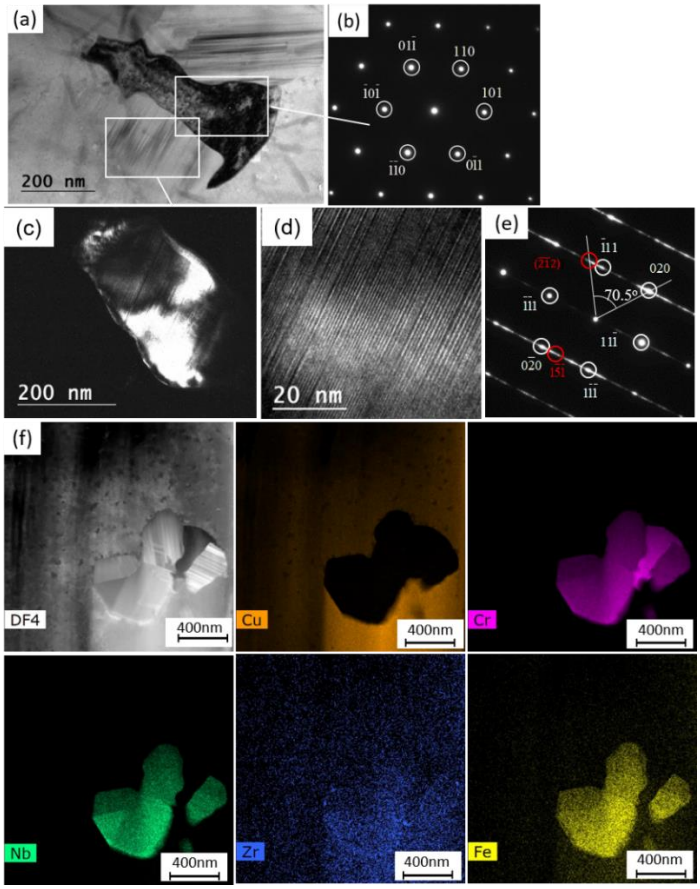


Figure 3-24: (a) TEM-BF image of a thermal aged CuCrNbZr alloy pre-cold rolled to 70% showing a large Cr precipitate in the matrix surrounded by a cluster of Cr_2Nb C15 Laves phase precipitates; (b) <111> SADP of Cr precipitate in (a); (c) CDF image of one of Laves phase precipitates selected with white rectangle in (a); (d) HRTEM image from the white rectangle in (a); (e) <110> SADP according to (d); (f) the individual composition maps of Cu, Cr, Nb, Zr, and Fe indicating that Zr is uniformly distributed both in the matrix and Laves phases.

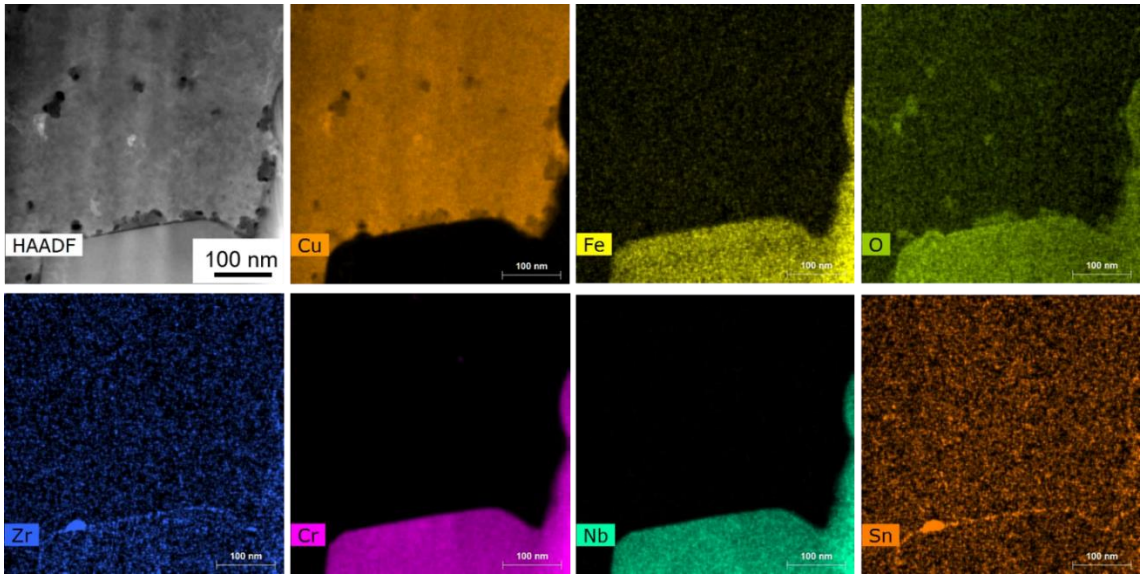


Figure 3-25: HAADF image and elemental TEM-EDS mappings of Cu, Fe, O, Zr, Cr, Nb and Sn focused on the Laves precipitate/matrix interface.

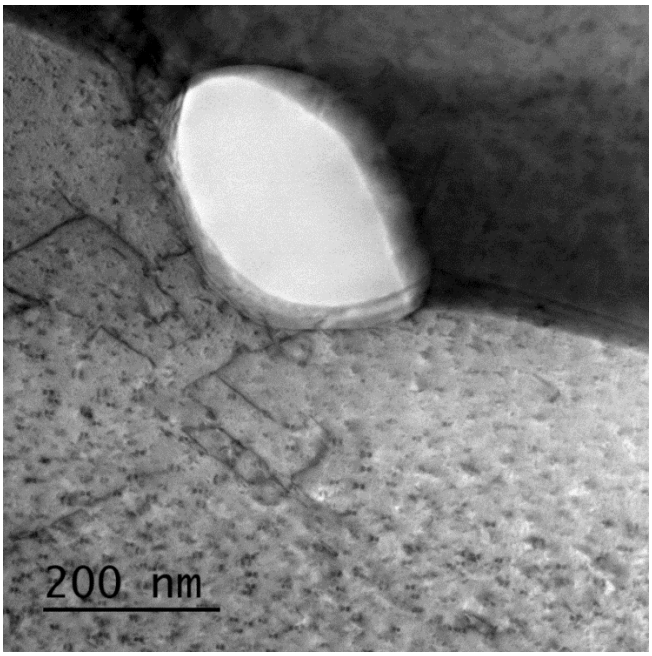


Figure 3-26: STEM-BF image showing a Cr precipitate located at the grain boundary and matrix coherent Cr precipitates uniformly distributed. This grain boundary precipitate will be characterized in detail later.

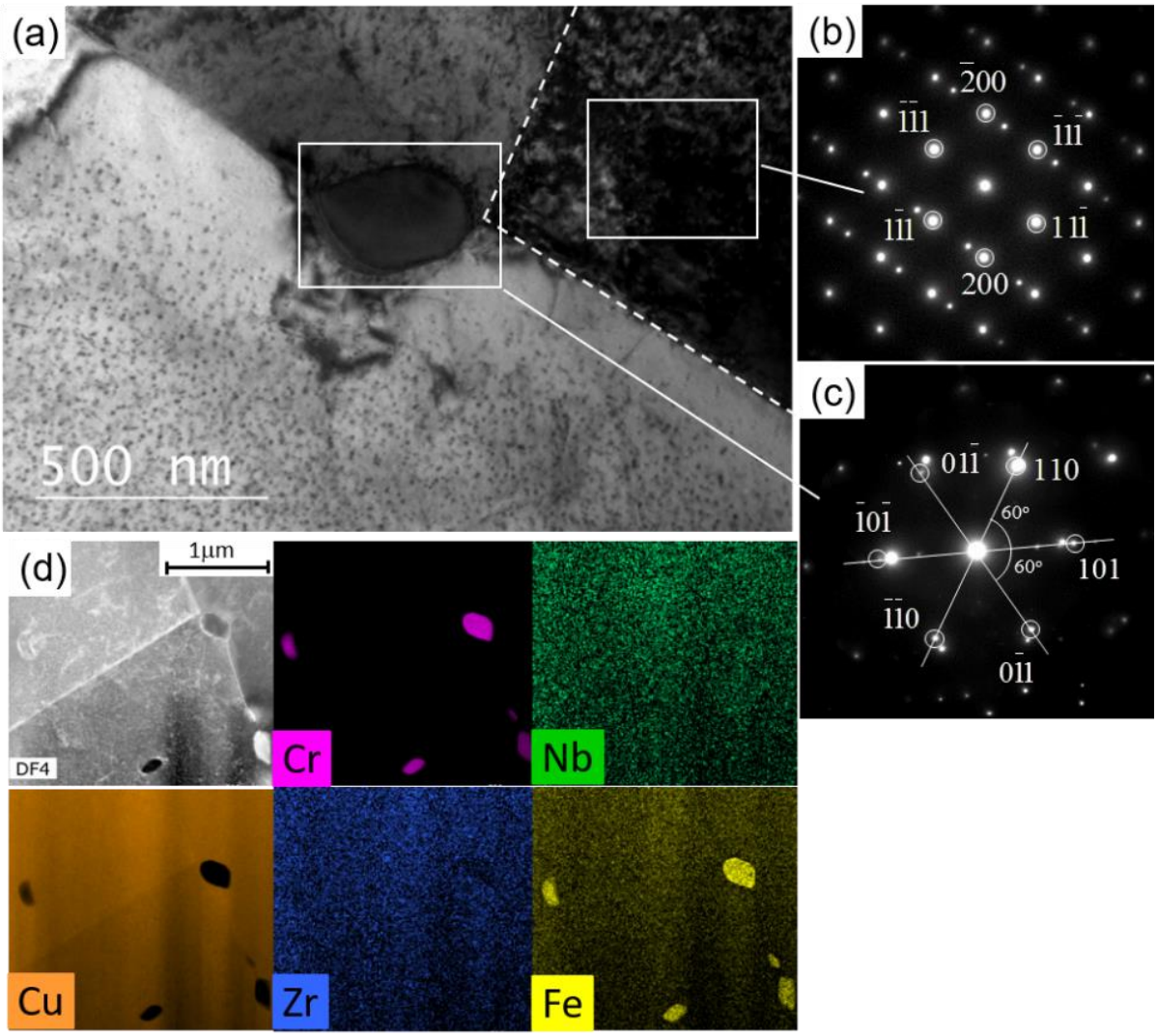


Figure 3-27: (a) TEM-BF image of the CuCrNbZr_70 alloy showing a coarse Cr precipitate located at the grain boundary; (b) <110> SADP of the right grain in (a) marked with white dotted lines; (c) <111> SADP of the grain boundary Cr precipitate in (a); (d) STEM-BF image on a larger area and the individual composition maps Cu, Cr, Nb, Zr and Fe [48].

The subsequent experimental results focused on the examinations of a high-purity CuCrNbZr (CuCrNbZr_HP) alloy heat with the same designed chemistry but reduced levels of impurities. This alloy was first screened by electrical resistivity and tensile testing, and then followed by a systematic study on creep properties at 500 ^{o}C under various applied stress levels of 90 to 140 MPa. Relations between microstructure and creep property were carefully studied and compared with a commercial Kablemeta CuCrZr (CuCrZr) alloy.

3.4.1 Electrical resistivity and Vickers hardness

The average electrical resistivity value of the three as-fabricated CuCrNbZr_HP alloys was measured to be 2.39×10^{-8} ohm·m, and the corresponding electrical conductivity was 72.1 %IACS (International Annealed Copper Standard) which is slightly lower than 83.4 %IACS for the CuCrZr alloy [17], shown in Table 2-3**.** Based on thermodynamic calculation, the solubilities of Cr and Zr elements in Cu are similar for the CuCrZr and CuCrNbZr_HP alloys, and well below their measured chemical concentrations. Thus, the main difference of the electrical resistivity values is due to the addition of Nb in the CuCrNbZr_HP alloy. From Reference [61] and [62], specific resistivity of 4.5×10^{-8} ohm·m/wt. % for Nb solutes is applied when assuming a Nb solubility of 0.09 wt.% at 475 ^{o}C. Using Matthiessen's Rule, the corresponding conductivity of the Cu alloy would be 81 %IACS (only consider the Nb solute contribution). If we assume the same resistivity contribution from Cr solute in the CuCrZr and CuCrNbZr_HP alloys of 3.4×10^{-8} ohm·m/wt.%, then the calculated CuCrNbZr_HP conductivity based on Cr and Nb solubility would be 70 %IACS, which is close to our experimental observation. Details of electrical resistivity calculations can be found in Table 3-3.

The Vickers hardness (Table 2-2) of the CuCrNbZr_HP alloy was 137.9±7.0 VHN, which is comparable to that of the CuCrZr alloy 135.8±6.2 VHN. It may suggest that the coarse Laves phase produced in newly developed CuCrNbZr_HP alloy had slightly positive effect on hardness.

Table 3-3: Room temperature electrical resistivity and conductivity calculations for CuCrZr and CuCrNbZr_HP alloys.

	Solubility at 475 °C (wt.%)	Resistivity increase per 1 wt.% addition (10^{-8} ohm·m)	Resistivity (10^{-8} ohm·m)/Conductivity (%IACS)	
			CuCrZr	CuCrNbZr_HP
Cu	100	1.72	2.05/84.1	2.45/70.2
Cr	≤0.05	4.90		
Nb	≤0.09	4.50		
Zr	≤0.01	8.0		

3.4.2 XRD results

Figure 3-28 shows the XRD pattern of as-aged CuCrNbZr_HP alloy. Three phases were identified, in agreement with the computational thermodynamic predictions: Laves_Cr_2Nb with the C15 structure (cF24, Cu_2Mg prototype), Cr with body centered cubic (bcc) structure, and Cu with fcc structure. Their lattice parameters in the CuCrNbZr_HP alloy were measured to be 6.9968, 2.8839 and 3.6163 Å, respectively, which agree well with the experimental values of 6.9913 Å [63], 2.8949 Å [64] and 3.6150 Å [65] for the respective phases. Their measured weight fractions in the alloy were 3.34, 0.57 and 96.09 %, respectively, which are in agreement with values of 3.10, 0.41 and 96.49% predicted from thermodynamic calculations.

3.4.3 Optical microscopy and SEM results

Figure 3-29 (a) and (c) show representative optical microstructures of the CuCrZr and CuCrNbZr_HP alloys in the as-aged conditions. A low density of moderate-sized round precipitates (diameter ~1 to 3 μm) are present in both alloys. SEM-EDS line scans shown as inset images in Figure 3-29 (b) and (d) show that these spherical micron-size features are Cr precipitates

with some dissolved Zr. The large and faceted precipitates (2~11 μm) in the CuCrNbZr_HP alloy are (Cr, Nb)-rich particles, as indicated by short red arrows in Figure 3-29 (c) and (d). Based on thermodynamic calculations and the XRD results in Figure 3-29, these large (Cr, Nb)-rich phases correspond to the Laves_Cr_2Nb phase with the C15 structure. These large faceted Cr_2Nb phase are formed from liquid during solidification. The pits shown in Figure 3-29 (d) are the places where brittle Laves phase dropped off the sample surface during mechanical polishing. We also observed the grains in the CuCrZr alloy were more uniform than those in the CuCrNbZr_HP alloy. By using a method of average number of grains intercepted by a line of fixed length, the mean grain diameter of the CuCrZr alloy was 39±5 μm, while the grain size of the CuCrNbZr_HP alloy exhibited a bi-model distribution: small grains associated with Laves grain boundary precipitation with a mean grain size 22±1 μm and large grains that contained few or no detectable Laves precipitates with a mean grain size of 104±23 μm. The overall mean size of the CuCrNbZr_HP alloy was 38±6 μm. The non-uniform grain size in CuCrNbZr_HP alloy suggests that the Laves precipitates formed during solidification impede growth of recrystallized grains during the solution anneal and aging thermal treatments.

3.4.4 Nano-scale precipitates

In addition to the large micron-sized Cr_2Nb precipitates, sub-micron Cr_2Nb precipitates were also observed in the CuCrNbZr_HP alloy. The TEM- high angle annular dark field (HAADF) image in Figure 3-30 (a) shows one of these precipitates located in the grain interior. The corresponding elemental mappings in Figure 3-30 show that this Laves phase consists of Cr and Nb elements only. The anomalous presence of high oxygen content in the precipitate is attributed to the overlap of the respective EDS peak positions for oxygen (L_3:575 eV) and chromium (K_1:532 eV). In the vicinity of the matrix Laves_Cr_2Nb phase, Zr-rich particles were observed with irregular shape and slightly enriched oxygen (see Fig. 4(a)), indicating the oxygen gettering effect of Zr. Figure 3-30 (b) shows the selected area electron diffraction pattern under <110> zone axis of the C15-Laves phase precipitate from the dashed blue rectangle region in Figure 3-30 (a), it revealed its characteristic twinned diffraction in the <110> zone axis, similar to Kazantzis's observation [66]. Figure 3-30 (c) shows the corresponding high-resolution TEM image with intense stacking faults and the fast Fourier transform (FFT) as an inset image, indicating the C15

cubic structure of Laves_Cr_2Nb phase. According to our computational thermodynamic analysis, these sub-micron Cr_2Nb precipitates are precipitated during solution annealing at 970 °C. Both types of Laves_Cr_2Nb phases that formed during solidification and 970 °C solutionization, respectively, are calculated to be thermodynamically stable during prolonged creep testing at 500 °C.

Intermetallic Cu_5Zr was observed as a second general type of precipitate in the as-aged CuCrNbZr_HP alloy, in agreement with computational thermodynamics predictions. The STEM-BF image in Figure 3-31 (a) shows the disc-shaped Cu_5Zr precipitates along $(\overline{1}11)$ and $(\overline{1}1\overline{1})$ habit planes of the Cu matrix. The size of the Cu_5Zr was between 20-40 nm, and the number density was 10^{21} m^{-3}. Figure 3-31 (b) shows a Cu matrix [112] SAED pattern showing the precipitation orientation relationship of Cu_5Zr with the Cu matrix, where the spots from Cu_5Zr are marked with red circles and those from the Cu matrix with blue circles. The orientation relationship, $[112]_{Cu} \parallel [011]_{Cu_5Zr}$, $(11\bar{1})_{Cu} \parallel (11\bar{1})_{Cu_5Zr}$, shown in Figure 3-31 (b) indicates the habit planes of these disc-shaped Cu_5Zr phases are parallel to [59] planes of the Cu matrix. The HRTEM image in Figure 3-31 (c) was taken near the Cu matrix [011] zone axis with the corresponding FFT pattern shown in Figure 3-31 (d), where the matrix spots are marked with dashed white circles, confirming the Cu_5Zr disc plane is parallel to the Cu matrix $(\overline{1}11)$ habit plane. The Cu_5Zr disc shape and precipitate/matrix orientation relationship are consistent with what has been observed in dilute Cu-Zr binary alloys or CuCrZr alloy systems after thermal aging below 500 °C [67].

The third major type of precipitation, matrix Cr precipitates that were observed in both the CuCrZr and CuCrNbZr_HP alloys, were characterized using STEM-BF techniques. The diffraction spots marked by purple triangles in Figure 3-31 (b) are from the bcc Cr precipitates, indicating the Nishiyama-Wassermann (N-W) orientation relationship exists between bcc Cr precipitates and fcc Cu matrix [31]. The matrix Cr precipitates were very small, typically ~3.4 nm in diameter for the CuCrZr alloy and ~5 nm for the CuCrNbZr_HP alloy, as shown in Figure 3-32 (a) and (c), respectively. The larger size of the Cr precipitates in the CuCrNbZr_HP alloy is attributed to the longer aging time (3 h for CuCrNbZr_HP vs. 2 h for CuCrZr). The uniformly distributed and spherical Cr precipitates show coherent features with a "no contrast line" located perpendicular to the diffraction $\boldsymbol{g}$ vector $\langle 200 \rangle$ under dynamical diffraction conditions (Figure 3-32 a, c). The TEM_EDS mappings of Cr in Figure 3-32 (b) and (d) show the Cr precipitates are

homogeneously distributed in the matrix, with a measured number density of 10^{22} m^{-3} in both of the alloys.

3.4.5 Tensile test results

To compare the tensile and ductility properties of the newly developed CuCrNbZr_HP alloys with relevant high strength Cu alloys at various temperatures, Some tensile properties of the CuCrNbZr_HP alloys are plotted and compared with the CuCrZr and other high-strength, high conductivity Cu alloys (including ITER grade CuCrZr, GlidCop Al25 and CuCrNb alloys) at various temperatures in Figure 3-33 (a) and (b) [68]. From room temperature to 500°C, the ultimate tensile strengths of the CuCrNbZr_HP alloy are near the upper ranking among all alloys with values of ~450 MPa at room temperature and ~220 MPa at 500 ^{o}C, while the corresponding uniform elongations are in the middle of all plotted alloys with values that slowly decrease from ~15% to ~6% with increasing temperature. The 0.2% yield strengths of CuCrZr and CuCrNbZr_HP alloys at 24, 300 and 500 ^{o}C are shown in Table 3-4. At 500 ^{o}C, the 0.2% yield strength of the CuCrNbZr_HP alloy is 212 MPa, higher than that of CuCrZr alloy (192 MPa), it may indicate that the Laves phase have some effect on increasing the yield strength in CuCrNbZr_HP alloys at high temperatures.

3.4.6 Creep test results

The creep tests were first performed in air at 500 °C and 90 MPa (Figure 3-34). The creep life of CuCrNbZr_HP alloy was 4.0×10^{5} s (~110 h), which was about 1.5 times longer than that of the reference CuCrZr alloy, 2.6×10^{5} s (~72 h). Significant oxidation occurred in both alloys under this creep test condition.

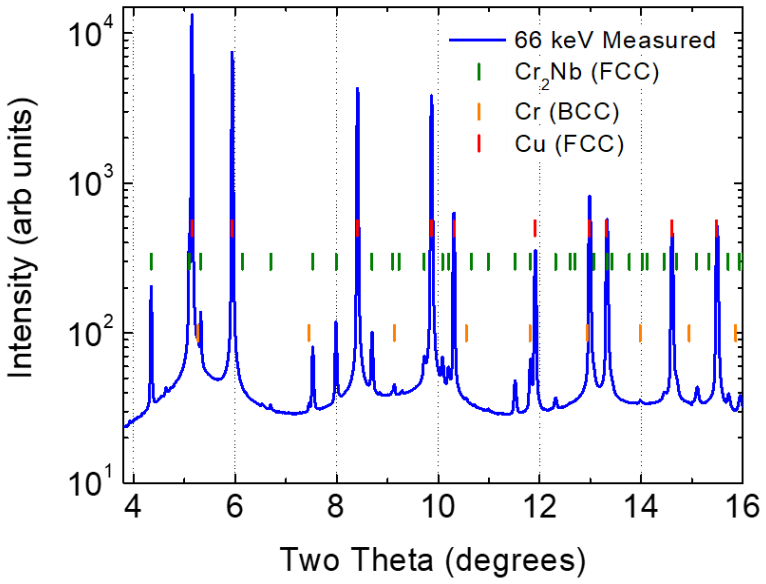


Figure 3-28: X-ray diffraction pattern of the CuCrNbZr_HP alloy in as-aged condition. (D. Sprouster, Stonybrook University)

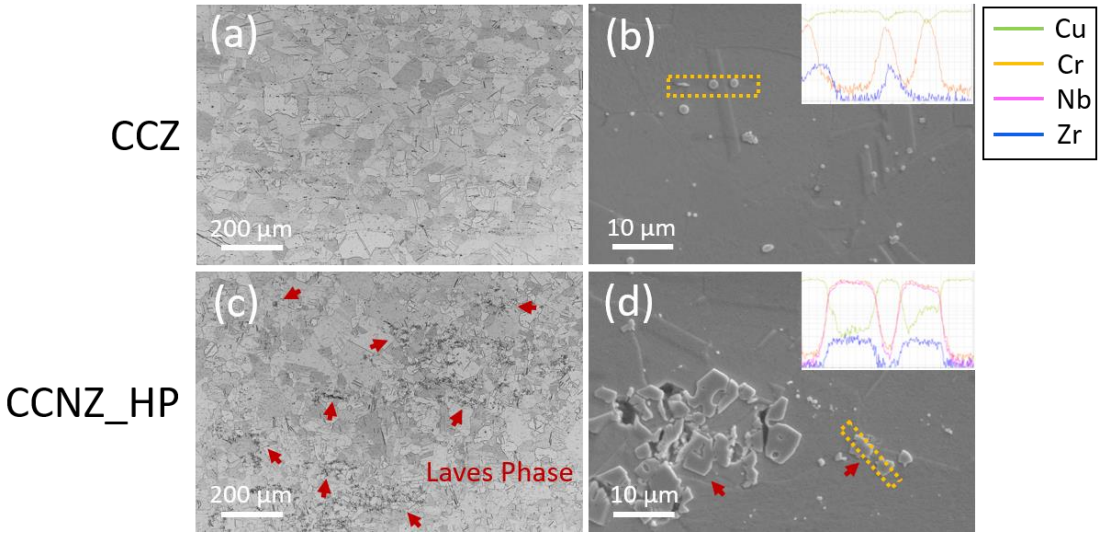


Figure 3-29: (a) and (c) are the optical microstructures of the grain morphologies of CuCrZr and CuCrNbZr_HP alloys in as-aged conditions, respectively; (b) and (d) are SEM images with the inset line scan results showing the chemical compositions of those micro-scale precipitates within and along the grain boundaries.

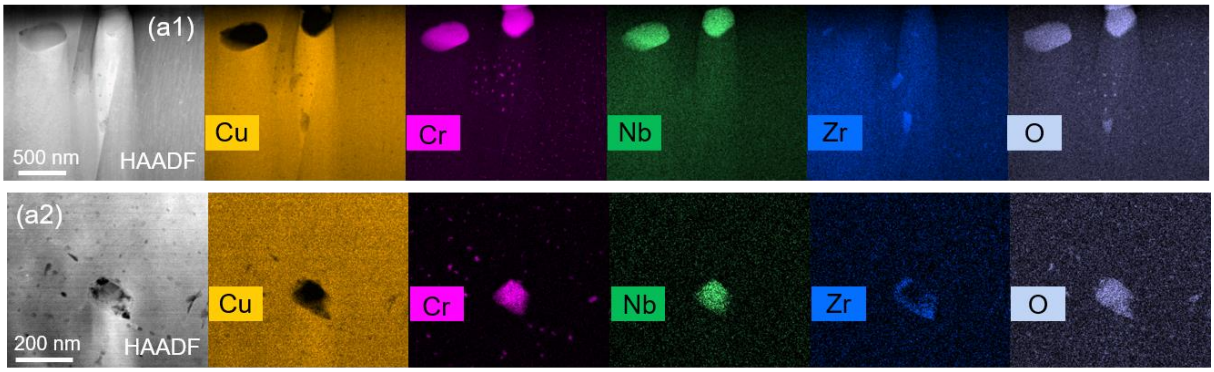


Figure 3-30: (a) HAADF image and elemental TEM-EDS mappings of Cu, Cr, Nb, Zr and O showing the laves phase Cr_2Nb precipitated in the matrix; (b) [110] SADP of the Laves_Cr_2Nb taken from dotted blue rectangle showing the C15-type cubic structure, and (c) the corresponding HRTEM image of Laves_Cr_2Nb.

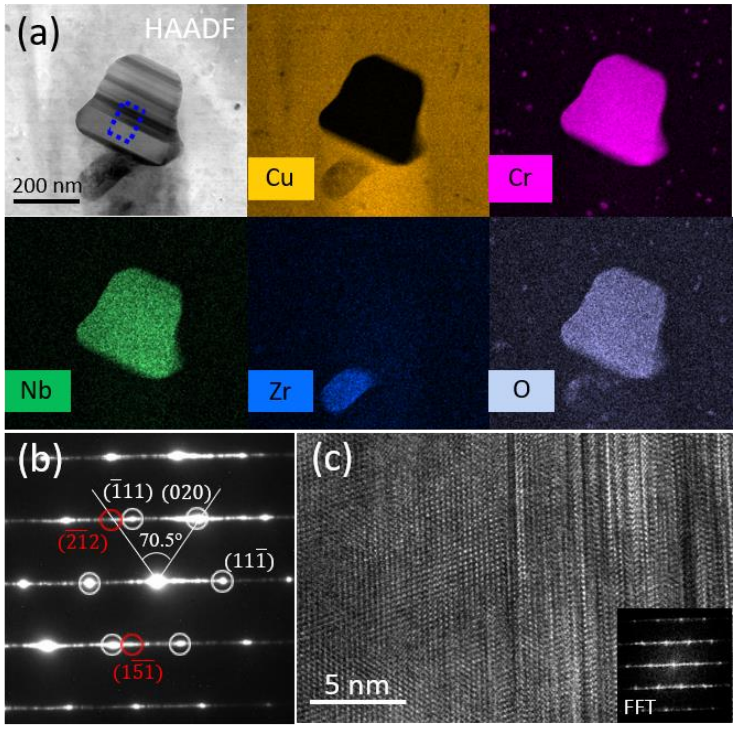


Figure 3-30: Continued. (a) HAADF image and elemental TEM-EDS mappings of Cu, Cr, Nb, Zr and O showing the laves phase Cr_2Nb precipitated in the matrix; (b) [110] SADP of the Laves_Cr_2Nb taken from dotted blue rectangle showing the C15-type cubic structure, and (c) the corresponding HRTEM image of Laves_Cr_2Nb.

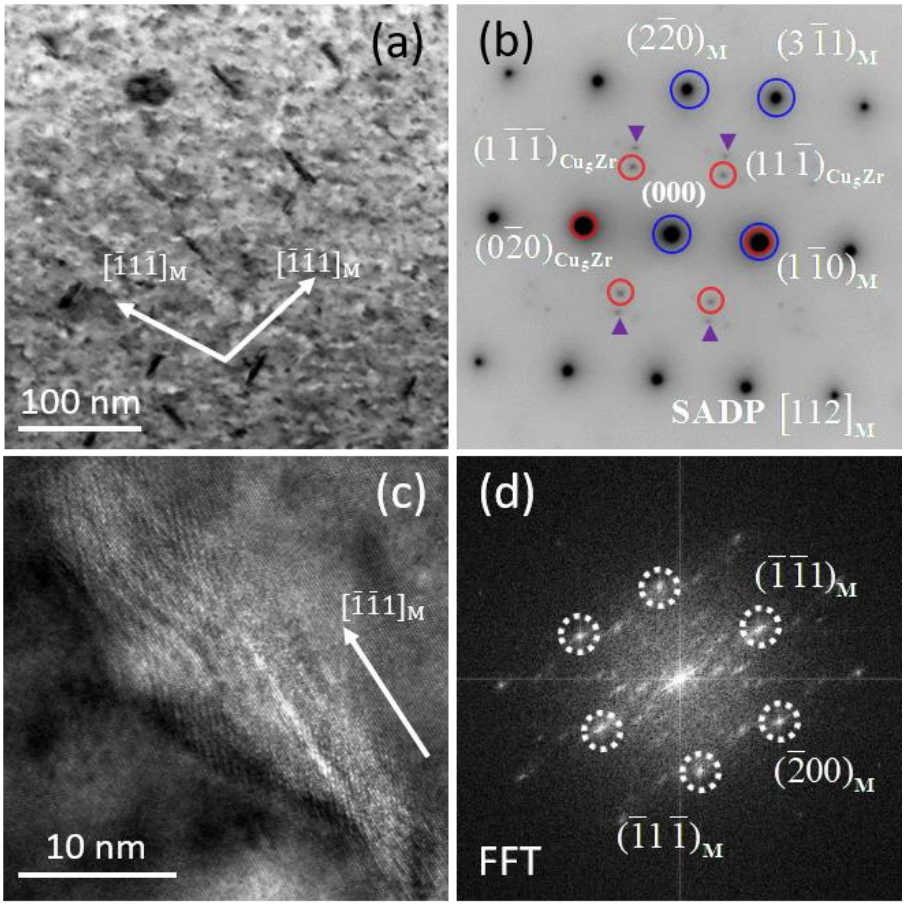


Figure 3-31: (a) STEM-BF image near the [110] Cu matrix zone axis with g=002, showing Cu_5Zr precipitates along two $\{111\}_{Matrix}$ planes [59]; (b) [112] matrix zone axis selected area diffraction pattern showing the precipitation orientation relationship of Cu_5Zr (red circles) with the Cu matrix. The superlattice reflections marked by purple arrows show the bcc Cr precipitates follow the N-W OR with the fcc Cu matrix; (c) and (d) high resolution TEM image of a Cu_5Zr precipitate along the <011> zone axis with the corresponding FFT pattern, indicating the precipitation habit plane is along $(\bar{1}\,\bar{1}1)$ of the Cu matrix.

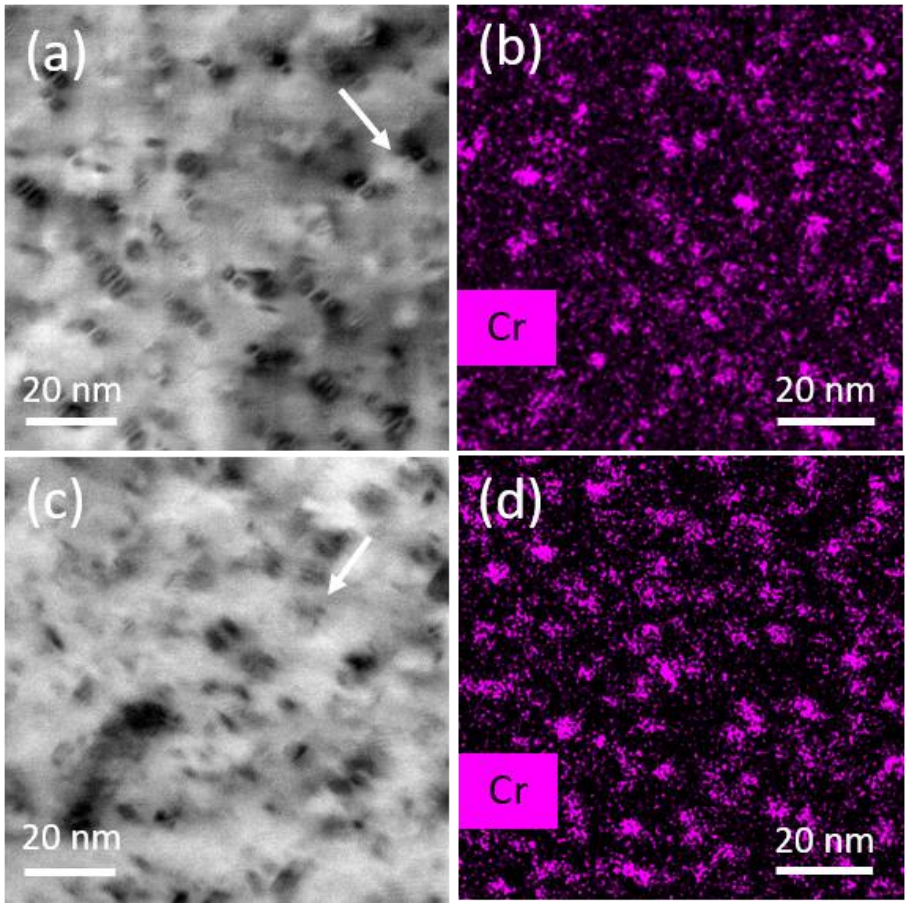


Figure 3-32: STEM-BF images and Cr EDS mapping of coherent Cr-rich precipitates in the (a, b) CuCrZr alloy and (c, d) CuCrNbZr_HP alloys in as-aged condition. The images in (a, c) were taken under dynamical diffraction conditions along the [011] zone axis using g=200 (diffraction vector direction shown by the white arrows).

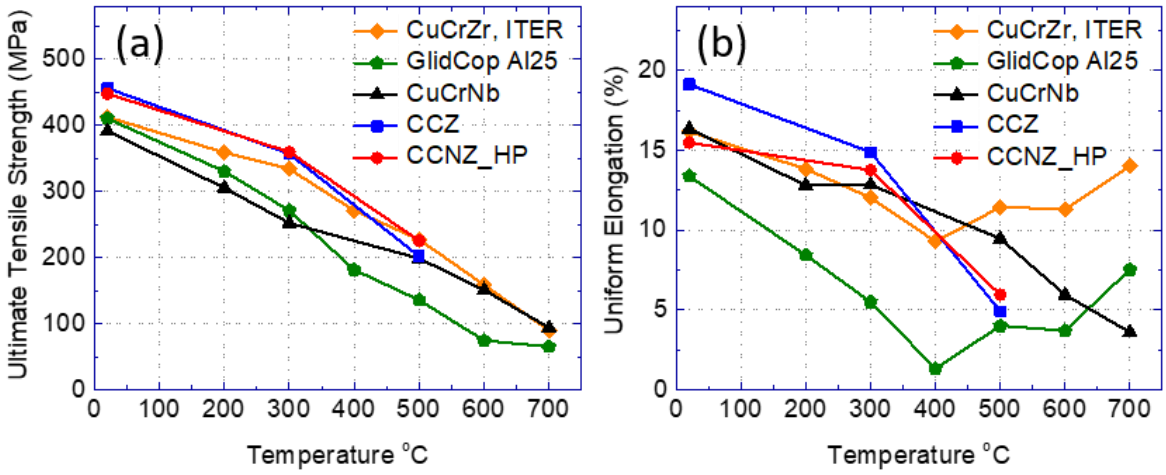


Figure 3-33: (a) Ultimate tensile strength versus temperature curves and (b) uniform elongation versus temperature curves for newly developed CuCrNbZr_HP alloys compared with existing commercial Cu alloy [68].

Table 3-4: 0.2% Yield strength on CuCrZr, and CuCrNbZr_HP alloys at 24, 300 and 500 °C.

Test Temperature (°C)	0.2% Yield Strength (MPa)	
	CuCrZr	CuCrNbZr_HP
24	347.5	342.0
300	293.7	288.2
500	192.4	212.4

To minimize the oxidation impact on a subsequent systematic study of creep strain rates at different stresses, follow-on creep tests on the CuCrZr and CuCrNbZr_HP alloys were conducted at 500 °C in flowing Ar gas with applied stress levels of 90, 100, 110, 125 and 140 MPa. The corresponding plots of creep strain versus time of both alloys are shown in Figure 3-35 (a) and (b), respectively. The creep life of the CuCrNbZr_HP alloy exceeded that of the CuCrZr alloy over all the applied stresses. The rupture strain for the CCNZ_HP alloy was similarly significantly higher (by about a factor of two) compared to the CuCrZr alloy for all test conditions. Linear curves were fitted for the applied stress vs. time to rupture data in Figure 3-35. The fitting for the CuCrZr alloy only included data from 90, 110 and 125 MPa applied stresses since the creep under 100 and 140 MPa (denoted by data points with an overlaid X in Figure 3-36; data points not plotted in later plots) resulted in premature failure as shown in Figure 3-35 (a)**.** The fitted curves for applied stress vs. rupture time of the CuCrZr and CuCrNbZr_HP alloys are nearly parallel to each other, indicating qualitative similarity of the two alloys, whereas from a quantitative perspective the CuCrNbZr_HP alloy had uniformly higher creep strength and longer creep life than the CuCrZr alloy for all test conditions at 500 °C. It is worth noting that instead of showing a prolonged steady state creep regime, the creep rates of both alloys continued to increase during all tests. This is probably due to the elevated test temperature (~0.6 T_m) [69]. Therefore, only the minimum creep strain rate values (obtained from polynomial fitting to the creep strain curves; Table 3-5) were used for further quantitative comparisons. The minimum creep rate vs. applied stress and rupture time for the CuCrZr and CuCrNbZr_HP alloys are shown in Figure 3-37 (a) and (b), respectively. The CuCrZr alloys exhibit lower (i.e., superior) minimum creep strain rates than the CuCrNbZr_HP alloys. A power-law equation can be used to obtain a simple estimation of the creep behavior of metallic alloys [70]:

$$\dot{\varepsilon} = A\sigma_a^m exp\left(\frac{-Q_c}{RT}\right), \qquad \text{(Eq. 3-1)}$$

where $\dot{\varepsilon}$ is the minimum creep rate (s^{-1}), A is a material constant (MPa^{-n}, s^{-1}), σ_a the applied stress (MPa), m the apparent stress exponent, Q_c the apparent activation energy for creep (kJ/mol), R the gas constant (8.314 kJ/mol-K) and T is the absolute temperature in K. The apparent stress exponents 8.7±0.9 and 6.6±1.3 were obtained from the slopes of the linear fitting for the CuCrZr and CuCrNbZr_HP alloys, respectively. Both alloys show that creep rate is inversely proportional to the time to rupture in Figure 3-37 (b).

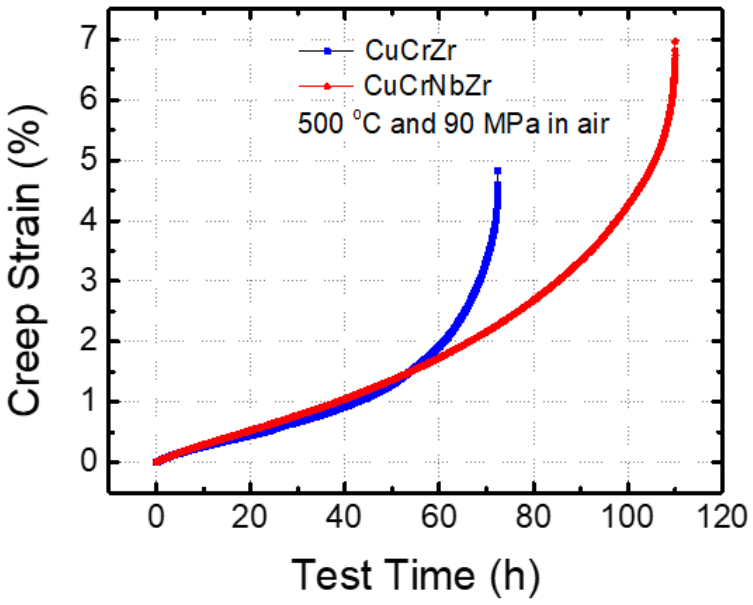


Figure 3-34: Plots of creep strain versus test time of CuCrZr and CuCrNbZr_HP alloys at 500 ºC and 90 MPa. The test environment was in air.

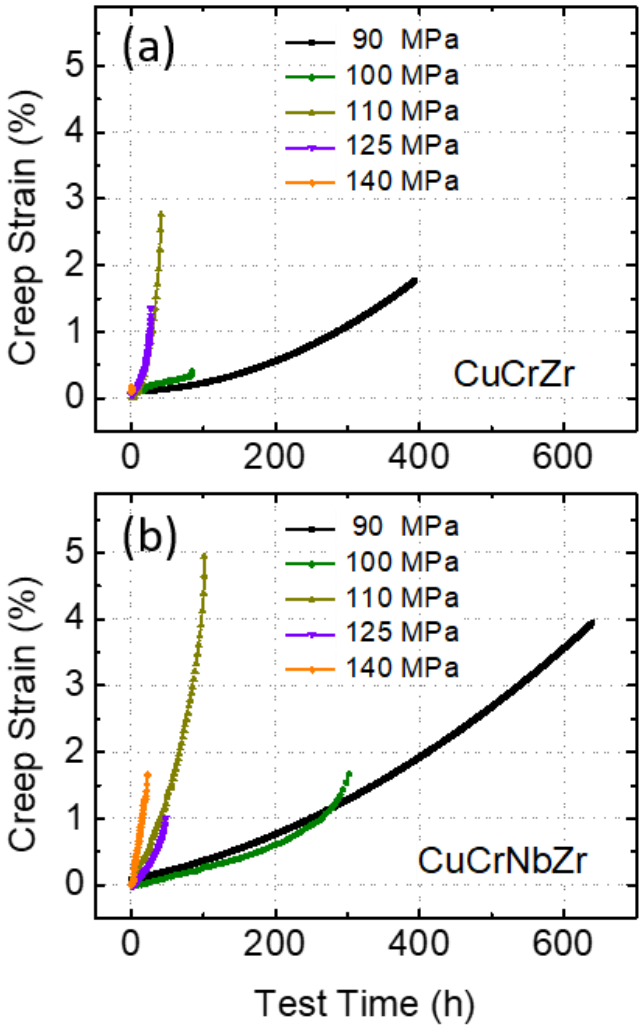


Figure 3-35: Plots of creep strain versus test time at 500 ºC for (a) CuCrZr and (b) CuCrNbZr_HP alloy under applied stresses of 90, 100, 110, 125 and 140 MPa.

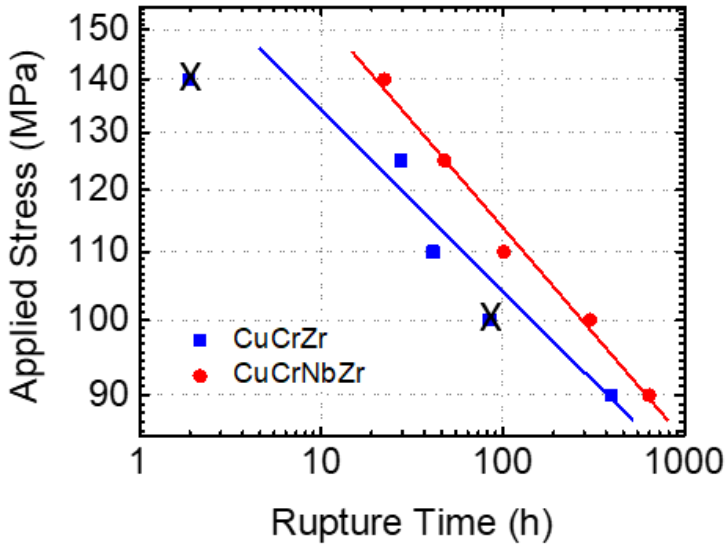


Figure 3-36: Applied stress versus rupture time.

Table 3-5: Minimum creep strain rates for CuCrZr and CuCrNbZr_HP alloys at 500 °C and 90, 100, 110, 125 and 140 MPa.

Applied Stress (MPa)	Strain rate $\dot{\varepsilon}_{min}$ (s^{-1})	
	CuCrZr	CuCrNbZr_HP
90	8.4×10^{-10}	6.1×10^{-9}
100	-	8.2×10^{-9}
110	3.8×10^{-9}	3.5×10^{-8}
125	1.5×10^{-8}	3.0×10^{-8}
140	-	1.3×10^{-7}

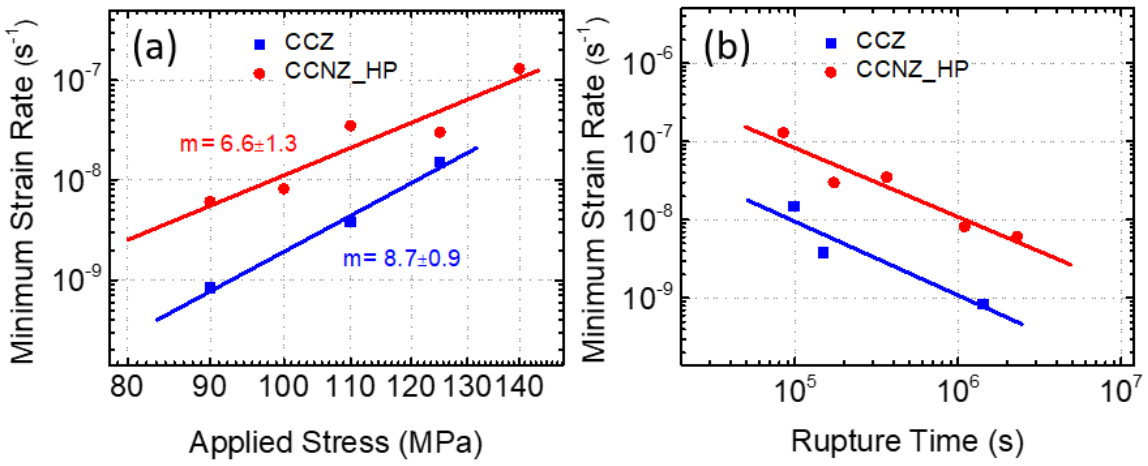


Figure 3-37: (a) Minimum creep rate versus applied stress for CuCrZr and CuCrNbZr_HP alloys on a double logarithmic scale; (b) minimum strain rate inversely proportional to rupture time on a double logarithmic scale.

3.4.7 Summary of CuCrNbZr precipitate characterization

In general, a new Cu based CuCrNbZr_HP alloy with a good combination of thermal conductivity, tensile strength, ductility and thermal creep resistance has been developed and fabricated through economic conventional ingot-metallurgy methods. Thermodynamic models for equilibrium phases in the CuCrNbZr_HP system have been used to aid the composition design and heat treatment parameter selection. The new alloy has been confirmed to have the desired multi-modal distribution of precipitates with coarse Laves phase at the grain boundary and fine Cr precipitates in the matrix to provide enhanced resistance to dislocation climb (power law creep) and diffusional creep (grain boundary sliding). The coarse Laves phase precipitates with typical size range of 2 to 11 μm are produced along the grain boundaries during solidification. The fine Cr precipitates with size of 5 nm are homogeneously distributed in the Cu matrix and form during final aging treatment at 475 °C. Both of the newly designed CuCrNbZr_HP and commercial CuCrZr alloys have sink strength of 2.6×10^{15} m^{-2}, contributing to high resistance to void swelling. Also, both of the Cr precipitates in two alloys show normal diffusion response to thermal creep annealing at 500 °C for ~100 h, indicating the addition of Nb does not significantly change the Cr diffusion kinetics in the CuCrNbZr_HP alloys. The high density of fine-scale Cr precipitates, forming coherent interfaces with the Cu matrix, are the predominant contributor to the tensile strength, and the coarse-scale Laves phase precipitates play the key role in enhancing thermal creep resistance in CuCrNbZr_HP alloys.

CHAPTER 4

DISCUSSION

4.1 Dilute Cu alloys

4.1.1 Sink strength effect on coherency loss of precipitates in irradiated regions

Both the in situ irradiation (1 MeV Kr^{++} ions) and ex situ (1 MeV Ni^{+} ions) irradiation experiments have been conducted at RT, high temperature (200 and 340 ^{o}C for in situ, 350 ^{o}C for ex situ) and low temperature (-223 ^{o}C for in situ, -117 ^{o}C for ex situ). It is found that at RT and high temperature irradiation experiments, higher sink strength alloys show higher resistance to coherency loss, which means higher threshold damage dose need to cause precipitates lose coherency. CC1 alloys with the sink strength of 1.3×10^{14} m^{-2}, have been irradiated up to 1 dpa at RT with 1 MeV Kr^{++} ion. No coherency loss was observed after the 500 ^{o}C post-irradiation annealing experiments, which is consistent with the results for irradiation to 1 dpa at RT and 350 ^{o}C with 1 MeV Ni^{+} ion. Actually, the predicted threshold damage dose is even higher than 10 dpa based on the 10 dpa irradiated results also conducted at RT and 350 ^{o}C. CC2 alloys have lower sink strength (5.3×10^{13} m^{-2}) compared to CC1 alloys. It is shown that Co precipitates lose coherency when irradiated up to 1.25 dpa at 340 ^{o}C with 1 MeV Kr^{++} ions and 1 and 10 dpa at 350 ^{o}C with 1 MeV Ni^{+} ions. Figure 4-1 shows microstructures of the Co precipitates in CC1 and CC2 alloys irradiated with 1 MeV Kr^{++} ions. The threshold damage dose for CC2 alloys is predicted to be between 0.25 and 1 dpa as shown in Figure 4-1, precipitates became semi-coherent when irradiated to 0.25 dpa at 340 ^{o}C. Figure 4-2 shows the precipitates in CC1 and CC2 alloys kept coherency when the damage doses are 0.0125 and 0.0625 dpa. Both of the precipitate structures in these two alloys are stable with increasing damage dose up to 0.0625 dpa. This may account for the low density of radiation defects at the early irradiation periods. The threshold damage dose for CC3 (3.0×10^{13} m^{-2}) alloy is predicted to be lower than 0.0625 dpa. For CC4 (3.0×10^{13} m^{-2}) alloys, precipitates were stable when irradiated up to 0.0125 dpa. However, some of the precipitates were semi-coherent due to their large size, so there's no conclusion on the threshold damage dose for this alloy. Fe precipitates in CFZ-0 (4.0×10^{14} m^{-2}) and CFZ alloys (7.3×10^{13} m^{-2}) show stronger resistance to coherency loss than CC2 alloys. The threshold damage dose of CFZ-0 alloy is above

10 dpa according to the experimental results, while due to the limited experimental results from CFZ alloy, the threshold damage dose for this alloy is predicted to be aboe 0.625 dpa.

1 MeV Kr^{++} ion irradiation is generally applied to mimic the neutron irradiation due to the close particle mass. According to SRIM predicted damage ranges in Figure 2-6 (450 nm for 1 MeV Kr^{++} ions) and Figure 2-7 (600 nm for 1 MeV Ni^{+} ions), both of the irradiation experiments can observe the precipitate structure within the irradiated regions, though there's concern regarding the implantation of Kr^{++} ions into the TEM thin foils that introduce bubbles during in situ irradiation. The thin foil regions during characterization in this research were all below 200 nm in thickness which is shallower than the penetration depth of 1 MeV Kr^{++} ions. The same ion energy and similar mass of the 1 MeV Kr^{++} ion irradiation and 1 MeV Ni^{+} ion irradiation can be basically assumed the same heavy ion irradiation.

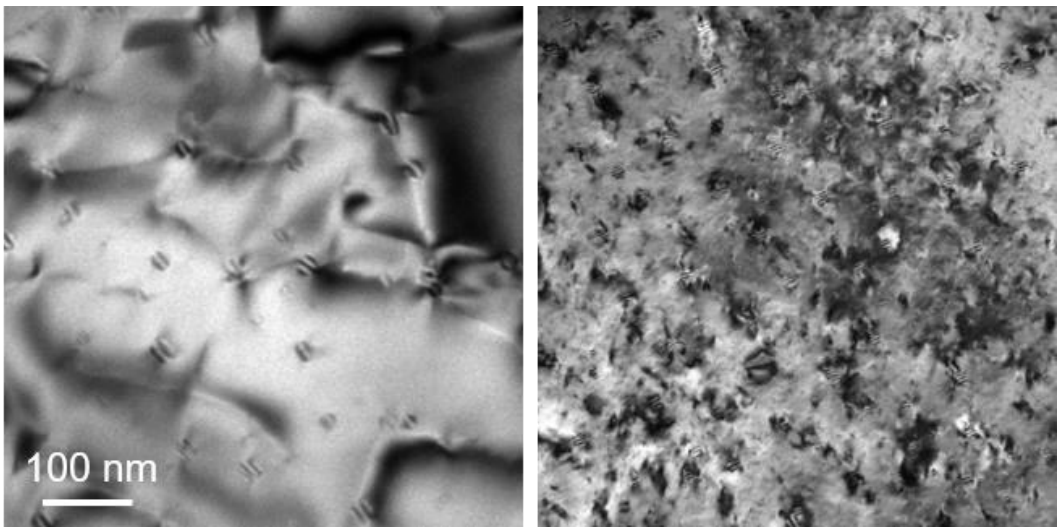


Figure 4-1: TEM-BF images of CC1 alloy irradiated to 1 dpa at RT then post-irradiation annealed at 500 ^{o}C (left) and CC2 alloy irradiated to 0.25 dpa at 340 ^{o}C (right) with 1 MeV Kr^{++} ions.

4.1.2 Comparison of observed 1D migration of SIAs clusters with MD simulations

Table 4-1 compares the observed BEOR (beyond end of region) loss of coherency with computational predictions by using the pure 3D and 1D equation from Ref. [22]. At 350 ℃ (above recovery "stage V" temperature in Cu), vacancy clusters are thermally unstable and can release vacancies to the matrix, while the diffusivity of SIAs is much higher than vacancies, resulting in initial coherent precipitates in these Cu alloys acting as majority sinks with the sink strength calculated through $2\pi Nd$ [22]. However, at 25 ℃ (above recovery "stage III" temperature), thermally stable vacancy-type stacking fault tetrahedra (SFT) along with dislocation loops and network dislocations play the key role of defect sinks in irradiated regions. The values of overall sink strength for irradiation at 25 ℃ are about 200 times higher than for 350 ℃ ion irradiation based on data collected from Ref. [71], causing fewer surviving defects (more recombination within the ion irradiated region) to escape into the BEOR. The observed extent of the loss of coherency regimes of CC2 alloys are consistent with 1D defect cluster motion, since at 350 ℃ (~1700 nm for 12 dpa and 800 nm for 1.2 dpa) and 25 ℃ (~550 nm for 12 dpa) both BEOR are close to their calculated pure 1D motion mean free paths, and significantly larger than calculated 3D motion mean free paths, indicating that most of the radiation-produced clusters exhibit 1D motion. No coherency loss of precipitates in the BEOR was observed at 0.1 dpa for CC2 alloy at either of the temperatures, indicating there's no significant fraction of mobile surviving defect clusters beyond the ion irradiated regions. Also, no observation of BEOR loss of coherency for sample CC1 and CFZ-0 occurred at any ion irradiation conditions, indicating the depth dependence of precipitate loss of coherency is related to initial precipitate sink strength. When the precipitate sink strength is over 10^{14} m^{-2}, the initial coherent interfaces are resistant to the migrating defect clusters and keep stable to certain irradiation conditions.

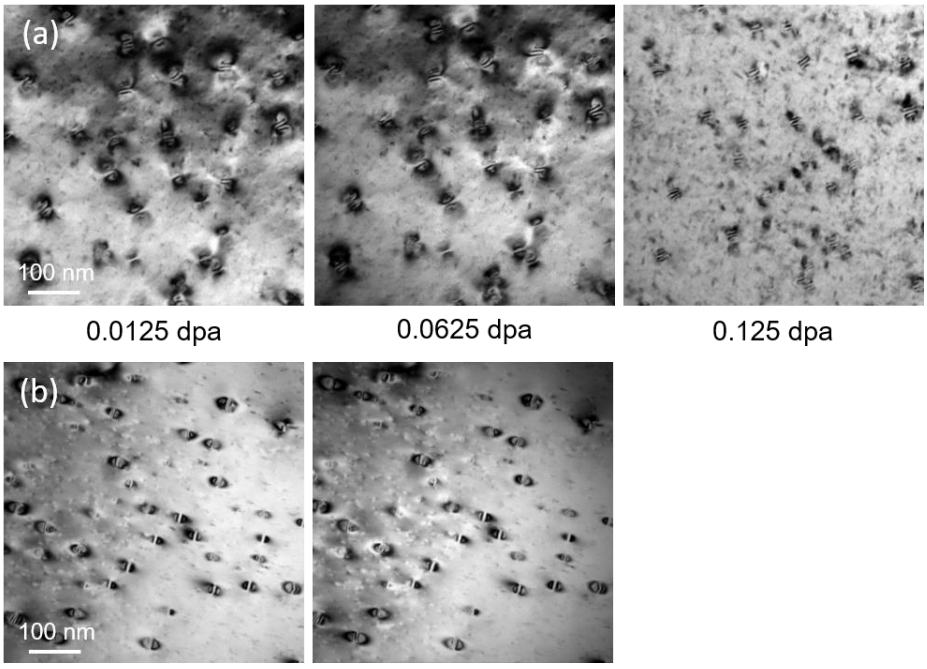


Figure 4-2: TEM-BF images of (a) CC1 and (b) CC2 alloys irradiated at 340 ^{o}C with 1 MeV Kr^{++} ions.

Table 4-1: Calculation results by 1D vs. 3D migration of SIA clusters on microstructural evolution and comparison to observed precipitate loss of coherency BEOR.

Alloys	Majority sink mean size (nm)	Majority sink density (m^{-3})	Majority sink strength ~4πNR (m^{-2})	3D motion $\boldsymbol{\lambda}\sim(4\boldsymbol{\pi}rN)^{-1/2}$ (nm)	1D motion $\boldsymbol{\lambda}\sim(6\boldsymbol{\pi}^2r^4N^2)^{-1/2}$ (nm)	Observed BEOR loss of coherency (nm)
CC2 (350 ℃)	19.6±3.6	4.3×10^{20}	5.3×10^{13}	137	3148	~1700 (12 dpa) ~800 (1.2 dpa)
CC2 (25 ℃)	2	9×10^{22}	1.1×10^{15}	30	1444	~550 (12 dpa) None
CC1	11.5±3.2	1.7×10^{21}	1.3×10^{14}	90	578	None
CFZ-0	12	4.3×10^{21}	3.3×10^{14}	55	839	None

Note that, the fluences for the peak damage of 1.2 and 12 dpa are 7×10^{14} and 7×10^{15} ions/cm^2, respectively.

4.1.3 The effect of Cu SIA clusters on the coherency of a Co precipitate

In order to further analyze the sink strength effect on the coherency loss of precipitates and interpreter the interactions between interstitial clusters and coherent precipitates, five MD simulation systems were setup and performed using LAMMPS by D. Martin, UTK [72]. The interactions between Cu atoms are described by an Embedded Atom Method (EAM) potential by Foiles et al. [73] and interactions between Co atoms are described by an EAM potential by Pasianot et al. [74]. The Cu-Co pair potential was developed by Nordlund and Averback [75]. This pair potential was developed to give correct heat of mixing for Co impurities in Cu at low Co concentrations and correct lattice parameter changes. These potentials were chosen for their ability to describe Co-Cu interactions and their fit to experimental data. Table 4-2 lists the precipitate mean size, number, density and sink strength of five MD simulation systems including a reference system without precipitates. Simulation cells with the volume of 72×72×72 nm^3 (approximately 32 million atoms) were used. Temperature controlled by Nose-Hoover thermostat to 227 ^oC (500 K) or 727 ^oC (1000 K). SIA inserted to a concentration of 2.7×10^{19} cm^{-3} (~10,000). Co precipitates are randomly distributed in the system with different number or size diameter to meet the different sink strength compared to experimental system.

(a) The growth of interstitial clusters in pure Cu and Cu with Co precipitates

All simulations show SIA clustering over time and most of the clusters form ½<110>{110} perfect loops. Figure 4-3 shows SIA clustering status at 727 ^oC, 2 ns. Simulations at 1000 K show larger clusters and a "flatter" distribution compared to 227 ^oC (Figure 4-4). While, there's no dependence of sink strength on cluster distribution, it seems that higher sink strength (~2×10^{14} m^{-2}) leads to higher accumulation of SIA clusters at the precipitate interface (Figure 4-5).

Table 4-2: MD simulation systems setup.

Systems	Precipitate mean size (nm)	Precipitate Number	Precipitate density (m^{-3})	Sink strength (m^{-2})
#1(0 at.% Co)	-	-	-	0
#2 (0.017 at.% Co)	5	1	2.58×10^{21}	8.4×10^{13}
#3 (0.5 at.% Co)	15	1	2.58×10^{21}	2.5×10^{14}
#4 (0.017 at.% Co)	5	8	2.01×10^{22}	6.7×10^{14}
#5 (0.5 at.% Co)	15	8	7.0×10^{21}	6.8×10^{14}

Note: the box volume of #5 is smaller than #1~4 in order to make the sink strength comparable to #4.

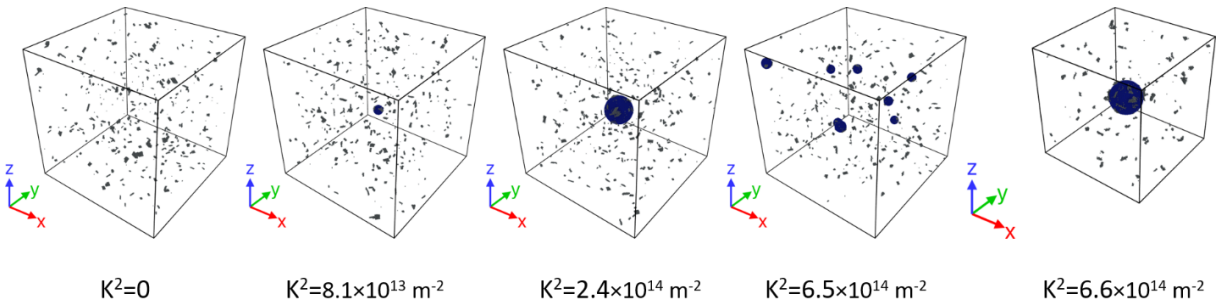


Figure 4-3: MD simulations results at 727 °C, 2 ns.

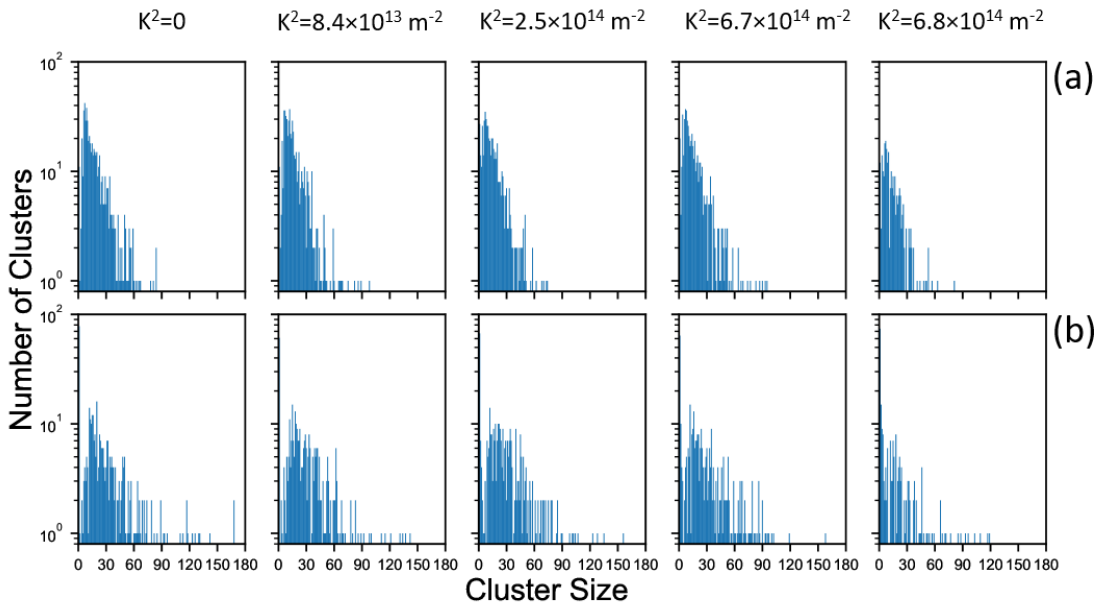


Figure 4-4: Cluster size distribution at 5 ns for (a) 227 °C and (b) 727 °C.

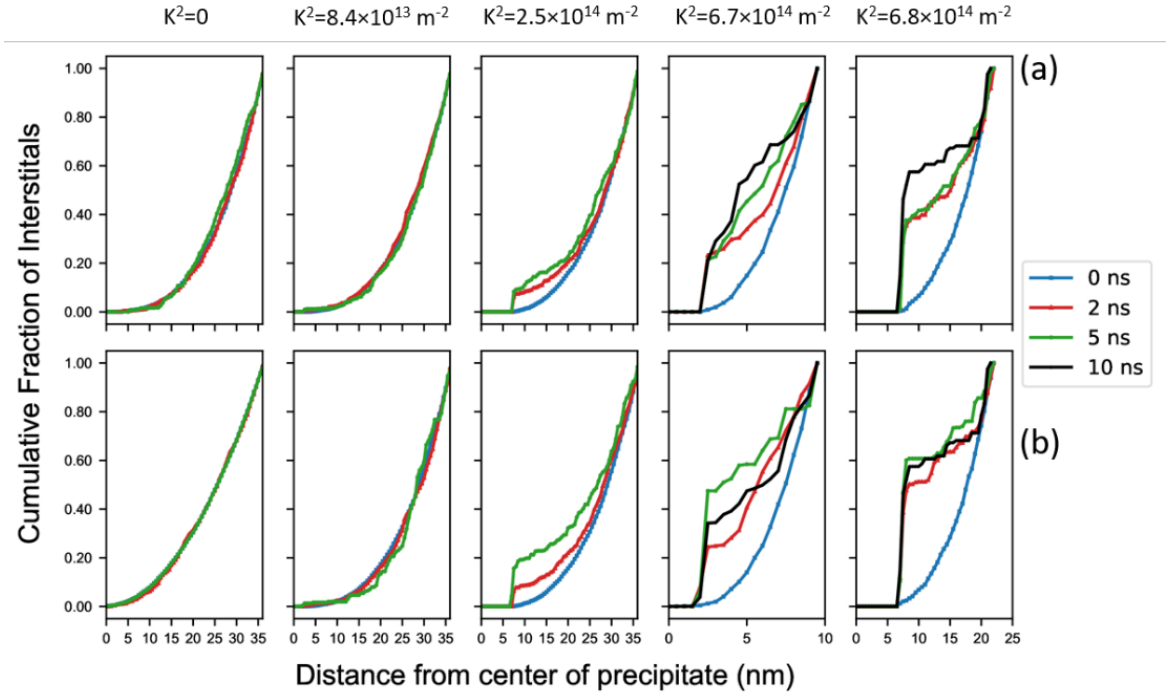


Figure 4-5: Cumulative fraction of interstitial versus distance from center of precipitate at (a) 227 °C and (b) 727 °C.

(b) The stress field induced by the insertion of a Co-precipitate

Figure 4-6 shows a [100] view of 4 nm slab presenting the interaction of Cu SIA clusters with the precipitate (MD simulation performed by David Martin, UTK graduate student). The induced strain from Cu SIA/Co-precipitate interaction becomes visible and appears to be mostly limited to the surface. At 5 ns, the Common Neighbor Analysis shows precipitate maintains FCC structure. While the low sink strength 5 nm-diameter precipitate shows very little interaction with Cu SIA clusters, the high sink strength precipitate has begun to show some loss of coherency shown in Figure 4-7.

(c) The effect of precipitate on migration path

A 24-interstitial cluster with the direction of ½{110} was chose to interact with a 15 nm-diameter precipitate at 727 ^{o}C at ~12 nm from the surface (MD simulation performed by D. Martin, UTK). Three separate glide paths were given: center of precipitate, edge of precipitate and just outside of the precipitate edge. The results show that the precipitate gives preference for glide direction depending on cluster orientation:

(1) The cluster pointed directly at the precipitate glided right into precipitate and became trapped within 150 ps.
(2) The clusters pointed at the edge of the precipitate have not shown a preference in glide direction and are still near starting point at 150 ps.
(3) The glide path has not been altered for any interstitial cluster

Figure 4-8 shows the deformation caused by the interaction between Cu SIA clusters and a 15 nm-diameter Co-precipitate from perspective side view of Co-precipitate/Cu matrix interface at 727 ^{o}C.

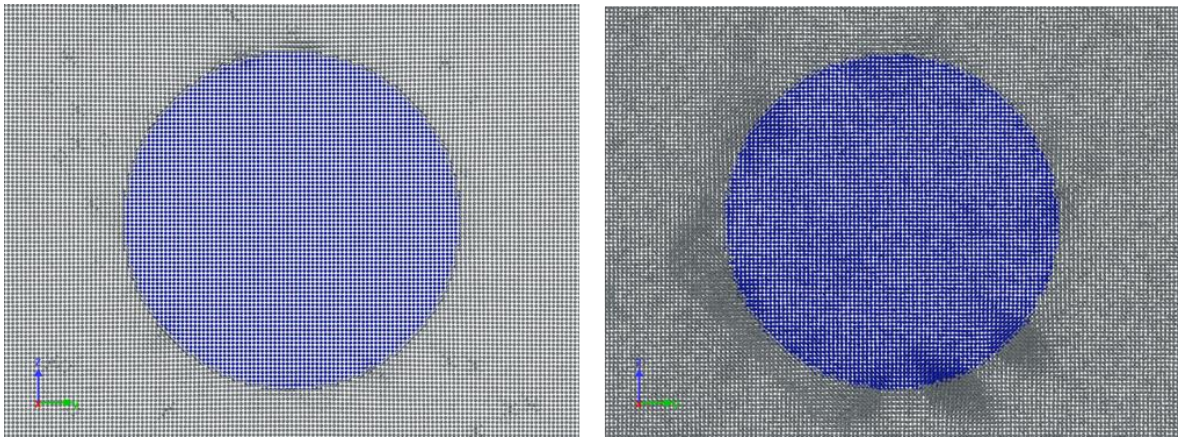


Figure 4-6: A 15 nm-diameter Co precipitate with the sink strength of 6.8×10^{14} m^{-2} at 727 ^{o}C at 0 ns (left) and 5 ns (right).

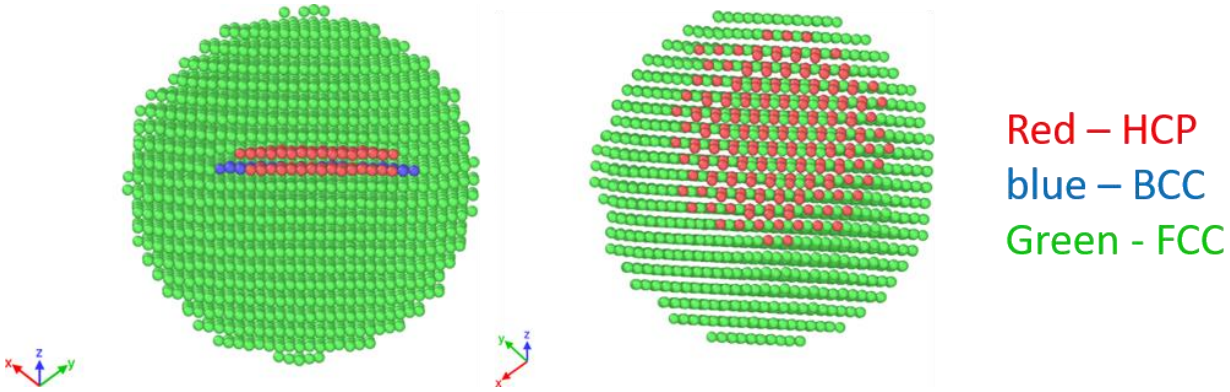


Figure 4-7: Perspective view of 2 separate 5 nm-diameter precipitates at 727 ^{o}C with a sink strength of 6.7×10^{14} m^{-2}.

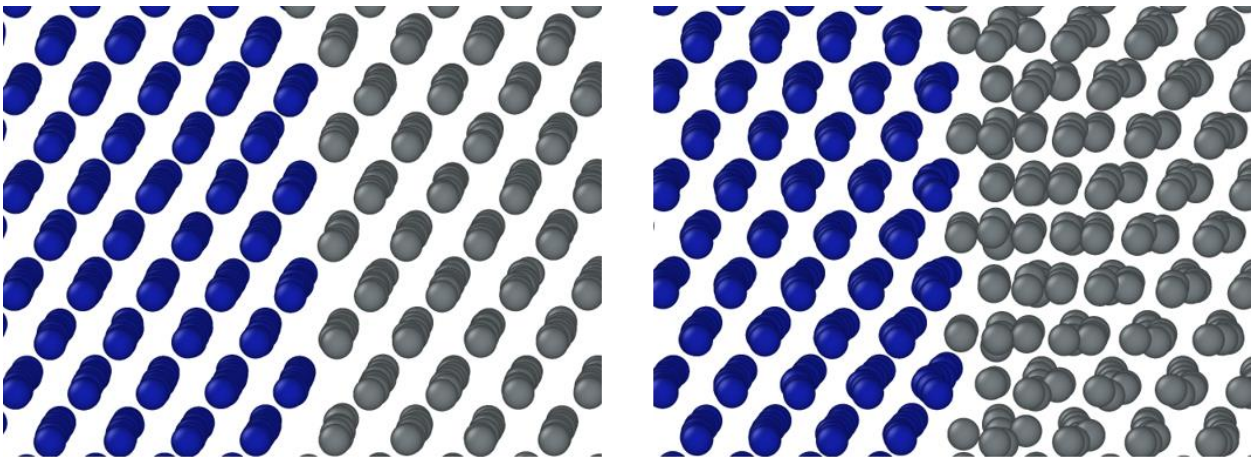


Figure 4-8: Perspective side view of a 15 nm-dimeter Co precipitate/Cu matrix interface simulated at 727 ^{o}C with 24 interstitial clusters at 0 ps (left) and 15 ps (right). Co precipitate in blue and Cu matrix in grey.

4.1.4 Quantification of vacancy defects during ion irradiations

Vacancy defects densities were calculated in two annealing conditions, Figure 4-9 shows the CC1 alloys annealed at 200 and 340 ^{o}C before irradiation and with the increasing damage dose, more vacancy defects produced and reached their peak when the damage dose is about 0.08 dpa based on the fitting plots. The higher density value of vacancy defects at 200 ^{o}C may account for their lower mobility compared with 340 ^{o}C. Figure 4-10 shows a CFZ alloy initially irradiated at RT and post-irradiation annealed to higher temperatures of 200, 400 and 500 ^{o}C with decreasing defect cluster density. The difference between RT and 500 ^{o}C might be more than 10 times.

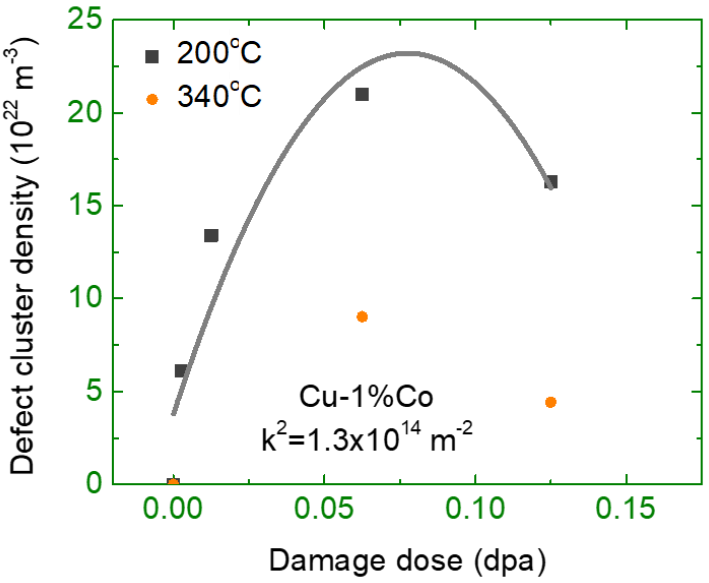


Figure 4-9: Defect cluster density of CC1 alloys irradiated at 200 and 340 °C with 1 MeV Kr^{++} ions up to 0.125 dpa.

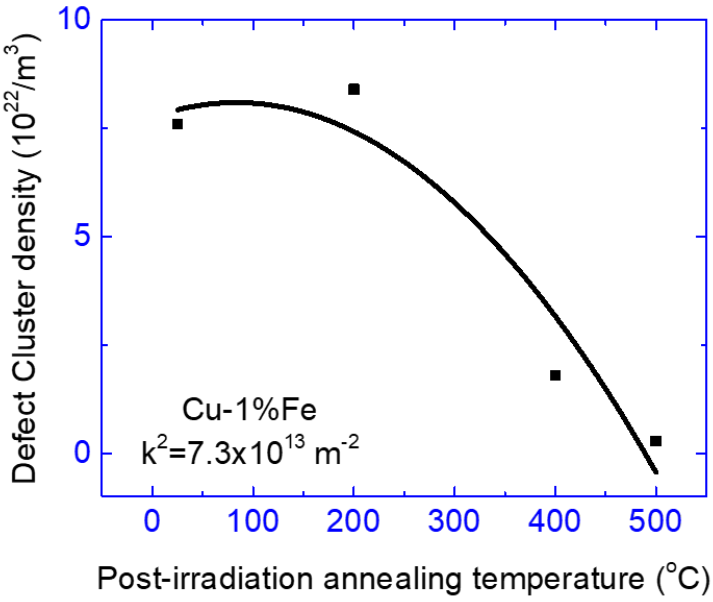


Figure 4-10: Defect cluster density of CFZ alloy initially irradiated at RT with 1 MeV Kr^{++} ions up to 0.625 dpa then post-irradiation annealed to temperatures of 300, 400 and 500 °C.

4.2 CuCrNbZr alloys

4.2.1 Threshold stress analysis and creep mechanism in CuCrZr and CuCrNbZr alloys

For the precipitation hardened alloys, a relatively high stress exponent (n≥5) for creep has generally been reported from a simple application of Eq. (4-1) [76]. The high stress exponents obtained from equation (1) can be rationalized by considering that there is a threshold stress (σ_{th}) below which dislocation creep doesn't occur [77]. The minimum creep strain rate is then described by

$$\dot{\varepsilon} = A(\sigma_{eff})^n exp\left(\frac{-Q_c}{RT}\right) \quad \text{(Eq. 4-1)}$$

where the effective stress $\sigma_{eff}=\sigma_a-\sigma_{th}$, and n is the true stress exponent.

For all possible creep mechanisms n can range from 1 to 7 [78]. Different n values correspond to different creep mechanisms, such as Nabarro-Herring creep, Coble creep, grain boundary sliding, dislocation viscous glide and dislocation climbing, respectively. By plotting the creep rate parameter $\dot{\varepsilon}^{(1/n)}$ vs. applied stress, σ_a, the intercept with the stress axis at zero creep rate is defined as threshold stress, σ_{th}. To estimate the rate controlling creep mechanisms, the choice of true stress exponent value must satisfy the best correlation coefficient of the linear fitting as well as the corresponding activation energy. However, the activation energy cannot be estimated here since the tests were done at one temperature (500 ^{o}C) only. Therefore, the stress component for each assumed "n" value was obtained as the slope of linear fitting curves in creep rate versus effective stress.

Based on the best match between the assumed stress exponent and obtained stress exponent from Table 4-3, grain boundary sliding (n=2) is the most likely dominant creep mechanism for both the CuCrZr (n=1.6±0.4) and CuCrNbZr_HP (n=1.7±0.4) alloys at 500 ℃ for applied stress levels of 90~140 MPa. The corresponding threshold stresses were 82 and 79 MPa, respectively. Figure 4-11 (a) shows the plots of $\dot{\varepsilon}^{\wedge(1/2)}$ versus σ_a for the CuCrZr and CuCrNbZr_HP alloys (i.e., assuming the stress exponent is 2). The minimum creep strain rates as a function of the effective stress on a double logarithmic scale at 500 ℃ for n=2 are shown in Figure 4-11 (b).

Table 4-3: Threshold stress analysis for CuCrZr and CuCrNbZr_HP alloys.

Assumed stress exponent	n=1		n=2		n =3		n =4		n =5		n=6		n=7	
Alloy	CCZ	CCNZ	CCZ	CCNZ	CCZ	CCNZ	CCZ	CCNZ	CCZ	CCNZ	CCZ	CCNZ	CCZ	CCNZ
Threshold Stress (MPa)	66	90	82	79	81	71	83	67	83	64	80	58	83	60
Correlation coefficient (%)	68.7	67.4	87.3	79.9	92.3	83.1	95.0	84.3	96.2	84.9	96.9	85.2	97.4	85.4
Obtained Stress exponent	3.5± 2.8	1.5± 0.5	1.6± 0.4	1.7± 0.4	1.7± 0.4	2.3± 0.5	1.5± 0.4	2.5± 0.6	1.5± 0.4	2.7± 0.6	1.8± 0.4	3.1± 0.7	1.5± 0.4	3.0± 0.6
Correlation Coefficient (%)	35.9	75.7	87.9	79.7	88.7	82.6	87.0	83.3	87	83.7	89.4	84.3	87.0	84.1

Note, the resultant matrix of the threshold stress analysis using the linear extrapolation method for all possible values of exponent at 500 ^{o}C is listed in Table 4-3. It includes the assumed n-values, thresholds, correlation coefficients, and obtained actual n-values.

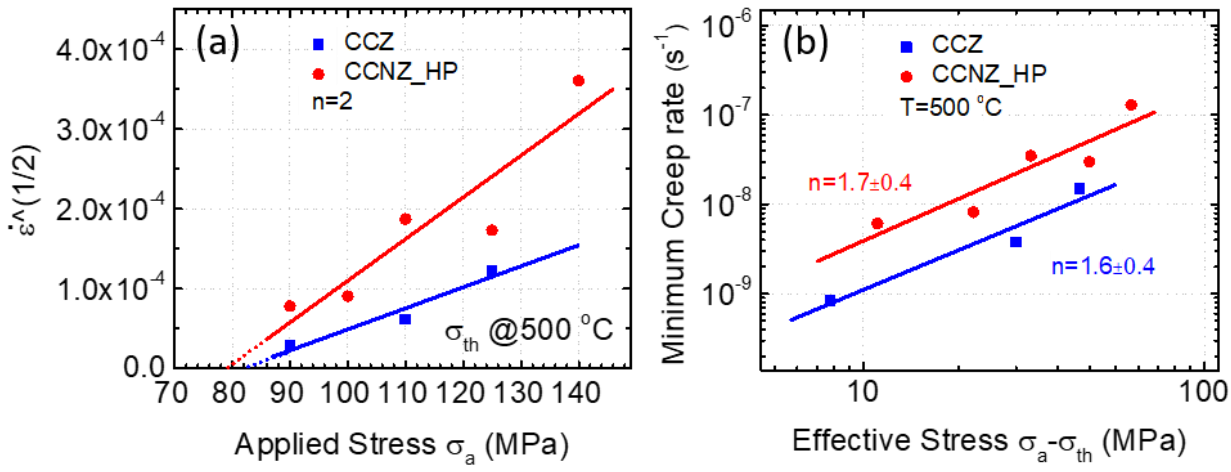


Figure 4-11: (a) Threshold stress calculation using linear extrapolation method for n=2, and (b) minimum strain rate versus effective stress at 500 ºC.

Table 4-4: Calculated miminum grain boundary strain rate for CuCrZr and CuCrNbZr_HP alloys at 500 ºC and applied stresses of 90, 100, 110, 125 and 140 MPa.

Applied Stress (MPa)	Strain rate $\dot{\varepsilon}_{min}$ (s^{-1})	
	CuCrZr	CuCrNbZr_HP
90	4.9×10^{-10}	5.2×10^{-9}
100	-	1.9×10^{-8}
110	6.0×10^{-9}	4.1×10^{-8}
125	1.4×10^{-10}	9.1×10^{-8}
140	-	1.6×10^{-7}

With the grain boundary sliding mechanism, the theoretical steady state strain rate could be calculated from the model by Ruano and Sherby [79]

$$\dot{\varepsilon}_{gbs} = 10^8 \frac{D_{gb} b}{\overline{L}^3} \left(\frac{\sigma_a - \sigma_{th}}{E}\right)^2 \quad \text{(Eq. 4-2)}$$

where D_{gb} is the grain boundary diffusivity (cm^2/s), $\boldsymbol{b}$ the Burgers vector (nm), $\overline{L}$ the mean linear intercept grain size (μm) and E the modulus of elasticity (GPa). The grain boundary diffusivity is given by $D_{gb} = D_{0gb}\, exp\left(\frac{-Q}{RT}\right)$ where D_{0gb} is grain boundary diffusion coefficient (cm^2/s), taken to be ~2 cm^2/s within the range reported for fcc metals by Gibbs and Harris [80], Q the grain boundary diffusion activation energy (133.9 kJ/mol) [81], R the universal gas constant (8.314 J/mol-K), T the absolute temperature in K. The value for b was taken to be 0.256 nm for dislocations in the fcc Cu matrix, and the modulus of elasticity E=100 GPa was estimated for Cu alloys at 500 ºC [82].

The calculated theoretical grain boundary creep strain rates are between the values of 4.9×10^{-10} s^{-1} (90 MPa) and 1.4×10^{-8} s^{-1} (125 MPa) for CuCrZr, and 5.2×10^{-9} s^{-1} (90 MPa) to 1.6×10^{-7} s^{-1} (140 MPa) for CuCrNbZr_HP (details are listed in Table 4-4), which are comparable to their experimental minimum strain rates in Figure 3-37 (a) and Table 3-5, consistent with the assumption of the prominent creep mechanisms of the two Cu alloys as grain boundary sliding. Plots of grain size-normalized minimum creep rate versus effective stress of CuCrZr and CuCrNbZr_HP alloys are shown in Figure 4-12. The linear fitted line of grain size-normalized creep rates in CuCrNbZr_HP alloys overlapped with original fitted line of CuCrZr alloys (Figure 4-11 b) when creep data for the CuCrNbZr_HP were normalized by cube of mean grain size of CuCrNbZr_HP (22 μm) over CuCrZr alloy (39 μm), providing support that grain boundary sliding is the main creep mechanism for these test conditions.

4.2.2 Roles of Laves phase on the creep property of the CuCrNbZr_HP alloy

Based on the results above, grain boundary sliding is dominant creep mechanism in both CuCrZr, and CuCrNbZr_HP alloys. It is well known that grain boundaries are a potential source of weakness at high temperatures because they provide both nucleation sites for cavities and paths for the interlinkage of cavities to form intergranular cracks. During creep, shear stresses will force

the grains to slide against each other, i.e., the so-called “grain boundary sliding” as a bulk movement of two grains. It is one of the deformation mechanisms of materials at elevated temperature and low strain rate.

While the creep of both the CuCrZr and CuCrNbZr_HP alloys are dominated by grain boundary sliding mechanism, the CuCrNbZr_HP alloy shows higher creep strength and longer creep life (higher creep fracture strain) than the CuCrZr alloy for all tested conditions. It is intriguing to see the enhanced creep life in the CuCrNbZr_HP alloy even though its minimum creep strain rate is also higher. The higher value of the minimum creep strain rate can be attributed to the finer grain size of the CuCrNbZr_HP alloy, as demonstrated in the grain size compensated creep rate Figure 4-12 The enhanced creep life behavior and higher creep fracture strain for the CuCrNbZr_HP alloy may be associated with the presence of Laves phase precipitates. It is well known [83] that grain boundaries are a potential source of weakness at high temperatures because they provide both nucleation sites for cavities and paths for the interlinkage of cavities to form intergranular cracks. Two low magnification SEM images, Figure 4-13 (a) and (b), show the ductile fracture behaviors of the CuCrZr and CuCrNbZr_HP alloys at 500 ℃ and 90 MPa. The dotted blue rectangle regions were magnified in Figure 4-13 (c) and (d), respectively. It is apparently that the larger cracks (indicated by yellow arrows) developed at grain boundaries without Laves phases, and much smaller cracks occurred at grain boundaries covered by Laves phase (indicated by red arrows). This suggests the coarse Laves phase is effective in blunting crack tips and suppressing crack propagation, thereby increasing the creep strength, overall creep fracture strain, and creep life. Figure 4-14 shows a STEM-BF image with a Laves precipitate across the grains, leaving the dislocations pile up at the interface between Laves phase and grain boundaries. On the other hand, Laves phase precipitates are also very effective to inhibit grain growth during high temperature annealing (such as the solution anneal treatment at 970 ℃). The non-uniform distribution of Laves phase precipitates at grain boundaries that formed during solidification apparently led to non-uniform grain size in the CuCrNbZr_HP microstructure. As shown in the optical images of the unstressed end tab sections of the samples after creep tests (Figure 4-15**)**, the grains associated with the Laves precipitates remain small in all testing conditions, while the grains (labelled by “C”) far away from the Laves precipitates (indicated by red arrows) show much larger size. The regions clustered with small grains have a higher tendency for crack initiation, therefore causing a higher minimum creep rate. The non-uniform distribution

of Laves phase left a large fraction of grain boundaries uncovered by precipitates, which made the material less effective to resist grain boundary sliding.

4.2.3 Precipitate stability after creep

Figure 4-16 includes a STEM-HAADF image and three individual elemental maps of Cu, Cr and Zr in CuCrZr alloy after creep test at 500 ^{o}C and applied stress of 90 MPa in air. The TEM sample was lift-out from a stressed gauge area containing a grain boundary in the view, however no apparent grain boundary deformation was observed. The matrix Cr precipitates coarsened after 72 h creep test, the precipitate shape changed from spherical to oval-shape, with decreased number density. The observed denuded zone is about 300 nm.

Figure 4-17 shows a STEM-HAADF image and individual composition maps of Cu, Cr, Nb and Zr and a two-elemental-composition map of Cr and Zr in CuCrNbZr_HP alloy after creep at 500 ^{o}C and 90 MPa in air. The TEM sample was lifted out from a stressed gauge without Laves phase due to no enrichment of Nb appeared. The matrix Cr precipitates seemed coarsen a lot after creep test time of 110 h, their morphology changed to stick shape and resulted in lower number density.

Figure 4-18 shows two high magnification Cr elemental mappings for CuCrZr and CuCrNbZr alloys both crept at 500 ^{o}C and 90 MPa in air with different creep rupture times (72h vs. 110 h). The average longitude sizes are 12.5±2.4 nm and 29.4±7.3 nm, respectively.

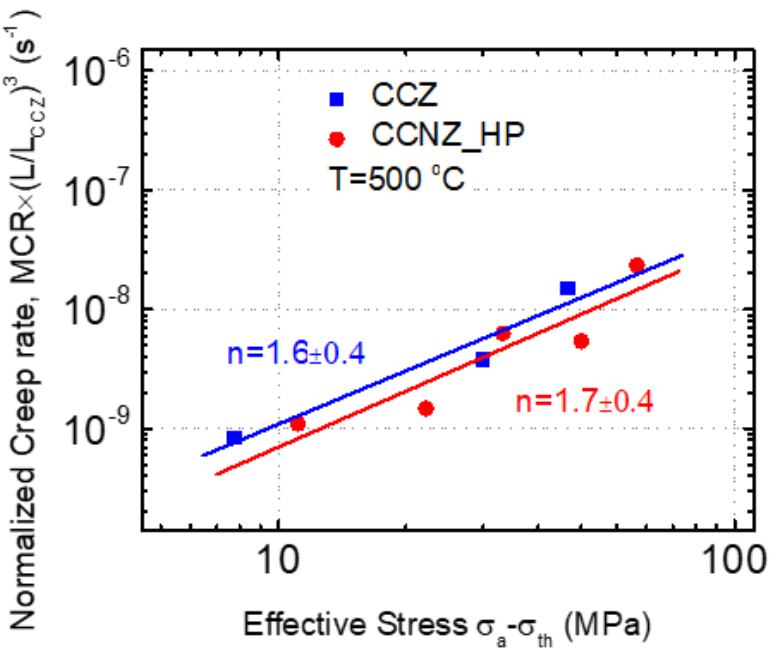


Figure 4-12: Normalized minimum creep strain rate as a function of effective stress of CuCrZr (blue) and CuCrNbZr_HP (red) alloys.

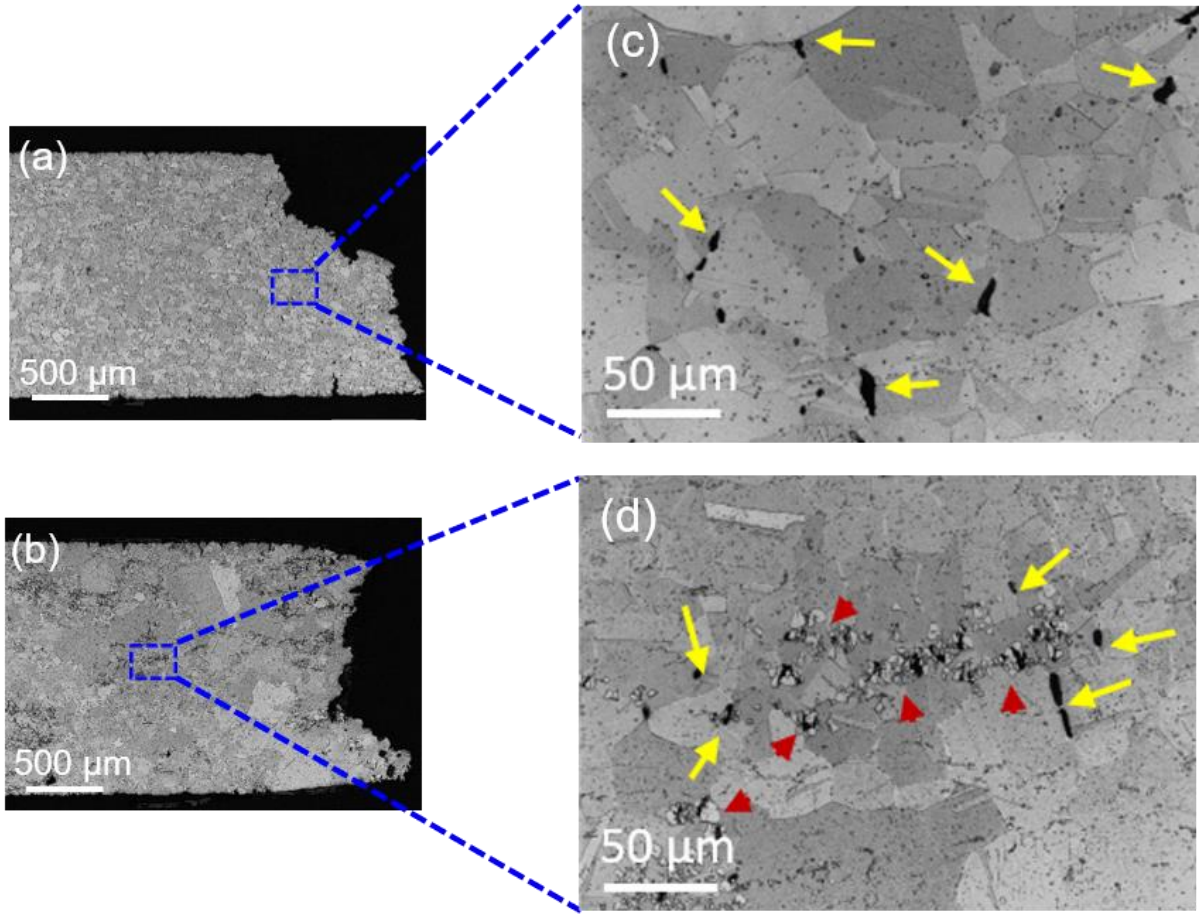


Figure 4-13: (a) and (b) SEM images of the entire fracture of the CuCrZr and CuCrNbZr_HP alloys at 500 °C and 90 MPa, respectivley, (c) and (d) magnified images of dotted blue rectangle regions in (a) and (b) showing larger cracks (indicated by yellow arrows) at grain boundaries without Laves phases, and small cracks at grain boundaries covered by Laves phase (indicated by red arrows).

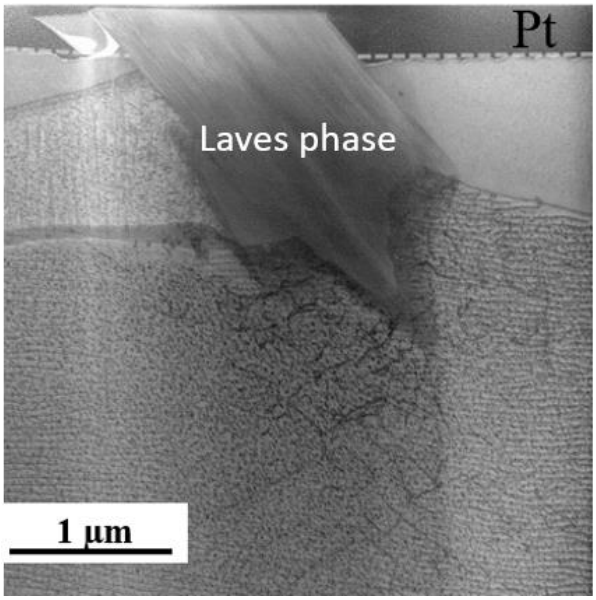


Figure 4-14: STEM-BF image showing a micron-scale Laves phase pinning the multi grains, leaving the dislocations pile up at the interface between the Laves phase and matrix in a crept CuCrNbZr_HP alloy.

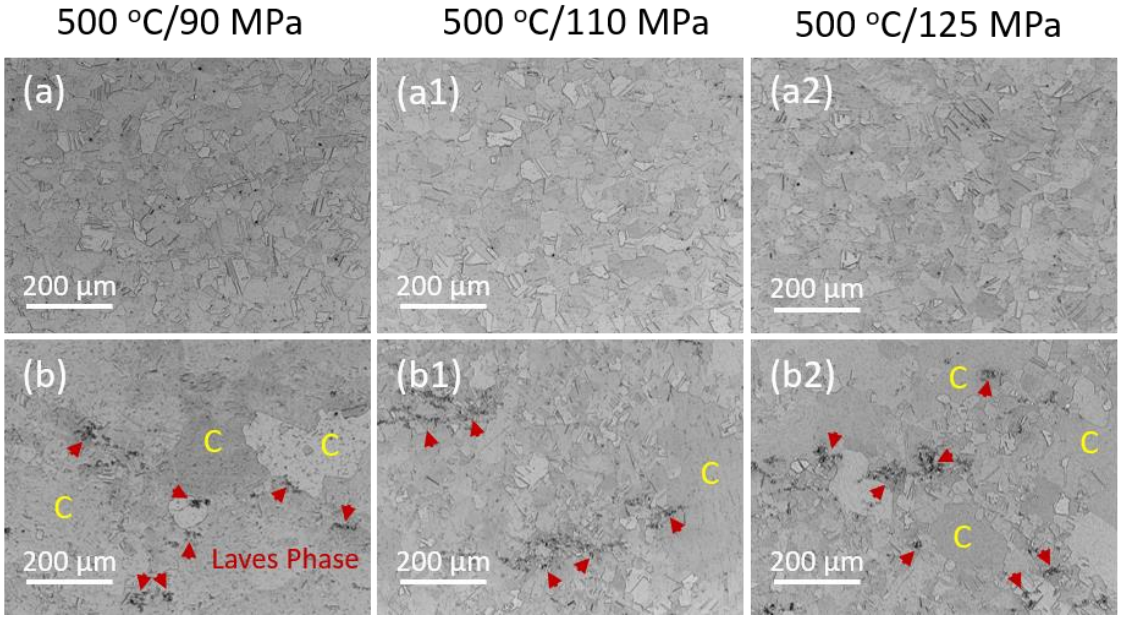


Figure 4-15: Optical images showing grain size of the (a) CuCrZr and (b) CuCrNbZr_HP alloys after creep tests (images taken from unstressed tab area).

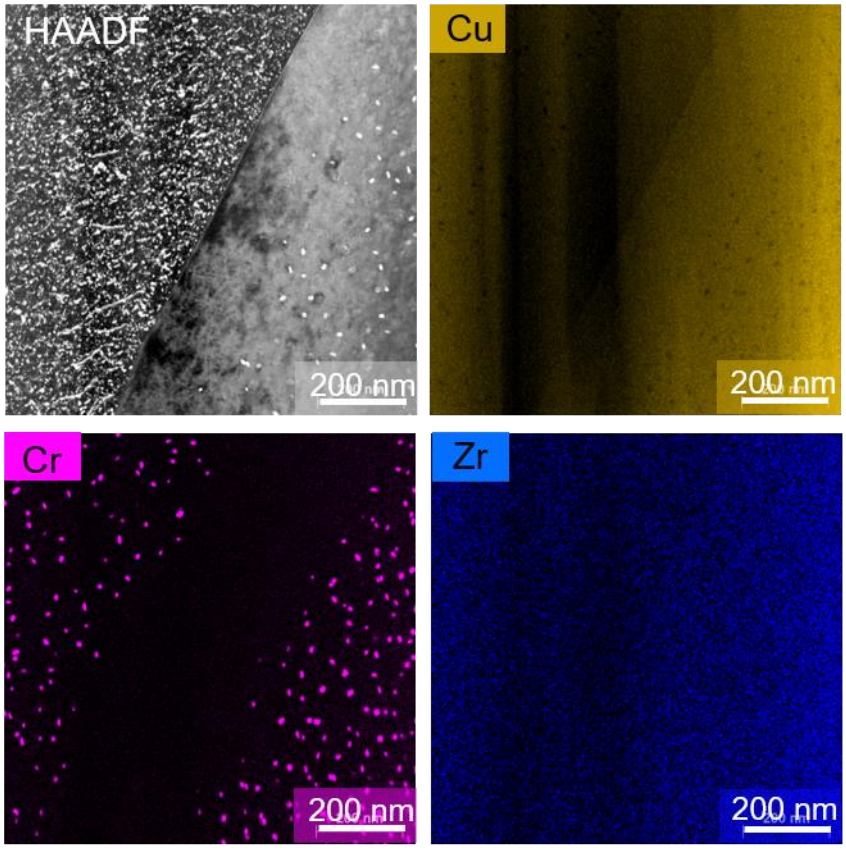


Figure 4-16: STEM-HAADF image and individual composition maps of Cu, Cr and Zr in CuCrZr alloy after creep at 500 ^{o}C and 90 MPa in air (images taken from stressed gauge area).

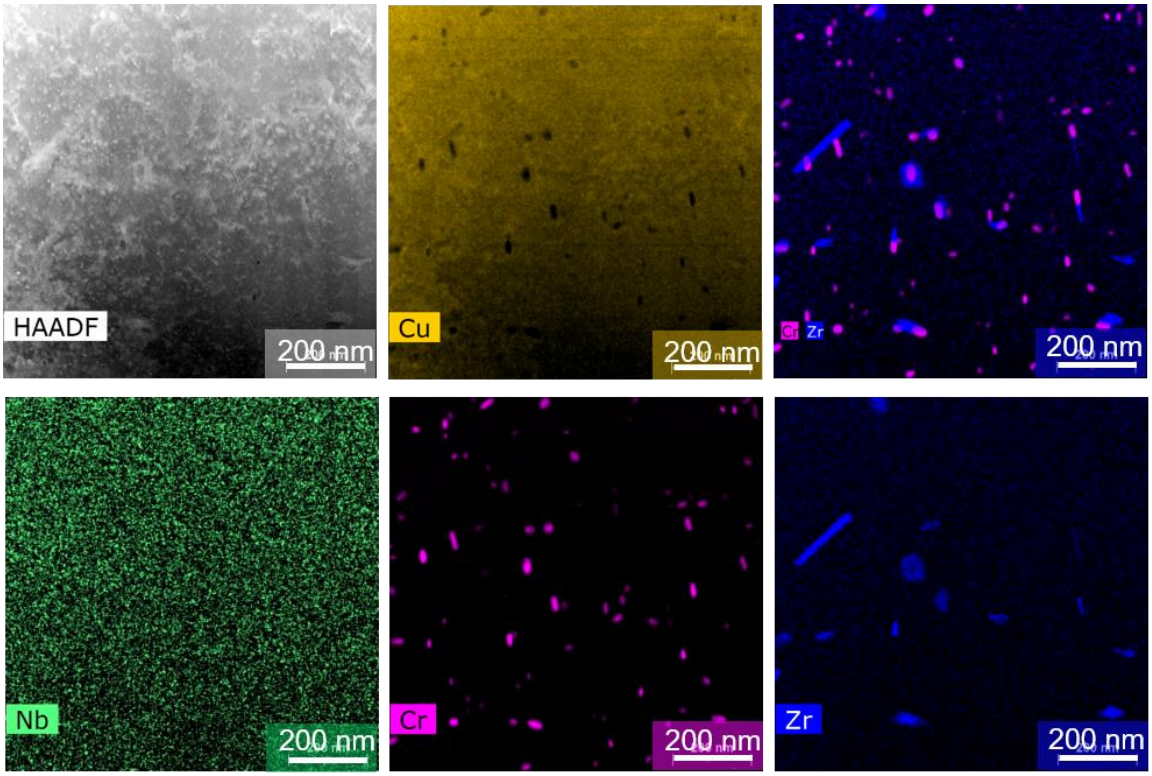


Figure 4-17: STEM-HAADF image and individual composition mappings of Cu, Cr and Zr and a two-elemental-composition map of Cr and Zr in CuCrNbZr_HP alloy after creep at 500 ºC and 90 MPa in air (images taken from stressed gauge area).

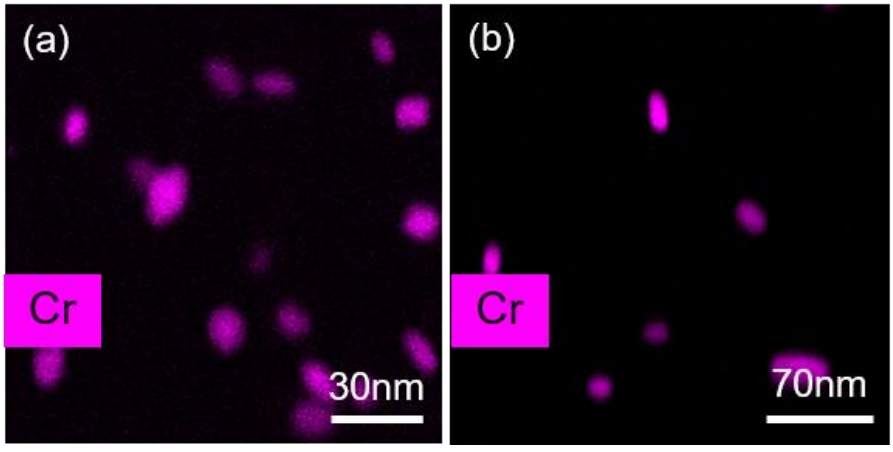


Figure 4-18: High magnification STEM-EDS mappings of Cr precipitates in CuCrZr (left) and CuCrNbZr_HP (right) alloys after creep tests at 500 ºC and 90 MPa in air (images taken from stressed gauge area).

CHAPTER 5

CONCLUSION

5.1 Dilute Cu alloys

The in situ irradiation experiments with 1 MeV Kr^{++} ions are valuable to provide some indication of the critical dose to induce loss of precipitate coherency. The observed effect of suppressed loss of coherency at high sink strengths might be due to nearly equal numbers of interstitial and vacancy defects arriving at the precipitate interface (effectively canceling each other out before loss of coherency from absorption of interstitial defects can occur). At low sink strengths, there might be a preferential medium-range strain-induced bias for absorption of interstitial defects at the precipitates.

The results from irradiated regions induced by 1MeV Ni^{+} ions are consistent with in situ irradiation results. Moreover, the ex situ irradiation experiments also focused on the extent of the loss of coherency beyond the nominal ion irradiated regions, and two important results can be concluded: (1) The extent of the loss of coherency (at low sink strengths, $<5\times10^{13}$ m^{-2}) is in agreement with 1D diffusion of defects. (2) The extent of the loss of coherency region beyond the end of range is significantly reduced at high sink strength. This implies that the 1D diffusion of defects might be reduced in the presence of a high sink strength.

MD simulations show that there's a strong effect of precipitate sink strength on probability of interstitial absorption at precipitates. This provides an alternative explanation for the observed reduction in the extent of the loss of coherency region at high sink strength: it could simply be due to very efficient absorption of defects at the precipitates, with the result that there are insufficient defects to induce loss of coherency well beyond the ion irradiated region.

5.2 CuCrNbZr alloys

In general, a new Cu based CuCrNbZr_HP alloy with a good combination of thermal conductivity (72.1% IACS), sink strength (10^{14} m^{-2}), tensile strength, ductility and creep resistance has been developed and fabricated through economic conventional ingot-metallurgy methods. Thermodynamic models for equilibrium phases in the CuCrNbZr_HP system have been used to aid the composition design and heat treatment parameter selection. The new alloy has been confirmed to have multi-modal distribution of precipitates. Systematic studies have been focused on the creep properties of a newly developed high-purity CuCrNbZr alloy and a reference commercial CuCrZr alloy at 500 ^{o}C for applied uniaxial stress levels of 90~140 MPa in Ar protected atmosphere. Microstructures before and after the creep tests were investigated by optical and transmission electron microscopy. The potential creep mechanisms in both alloys were then evaluated based on creep test and microstructural characterization results. The major findings are summarized below:

1) Coarse Laves phase precipitates with typical size range of 2 to 11 μm are produced in the inter-dendritic region during solidification of the CuCrNbZr_HP alloy. The non-uniform distribution of Laves phase precipitates leads to non-uniform grain size during subsequent solution anneal heat treatment and creep tests. Those grains associated with the Laves precipitates remains small over all testing conditions while grains without precipitates grew much larger.
2) Despite a higher minimum creep rate (attributable to its finer grain size for the smaller grains in the bimodal grain size distribution), the CuCrNbZr_HP alloy has higher creep strength, higher creep fracture ductility, and longer creep life than the CuCrZr alloy. The dominant creep mechanism in both alloys was grain boundary sliding with a threshold stress of ~80 MPa.
3) The Laves phase precipitates in the CuCrNbZr_HP alloy played two roles on the creep behavior. First, these precipitates hinder grain growth during thermal processing of the ingot (solution annealing and aging), producing a bimodal grain size distribution due to nonuniform distribution of the Laves precipitates. The regions clustered with smaller grains are susceptible to grain boundary sliding and crack initiation, resulting in a higher minimum creep rate. The second role of Laves precipitates is to impede the crack propagation, leading to very beneficial enhanced creep strength and life despite the higher minimum creep rate.

This study confirmed the positive effect of the Laves phase precipitates in impeding crack propagation at grain boundaries and increasing creep strength and life. However, to take full advantage of the Laves precipitates, improved control of their spatial distribution is needed.

REFERENCES

[1] Å. Gustafson, M. Hättestrand. Coarsening of precipitates in an advanced creep resistant 9% chromium steel—quantitative microscopy and simulations, Materials Science and Engineering A 333 (2002) 279-286.

[2] R.S. Nelson, J.A. Hudson, D.J. Mazey. The stability of precipitates in an irradiation environment, Journal of Nuclear Materials 44 (1972) 318-330.

[3] H.J. Frost, K.C. Russell. Particle stability with recoil resolution, Acta Materialia 30 (1982) 953-960.

[4] G. Martin. Phase stability under irradiation: Ballistic effects, Physical Review B 30 (1984) 1424-1436.

[5] K.C. Russell. Phase stability under irradiation, Progress in Materials Science 28 (1984) 229-434.

[6] K.H. Heinig, T. Müller, B. Schmidt, M. Strobel, W. Möller. Interfaces under ion irradiation: growth and taming of nanostructures, Applied Physics A 77 (2003) 17-25.

[7] S.W. Chee, B. Stumphy, N.Q. Vo, R.S. Averback, P. Bellon. Dynamic self-organization in Cu alloys under ion irradiation, Acta Materialia 58 (2010) 4088-4099.

[8] J. Ribis, E. Bordas, P. Trocellier, Y. Serruys, Y. de Carlan, A. Legris. Comparison of the neutron and ion irradiation response of nano-oxides in oxide dispersion strengthened materials, Journal of Materials Research 30 (2015) 2210-2221.

[9] M.L. Lescoat, J. Ribis, Y. Chen, E.A. Marquis, E. Bordas, P. Trocellier, Y. Serruys, A. Gentils, O. Kaïtasov, Y. de Carlan, A. Legris. Radiation-induced Ostwald ripening in oxide dispersion strengthened ferritic steels irradiated at high ion dose, Acta Materialia 78 (2014) 328-340.

[10] T. Chen, J.G. Gigax, L. Price, D. Chen, S. Ukai, E. Aydogan, S.A. Maloy, F.A. Garner, L. Shao. Temperature dependent dispersoid stability in ion-irradiated ferritic-martensitic dual-phase oxide-dispersion-strengthened alloy: Coherent interfaces vs. incoherent interfaces, Acta Materialia 116 (2016) 29-42.

[11] L. Tan, T.S. Byun, Y. Katoh, L.L. Snead. Stability of MX-type strengthening nanoprecipitates in ferritic steels under thermal aging, stress and ion irradiation, Acta Materialila 71 (2014) 11-19.

[12] J. He, F. Wan, K. Sridharan, T.R. Allen, A. Certain, V. Shutthanandan, Y.Q. Wu. Stability of nanoclusters in 14YWT oxide dispersion strengthened steel under heavy ion-irradiation by atom probe tomography, Journal of Nuclear Materials 455 (2014) 41-45.

[13] M.F. Ashby, L.M. Brown. On diffraction contrast from inclusions, Philosophical Magazine 8 (1963) 1649-1676.
[14] S. Iwamura, Y. Miura. Loss in coherency and coarsening behavior of Al_3Sc precipitates, Acta Materialia 52 (2004) 591-600.
[15] G.R. Woolhouse. Loss of precipitate coherency by electron irradiation in the high voltage electron microscope, Nature 220 (1968) 573-574.
[16] G.R. Woolhouse, M. Ipohorski. On the interaction between radiation damage and coherent precipitates, Proceedings of the Royal Society A: Mathematical and Physical Sciences, 324 (1971) 415-431.
[17] Z.C. Li, H. Abe, N. Sekimura. Detection of point defects upon ion irradiation by means of precipitate coherency, Journal of Nuclear Materials 362 (2007) 87-92.
[18] R.W. Knoll. Effects of heavy-ion irradiation on the phase stability of several copper-base alloys, Ph.D. Thesis, University of Wisconsin-Madison, UW, USA, August (1981) UWFDM-436.
[19] G.S. Was, Fundamentals of radiation materials science: Metals and Alloys, New York, USA Springer Book Second Edition (2017).
[20] Y.N. Osetsky, D.J. Bacon, A. Serra, B.N. Singh, S.I. Golubov. One-dimensional atomic transport by clusters of self-interstitial atoms in iron and copper, Philosophical Magazine 83 (2003) 61-91.
[21] Y.N. Osetsky, D.J. Bacon, A. Serra, B. Singh, S.I. Golubov. Stability and mobility of defect clusters and dislocation loops in metals, Journal of Nuclear Materials 276 (2000) 65-77.
[22] H.L. Heinisch, H. Trinkaus, B.N. Singh. Kinetic Monte Carlo studies of the reaction kinetics of crystal defects that diffuse one-dimensionally with occasional transverse migration, Journal of Nuclear Materials 367-370 (2007) 332-337.
[23] B.D. Wirth, G.R. Odette, D. Maroudas, G.E. Lucas. Energetics of formation and migration of self-interstitials and self-interstitial clusters in α-iron, Journal of Nuclear Materials 244 (1997) 185-194.
[24] K. Arakawa, K. Ono, M. Isshiki, K. Mimura, M. Uchikoshi, H. Mori. Observation of the one-dimensional diffusion of nanometer-sized dislocation loops, Science 318 (2007) 956-959.
[25] Y. Matsukawa, S.J. Zinkle. One-dimensional fast migration of vacancy clusters in metals, Science 318 (2007) 959-962.

[26] S.J. Zinkle. Applicability of copper alloys for DEMO high heat flux components, Physica Scripta T167 (2016) 014004.
[27] Metals Handbook, Desk Edition, ASM, Ohio, USA, (1984) 71.
[28] I.S. Batra, G.K. Dey, U.D. Kulkarni, S. Banerjee. Microstructure and properties of a Cu–Cr–Zr alloy, Journal of Nuclear Materials 299 (2001) 91-100.
[29] R.W. Knights, P. Wilkes. Precipitation of chromium in copper and copper-nickel base alloys, Metallurgical Transactions 4 (1973) 2389-2393.
[30] T. Fuji, H. Nakazawa, M. Kato, U. Dahmen. Crystallography and morphology of nanosized Cr particles in a Cu–0.2% Cr alloy, Acta Materialia 48 (2000) 1033-1045.
[31] A. Chbihi, X. Sauvage, D. Blavette. Atomic scale investigation of Cr precipitation in copper, Acta Materialia 60 (2012) 4575-4585.
[32] S.J. Zinkle, W.S. Eatherly. Effect of heat treatments on the tensile and electrical properties of high-strength, high-conductivity copper alloys, Fusion Materials Semiannual Progress Report for Period ending June 30, 1997 DOE/ER-0313/22 Oak Ridge National Lab 143-148.
[33] S.J. Zinkle. Evaluation of high strength, high conductivity CuNiBe alloys for fusion energy applications, Journal of Nuclear Materials 449 (2014) 277-289.
[34] K.J. Zeng, M. Hämäläinen. A theoretical study of the phase equilibria in the Cu-Cr-Zr system, Journal of Alloys and Compounds 220 (1995) 53-61.
[35] K.J. Zeng, M. Hämäläinen, K. Lilius. Phase relationships in Cu-rich corner of the Cu-Cr-Zr phase diagram, Scripta Metallurgica et Materialia 32 (1995) 2009-2014.
[36] D.J. Edwards, B.N. Singh, S. Tähtinen. Effect of heat treatments on precipitate microstructure and mechanical properties of a CuCrZr alloy, Journal of Nuclear Materials 367 (2007) 904-909.
[37] S.J. Zinkle, A. Horsewell, B.N. Singh, W.F. Sommer. Dispersoid stability in a Cu-Al_2O_3 alloy under energetic cascade damage conditions, Journal of Nuclear Materials 195 (1992) 11-16.
[38] S.J. Zinkle, E.V. Nesterova, V.R. Barabash, V.V. Rybin, A.V. Naberenkov. Effect of ion irradiation on the structural stability of dispersion-strengthened copper alloys, Journal of Nuclear Materials 208 (1994) 119-127.
[39] D.L. Ellis, G.M. Michal. Precipitation strengthened high strength, high conductivity Cu-Cr-Nb alloys produced by chill block melt spinning, Ph. D. Thesis, Case Westem Reserve University,Cleveland, OH, USA, September (1989) 19900002537.

[40] D.L. Ellis. GRCop-84: A high-temperature copper alloy for high-heat-flux applications, NASA/TM (2005) 213566.
[41] R.O. Williams. Precipitation process in copper-chromium alloys, ASM Transaction 52 (1960) 530-544.
[42] I.S. Batra, G.K. Dey, U.D. Kulkarni, S. Banerjee. Precipitation in a Cu–Cr–Zr alloy, Materials Science and Engineering A 356 (2003) 32-36.
[43] M. Hatakeyama, T. Toyama, J. Yang, Y. Nagai, M. Hasegawa, T. Ohkubo, M. Eldrup, B.N. Singh, 3D-AP and positron annihilation study of precipitation behavior in Cu–Cr–Zr alloy, Journal of Nuclear Materials 386-388 (2009) 852-855.
[44] L. Bi, P. Liu, X. Chen, X. Liu, W. Li, F. Ma. Analysis of phase in Cu–15%Cr–0.24%Zr alloy, Transactions of Nonferrous Metals Society of China 23 (2013) 1342-1348.
[45] M.W. Decker, J.R. Groza, J.C. Gibeling. Creep properties of an extruded copper–8% chromium–4% niobium alloy, Materials Science and Engineering A 369 (2004) 101-111.
[46] H.C. de Groh, D.L. Ellis, W.S. Loewenthal. Comparison of GRCop-84 to Other Cu Alloys with High Thermal Conductivities, Journal of Materials Engineering and Performance 17 (2007) 594-606.
[47] K.R. Anderson, J.R. Groza, R.L. Dreshfield, D.L. Ellis. High-performance dispersion-strengthened Cu-8 Cr-4 Nb alloy, Metallurgical and Materials Transactions A 26 (1995) 2197-2206.
[48] Y. Yang, L. Wang, L.L. Snead, S.J. Zinkle. Development of novel Cu-Cr-Nb-Zr alloys with the aid of computational thermodynamics, Materials and Design 156 (2018) 370-380.
[49] N. Saunders, A.P. Miodownik. CALPHAD (calculation of phase diagrams): a comprehensive guide, Amsterdam, Netherlands, Elsevier Book (1998).
[50] K-M Kabelmetal, Technical data brochure on Cu alloy moulds for continuous casting (Elbrodur CuCrZr alloy).
[51] S.J. Zinkle, L.L. Snead. Opportunities and limitations for ion beams in radiation effects studies: bridging critical gaps between charged particle and neutron irradiations, Scripta Materialia 143 (2018) 154-160.
[52] M.A. Kirk, P.M. Baldo, A.C.Y. Liu, E.A. Ryan, R.C. Birtcher, Z. Yao, S. Xu, M.L. Jenkins, M. Hernandez-Mayoral, D. Kaoumi, A.T. Motta. In situ transmission electron microscopy and ion irradiation of ferritic materials, Microscopy Research and Technique 72 (2009) 182-186.

[53] R.E. Stoller, M.B. Toloczko, G.S. Was, A.G. Certain, S. Dwaraknath, F.A. Garner. On the use of SRIM for computing radiation damage exposure, Nuclear Instruments and Methods in Physics Research Section B: Beam Interactions with Materials and Atoms 310 (2013) 75-80.
[54] J. Marian, B.D. Wirth, A. Caro, B. Sadigh, G.R. Odette, J.M. Perlado, T.D. de la Rubia. Dynamics of self-interstitial cluster migration in pure α-Fe and Fe-Cu alloys, Physical Review B 65 (2002) 144102.
[55] K. Arakawa, M. Hatanaka, H. Mori, K. Ono. Effects of chromium on the one-dimensional motion of interstitial-type dislocation loops in iron, Journal of Nuclear Materials 329-333 (2004) 1194-1198.
[56] E. Getto, Z. Jiao, A.M. Monterrosa, K. Sun, G.S. Was. Effect of irradiation mode on the microstructure of self-ion irradiated ferritic-martensitic alloys, Journal of Nuclear Materials 465 (2015) 116-126.
[57] C.B. Carter, D.B. Williams. Transmission electron microscopy: Diffraction, imaging, and spectrometry, Springer Book 2016.
[58] P.B. Hirsch, A. Howie, R. Nicholson, D. Pashley, M.J. Whelan. Electron microscopy of thin crystals, Butterworths London 320 (1965).
[59] X. Shi, S. Ghose, E. Dooryhee. Performance calculations of the X-ray powder diffraction beamline at NSLS-II, Journal of Synchrotron 20 (2013) 234-242.
[60] W.G. Wolfer. Fundamental properties of defects in metals, Comprehensive Nulcear Materials1 (2012) 1-45.
[61] K. Schroder. CRC handbook of electrical resistivitives of binary metallic alloys, CRC Press Book (1983).
[62] D. Chapman. High conductivity copper for electrical engineering, Copper Development Association's resource library 122 (2016) 1-32.
[63] D.J. Thoma, J.H. Perepezko. An experimental evaluation of the phase relationships and solubilities in the Nb-Cr system, Materials Science and Engineering A 156 (1992) 97-108.
[64] A.W. Hull, W.P. Davey. Crystal structure of chromium, Physical Review 14 (1919) 540-540.
[65] H.M. Otte. Lattice parameter determinations with an x-ray spectrogoniometer by the debye-scherrer method and the effect of specimen condition, Journal of Appllied Physics 32 (1961) 1536-1546.

[66] M.F. Ashby, L.M. Brown. Diffraction contrast from spherically symmetrical coherency strains, The Philosophical Magazine: A Journal of Theoretical Experimental and Applied Physics 8 (1963) 1083-1103.
[67] L. Peng, H. Xie, G. Huang, Y. Li, X. Yin, X. Feng, X. Mi, Z. Yang. The phase transformation and its effects on properties of a Cu−0.12 wt% Zr alloy, Materials Science and Engineering A 633 (2015) 28-34.
[68] V. Barabash, A. Peacock, S. Fabritsiev, G. Kalinin, S. Zinkle, A. Rowcliffe, J.W. Rensman, A.A. Tavassoli, P. Marmy, P.J. Karditsas, F. Gillemot, M. Akiba. Materials challenges for ITER – Current status and future activities, Journal of Nuclear Materials 367-370 (2007) 21-32.
[69] F. Abe, T.U. Kern, R. Viswanathan. Creep-resistant steels, Amsterdam, Netherlands, Elsevier Book (2008).
[70] C.R. Barrett, O.D. Sherby. Steady-state creep characteristics of polycrystalline copper in the temperature range 400 to 950 C, Transaction Metallurgy Society AIME 230 (1964) 1322-1327.
[71] S.J. Zinkle, G.L. Kulcinski, R.W. Knoll. Microstructure of copper following high dose 14-MeV Cu ion irradiation, Journal of Nuclear Materials 138 (1986) 46-56.
[72] S. Plimpton. Fast parallel algorithms for short-range molecular dynamics, Journal of Computational Physics 117 (1995) 1-19.
[73] S.M. Foiles, M.I. Baskes, M.S. Daw. Embedded-atom-method functions for the fcc metals Cu, Ag, Au, Ni, Pd, Pt, and their alloys, Physical Review B 33 (1986) 7983.
[74] R. Pasianot, E.J. Savino. Embedded-atom-method interatomic potentials for hcp metals, Physical Review B 45 (1992) 12704.
[75] K. Nordlund, R.S. Averback. Inverse Kirkendall mixing in collision cascades, Physical Review B 59 (1999) 20.
[76] A.S. Alomari, N. Kumar, K.L. Murty. Investigation on Creep Mechanisms of Alloy 709, ASME Power and Energy/ICOPE-17, Charlotte, NC USA, (2017) 26-30.
[77] J. Cadek. Creep in metallic materials, Amsterdam, Netherlands, Elsevier Book (1988) 150-155.
[78] H.J. Frost, M.F. Ashby. Deformation mechanism maps: the plasticity and creep of metals and ceramics, Pergamon Press, Oxford, UK 1982.

[79] O.A. Ruano, O.D. Sherby. Low stress creep of fine-grained materials at intermediate temperatures: Diffusional creep or grain boundary sliding? Materials Science and Engineering A 56 (1982) 167-175.
[80] W.B. Beere, G.W. Greenwood. The effect of hydrostatic pressure on the shrinkage of cavities in metals, Materials Science Journal 5 (1971) 107-113.
[81] S.E. Broyles, K.R. Anderson, J.R. Groza, J.C. Gibeling. Creep deformation of dispersion-strengthened copper, Metallurgical and Materials Transcations A 27 (1996) 1217-1227.
[82] H.M. Ledbetter, E.R. Naimon. Elastic properties of metals and alloys. II. Copper, Journal of Physical and Chemical Reference Data 3 (1974) 897-935.
[83] T.G. Langdon. The role of grain boundaries in high temperature deformation, Materials Science and Engineering A 166 (1993) 67-79.

VITA

Ling Wang was born in City of Suzhou, Jiangsu Province, China on November 9, 1989 to Minghui Wang and Yuyun Zhang. She attended No.1 Middle high school in city of Suzhou, Jiangsu Province. After graduating, Ling attended Tianjin Polytechnic University in city of Tianjin, where she received her B.S. degree in Materials Science and Engineering in June, 2012. She started pursuing her master degree in September under the mentorship of Prof. Wei Wang in Shanghai University of Engineering Science, majoring in Materials Science. Her Master degree thesis is titled with "Microstructural evolution of Cu-rich precipitates in model ferritic steel". During her Master degree study, she got a chance to spend 13 months as a visiting student in Prof. Lumin Wang's research group in the Department of Nuclear Engineering and Radiological Sciences in the University of Michigan, Ann Arbor from December 2013 till end of January 2015. There, she was focused on transmission electron microscopy (TEM) sample preparation (mainly through carbon replica) and TEM characterization on nano-scale Cu-rich precipitates in RPV model steels. She decided to apply for the Ph.D. program in U.S. universities when she found her strong interests in phase transformation of unstable precipitates after thermal-aging for thousands of hours and TEM characterization an amazing technique. Ling graduated with her Master's degree in March, 2015 after she returned to China. In the same year, Ling enrolled at the University of Tennessee as a graduate research assistant in the Department of Materials Science and Engineering under Prof. Steven J. Zinkle, where she was involved in two research projects related to phase stability of precipitates after ion irradiation and creep deformation. She was a summer intern with the IVEM group at Argonne National Laboratory under Dr. Meimei Li for three months in 2019 and became experienced with the IVEM-Tandem facility. She was awarded a graduate CMP fellowship since July 2019 and a NSUF FY 2019 RTE 3rd Call proposal in Fall 2019. Ling will obtain her Doctor of Philosophy degree in Materials Science and Engineering in May 2020.